Study of Bottomonium States in Radiative $\Upsilon(2S)$ Decays at Belle

A Thesis

Submitted to the

TATA INSTITUTE OF FUNDAMENTAL RESEARCH,

MUMBAI

for the degree of Doctor of Philosophy

in Physics

by

Saurabh Sandilya

School of Natural Sciences

Tata Institute of Fundamental Research

Mumbai

April, 2015

[Final version submitted in August, 2015]

“Dedicated to my family and the other taxpayers”

DECLARATION

This thesis is a presentation of my original research work. Wherever contributions of other are involved, every effort is made to indicate this clearly, with due reference to the literature, and acknowledgement of collaborative research and discussions.

The work was done under the guidance of Professor Gagan B. Mohanty, at the Tata Institute of Fundamental Research, Mumbai.

Saurabh Sandilya

In my capacity as supervisor of the candidate's thesis, I certify that the above statements are true to the best of my knowledge.

Prof. Gagan B. Mohanty

Date :

Acknowledgement

The work presented in this thesis would not have been possible without the help of many individuals, involved at different stages. This thesis will be incomplete without acknowledging them.

I express my sincerest gratitude towards my advisor Prof. Gagan B. Mohanty for his continuous support, inspiring discussions, invaluable guidance, and constant encouragement. He has been always supportive, patient, and showed immense confidence in me throughout this work.

I had a great opportunity to work closely with Prof. Karim Trabelsi at KEK, Japan. He has inculcated an immaculate working discipline in me which will serve me in good purpose for the rest of my academic and also non-academic life. His commitment to research, vision and inspiring personality had profound influence on me.

Belle collaboration has members more than 470 physicists from 18 countries. I formally wish to thank Profs. S. Bahinipati, P. Behera, D. Besson, B. Bhuyan, T. Browder, S. Eidelman, J. Libby, R. Mizuk, R. Mussa, M. Nakao, C. P. Shen, Y. Sakai, J. Singh, R. Sinha and C. Z. Yuan for giving us very useful discussions and comments on our analysis.

My deepest respect goes to Profs. T. Aziz, A. Dighe, S. Dugad, M. Guchait, N. Krishnan, N. Mathur, I. Mazumdar, K. Mazumdar, G. Majumder and R. Palit for their valuable suggestions on my work.

I have been blessed with a friendly and cheerful group of fellow colleagues Bibhu, Gouranga, Kolahal, Nairit, Ninad, Nisar, Rajdeep, Ram Krishna, Sanjeev, Sanmay, Saranya, Soureek, Vargheese and Vipin. Department staff members Chendvankar sir, Despande sir, Mandakini ma'am, Divekar ji, Kamesh ji, Kolwalkar ji, Pathare ji, Minal ji, Brij, Sukant, Samuel, Prashant and Thomas have always been available to help me in technical and administrative works.

My sincere thanks to Anuradha, Dipankar, Jasmine, Kiran, Rahul, Subha for encouraging me through the thick and thin during my TIFR days and a very special thanks to Neha for being always helpful since my M.Sc. days. I am also thankful to my Belle collaboration friends and seniors Abinash, Nikhil, Anu, Deepanwita and Minakshi for their suggestions and discussions.

My grandfather Prof. Shyama Kant Jha has always encouraged me to ask questions during my childhood days which propelled me to pursue a career in academics. I am thankful to my parents Mr. K. P. Thakur and Mrs. Unman Madhukanta, and my sister Ruchi Sandilya for their patience and understanding, during my hustling days.

Finally, I thank and dedicate this thesis to the taxpayers of this country for supporting my education and research.

Synopsis

0.1 Introduction

The bottomonium family, a bound system of a bottom (b) quark and its antiquark ($\bar{b}$), offers a unique laboratory to study spin-dependent strong interactions. As the b quark is heavier than the u, d, s and c quarks, the bottomonia can be well described by the non-relativistic quantum mechanics. These states are characterised by their spin $S = 0$ or 1, owing to an antiparallel or a parallel configuration of b and $\bar{b}$, orbital angular momentum (L), and total angular momentum (J). Among them the $\Upsilon(nS)$ states have $J^{PC} = 1^{--}$ and thus can be directly produced through virtual photons in e^+e^- collisions in the process $e^+e^- \to \gamma^\star \to \Upsilon(nS)$. At e^+e^- colliders, other bottomonium states are mainly produced from the $\Upsilon(nS)$ decays.

The spin-singlet ($S = 0$) states with zero orbital angular momentum ($L = 0$) are denoted as the $\eta_b(nS)$. The $\eta_b(1S)$ meson, also the ground state of the bottomonium family, was discovered by the BaBar Collaboration in 2008 in the decay $\Upsilon(3S) \to \gamma\eta_b(1S)$ [1]. Recently, attempts have been made to look for its radially excited partner, the $\eta_b(2S)$. The first evidence for the $\eta_b(2S)$ is reported by the Belle Collaboration [2] using a 133.4 fb^{-1} of data sample collected near the $\Upsilon(5S)$ resonance. The study is performed with the process $e^+e^- \to \Upsilon(5S) \to h_b(nP)\pi^+\pi^-, h_b(nP) \to \eta_b(mS)\gamma$ for $n \geq m = 1$ and 2, in which the $\eta_b(mS)$ states are not exclusively reconstructed. Here, the intermediate $h_b(nP)$ states are the P–wave spin singlet states ($S = 0$, $L = 1$) of the bottomonium family. The $\eta_b(2S)$ mass is measured in the transition $h_b(2P) \to \eta_b(2S)\gamma$ to be $9999.0 \pm 3.5(\text{stat.})^{+2.8}_{-1.9}(\text{syst.})$ MeV/c^2, which corresponds to a hyperfine mass splitting between the $\Upsilon(2S)$ and $\eta_b(2S)$ states, $\Delta M_{\text{HF}}(2S) \equiv M[\Upsilon(2S)] - M[\eta_b(2S)]$, of $24.3^{+4.0}_{-4.5}$ MeV/c^2.

There is a recent claim of observation of a bottomonium state, $X_{b\bar{b}}(9975)$, in the radiative $\Upsilon(2S)$ decay based on an analysis performed on a data sample of 9.3×10^6 $\Upsilon(2S)$ decays recorded with the CLEO III detector [3]. The $X_{b\bar{b}}(9975)$ state is exclusively reconstructed in 26 hadronic final states, and is measured with a significance of about 5 standard deviations (σ) at a mass of $9974.6 \pm 2.3(\text{stat.}) \pm 2.1(\text{syst.})$ MeV/c^2. Furthermore, the $X_{b\bar{b}}(9975)$ state is assigned to the $\eta_b(2S)$, which corresponds to the hyperfine splitting, $\Delta M_{\rm HF}(2S) = 48.6 \pm 3.1$ MeV/c^2. The claim of $X_{b\bar{b}}(9975)$ state to be the $\eta_b(2S)$ is in contrast with the Belle result, while the latter is in agreement with the lattice QCD, potential model and related theoretical predictions summarized in Refs. [4, 5].

The P-wave spin-triplet states $\chi_{bJ}(1P)$ and $\chi_{bJ}(2P)$ ($J = 0, 1, 2$) were discovered more than 30 years ago, while the $\chi_{bJ}(3P)$ is observed only in 2011 by the ATLAS experiment [6]. In 2008, the CLEO Collaboration had reported first observations of the $\chi_{bJ}(1P)$ and $\chi_{bJ}(2P)$ decays into specific final states of light hadrons, where the $\chi_{bJ}(1P)$ and $\chi_{bJ}(2P)$ are produced in the radiative transition of the $\Upsilon(2S)$ and $\Upsilon(3S)$, respectively [7]. For this study, CLEO used an on-resonance data sample corresponding to 9.3×10^6 $\Upsilon(2S)$ and 20.8×10^6 $\Upsilon(3S)$ decays. Further, the $\chi_{bJ}(1P)$ and $\chi_{bJ}(2P)$ states were reconstructed from a combination of 12 or fewer particles, where the particles are defined as a photon, $\pi^{\pm}$, $K^{\pm}$, $p/\overline{p}$, and K^0_S (photons must be paired into either π^0 or η). At the end, 14 modes were identified that have had at least 5σ significance from both $\chi_{bJ}(1P)$ and $\chi_{bJ}(2P)$ decays.

With almost 17 times larger data sample recorded at the $\Upsilon(2S)$ resonance compared to CLEO, Belle has a unique opportunity to either confirm or refute the aforementioned observation of the $X_{b\bar{b}}(9975)$ state. A search for the $X_{b\bar{b}}(9975)$ is discussed in detail in Section 0.3. The study of $\chi_{bJ}(1P)$ decays in specific hadronic final states at Belle would not only improve over the CLEO's measurements of 14 modes, but also potentially uncover many new modes. Section 0.4 dwells on our study of $\chi_{bJ}(1P)$ decays to several hadronic states.

0.2 Detector and Dataset

The dataset used in our study is recorded with the Belle detector [8] located at an interaction region of the KEKB asymmetric-energy e^+e^- collider [9] in Tsukuba, Japan. Belle is a general-purpose magnetic spectrometer with a large solid angle coverage. It includes a silicon vertex detector, a 50-layer central drift chamber (CDC), an array of aerogel threshold Cherenkov counters (ACC), time-of-flight scintillation counters (TOF), and an electromagnetic calorimeter (ECL) comprising CsI(Tl) crystals. All these components are located inside a superconducting solenoid coil that provides a 1.5 T magnetic field. An iron flux return located outside of the coil is instrumented to detect K^0_L mesons and muons.

Belle was mainly designed to study CP violation in the B-meson system, for which most of its data were recorded at the $\Upsilon(4S)$ resonance that decays almost entirely to a $B\bar{B}$ pair. In addition, Belle also recorded world's largest e^+e^- collision data near the $\Upsilon(1S)$, $\Upsilon(2S)$ and $\Upsilon(5S)$ resonances. The latter data sets are well suited for hadron spectroscopy related studies.

Our studies are performed using a $24.7\,\mathrm{fb}^{-1}$ of data, equivalent to $(157.8 \pm 3.6) \times 10^6$ $\Upsilon(2S)$ events, recorded at the $\Upsilon(2S)$ resonance. A $1.7\,\mathrm{fb}^{-1}$ of off-resonance data sample, collected 30 MeV below the $\Upsilon(2S)$ peak, provides a convenient though limited sample to study the $e^+e^- \to q\bar{q}$ ($q = u, d, s, c$) continuum background. Hence, an $89.5\,\mathrm{fb}^{-1}$ of off-resonance data sample recorded 60 MeV below the $\Upsilon(4S)$ resonance is also used for the continuum background study. Monte Carlo (MC) samples, equivalent to the total $\Upsilon(2S)$ data sample of Belle, of inclusive $\Upsilon(2S)$ decays are generated with Pythia [10]. These MC samples are utilised for the investigation of potential peaking backgrounds.

0.3 Search for $X_{b\bar{b}}(9975)$

As discussed in Section 0.1, having 17 times larger data sample compared to CLEO, Belle can unambiguously confirm or refute the observation of the $X_{b\bar{b}}(9975)$ state. We perform a search for the $X_{b\bar{b}}(9975)$ in the reaction, $\Upsilon(2S) \to \gamma X_{b\bar{b}}(9975)$ [11], where the $X_{b\bar{b}}(9975)$ is reconstructed in the same 26 modes as in Ref. [3]:

$2(\pi^+\pi^-)$, $3(\pi^+\pi^-)$, $4(\pi^+\pi^-)$, $5(\pi^+\pi^-)$, $(\pi^+\pi^-)(K^+K^-)$, $2(\pi^+\pi^-)(K^+K^-)$, $3(\pi^+\pi^-)(K^+K^-)$, $4(\pi^+\pi^-)(K^+K^-)$, $2(K^+K^-)$, $(\pi^+\pi^-)2(K^+K^-)$, $2(\pi^+\pi^-)2(K^+K^-)$, $3(\pi^+\pi^-)2(K^+K^-)$, $(\pi^+\pi^-)p\bar{p}$, $2(\pi^+\pi^-)p\bar{p}$, $3(\pi^+\pi^-)p\bar{p}$, $4(\pi^+\pi^-)p\bar{p}$, $(\pi^+\pi^-)(K^+K^-)p\bar{p}$, $2(\pi^+\pi^-)(K^+K^-)p\bar{p}$, $3(\pi^+\pi^-)(K^+K^-)p\bar{p}$, $\pi^\pm K^\mp K_S^0$, $(\pi^+\pi^-)\pi^\pm K^\mp K_S^0$, $2(\pi^+\pi^-)\pi^\pm K^\mp K_S^0$, $3(\pi^+\pi^-)\pi^\pm K^\mp K_S^0$, $(\pi^+\pi^-)2K_S^0$, $2(\pi^+\pi^-)2K_S^0$, and $3(\pi^+\pi^-)2K_S^0$

The reaction $\Upsilon(2S) \to \gamma\chi_{bJ}(1P)(J = 0, 1, 2)$, where the $\chi_{bJ}(1P)$ decays to the aforementioned 26 hadronic modes, serves as a good control sample. In the same analysis, the $\eta_b(1S)$ state is also looked for in the radiative process $\Upsilon(2S) \to \gamma\eta_b(1S)$.

Half a million signal MC events are produced for each of the 26 hadronic final states arising from the $X_{b\bar{b}}(9975)$, $\eta_b(1S)$ and $\chi_{bJ}(1P)$ decays. The radiative transition of $\Upsilon(2S)$ is generated with the helicity amplitude formalism [12]. Hadronic decays of the $(b\bar{b})$ system are modeled assuming a phase space distribution, where an interface to PHOTOS [13] has been added to incorporate final state radiation effects.

Our event reconstruction procedure starts with the selection of an appropriate number and type of charged particles to form a $(b\bar{b})$ system. We require all charged tracks, except for those from the K_S^0 decays, to originate from the vicinity of the interaction point by requiring their impact parameters along and perpendicular to the z axis to be less than 4 cm and 1 cm, respectively. Here, the z axis is the direction opposite to the e^+ beam. Based on the information from various particle identification subdetectors namely CDC, TOF, and ACC, the track candidates are identified as pions, kaons, or protons. Candidate K_S^0 mesons are reconstructed by combining two oppositely charged tracks that have an invariant mass between 486 and 509 MeV/c^2; the selected candidates are also required to satisfy the criteria described in Ref. [14].

An isolated cluster in the ECL that has an energy greater than 22 MeV and a cluster shape consistent with an electromagnetic shower is selected as a photon candidate. The expected energy range of the signal photon for $X_{b\bar{b}}(9975)$ is 30 – 70 MeV and for $\eta_b(1S)$ is 400 – 900 MeV. Photons detected from the backward endcap part of the ECL are excluded for the $\eta_b(1S)$ selection in order to suppress the beam-related background. For the $X_{b\bar{b}}(9975)$ selection, photons detected only in the barrel part of the ECL (excluding both the forward and backward endcap) are considered, as the photon from $\Upsilon(2S) \to \gamma X_{b\bar{b}}(9975)$ is even less energetic and thus more prone to contamination from the beam background. The photon energy resolution in the barrel ECL ranges between 2% at 1 GeV and 3% at 100 MeV.

An $\Upsilon(2S)$ candidate is formed by combining a photon candidate with the $(b\bar{b})$ system. The continuum events coming from the process $e^+e^- \to q\bar{q}$, where $q = u, d, s$ and c quarks, pose as a background. To suppress these events, the cosine of the angle between the photon candidate and the event thrust axis ($\cos\theta_T$) is utilised. Signal events have a spherical event topology giving rise to a uniform $\cos\theta_T$ distribution whereas dijet continuum events peak near $\cos\theta_T = \pm 1$. Events satisfying $|\cos\theta_T| < 0.8$ are thus selected as signal. This requirement substantially (60%) reduces continuum background with a modest loss (20%) of signal.

Requirements are made on the difference between the energy of the $\Upsilon(2S)$ candidate and the beam energy (ΔE) , the momentum of the $\Upsilon(2S)$ candidate ($P^{\star}_{\Upsilon(2S)}$), and the angle between the γ candidate and the $(b\bar{b})$ system ($\theta_{\gamma(b\bar{b})}$). These three quantities are calculated in the e^+e^- center-of-mass (CM) frame. The requirements are obtained for $X_{b\bar{b}}(9975)$ and $\eta_b(1S)$ signal regions separately from an optimization procedure by using $S/\sqrt{S+B}$ as a figure of merit, where S is the number of signal events estimated by assuming a branching fraction of 46.2×10^{-6} for $X_{b\bar{b}}(9975)$ [3] and 3.9×10^{-6} for the $\eta_b(1S)$ [15], and B is the number of background events obtained from a sum of the off-resonance data and a data equivalent of generic MC events. Criteria for the $X_{b\bar{b}}(9975)$ and $\eta_b(1S)$ signal selections are summarised below:

- $X_{b\bar{b}}(9975)$:
    - $-40\,\mathrm{MeV} < \Delta E < 50\,\mathrm{MeV}$
    - $P^{\star}_{\Upsilon(2S)} < 30\,\mathrm{MeV}/c$
    - $\theta_{\gamma(b\bar{b})} > 150^{\circ}$
- $\eta_b(1S)$:
    - $-30\,\mathrm{MeV} < \Delta E < 80\,\mathrm{MeV}$
    - $P^{\star}_{\Upsilon(2S)} < 50\,\mathrm{MeV}/c$
    - $\theta_{\gamma(b\bar{b})} > 177^{\circ}$
    - As the background contribution is found to be dominated by photons coming from the π^0 decay, we require a π^0 veto. For this, the difference between the nominal π^0 mass [16] and the invariant mass formed by combining the signal photon with another photon candidate in the same event is computed for each photon pair, and the smallest magnitude of these differences ($\Delta M_{\gamma\gamma}$) is recorded. As a π^0 veto, we require $\Delta M_{\gamma\gamma} > 10\ \mathrm{MeV}/c^2$.

A kinematic fit imposing energy-momentum conservation (4C-fit) is applied to the $\Upsilon(2S)$ candidates, which improves the resolution of the signal. Further, the χ^2 of the 4C-fit is used to select the best candidate in case of events with multiple candidate that appear in about 10% of the events in case of the $X_{b\bar{b}}(9975)$ selection.

In Figure 1, the $\Upsilon(2S)$ data after all selection criteria applied are presented in terms of $\Delta M \equiv M[(b\bar{b})\gamma] - M[(b\bar{b})]$. The four signals [$X_{b\bar{b}}(9975)$ and $\chi_{bJ}(1P)$] are parametrized by a sum of a Gaussian and an asymmetric Gaussian functions.

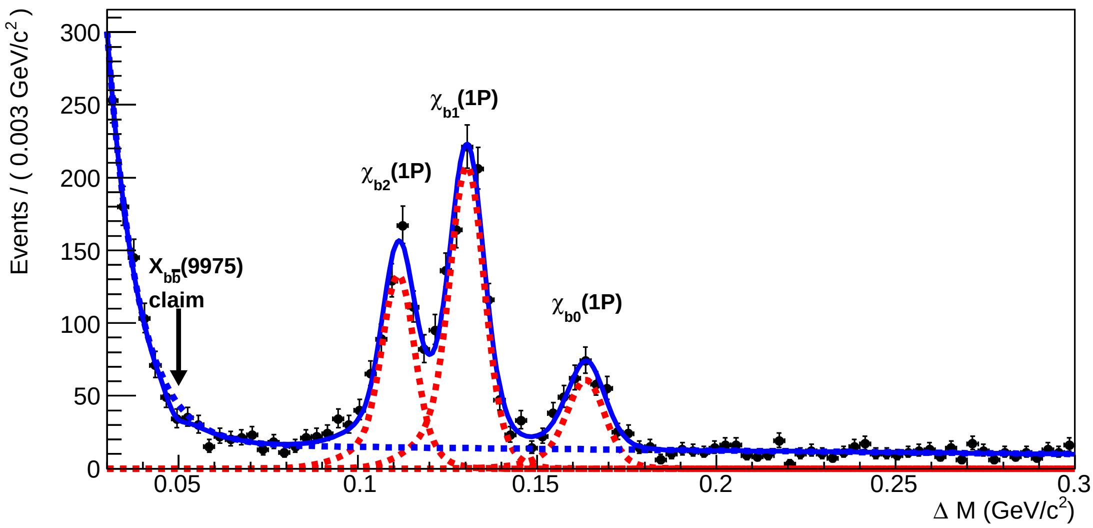

FIGURE 1: ΔM distribution for $\Upsilon(2S)$ data events that pass all the selection criteria. Points with error bars are the data, the blue solid curve is the result of the fit for the signal-plus-background hypothesis, and the blue dashed curve is the background component. The three $\chi_{bJ}(1P)$ components indicated by the red dotted curves are considered here as part of the signal.

The signal shape parameters (the common mean, three widths and relative fraction) are taken from MC samples. A common calibration factor for four signal components is used to account for a modest difference in the detector resolution between data and MC simulations. The background is modeled with a sum of an exponential function and a first-order Chebyshev polynomial shown with the blue dotted curve in Figure 1. The large signal yields for the $\chi_{bJ}(1P)$ are found (300, 950, and 580 events for J=0, 1, and 2, respectively), which allow us to precisely determine the mass of $\chi_{bJ}(1P)$ states to be 9859.63 ± 0.49, 9892.83 ± 0.23, and 9912.00 ± 0.34 MeV/c^2. These results are in good agreement with the world average values [16]. No signal (-30 ± 19 events) is found for the $X_{b\bar{b}}(9975)$ state and hence an upper limit at 90% confidence level (CL) is set on the product branching fraction $\mathcal{B}[\Upsilon(2S) \to X_{b\bar{b}}(9975)\gamma] \times \sum_i \mathcal{B}[X_{b\bar{b}} \to h_i] < 4.9 \times 10^{-6}$, where h_i denotes the i-th hadronic state. Our upper limit on the $X_{b\bar{b}}(9975)$ is an order of magnitude smaller than the product branching fraction measured in the CLEO data.

The $\eta_b(1S)$ signal shape is calibrated with a Breit-Wigner function whose width is fixed to the value obtained in Ref. [2], convolved with a Gaussian function of width 8 MeV/c^2 describing the detector resolution. A first-order Chebyshev polynomial is used for the background in the $\eta_b(1S)$ region. The result of the fit shows no excess for the $\eta_b(1S)$ signal, with a yield of -6 ± 10 events. An upper limit at 90% CL is obtained on the product branching fraction $\mathcal{B}[\Upsilon(2S) \to \eta_b(1S)\gamma] \times \sum_i \mathcal{B}[\eta_b(1S) \to h_i] < 3.7 \times 10^{-6}$.

0.4 Properties of $\chi_{bJ}(1P)$ states

A large signal statistics for $\chi_{bJ}(1P)$ states in our previous analysis motivated us further to study the product branching fractions of $\mathcal{B}[\Upsilon(2S) \to \gamma\chi_{bJ}(1P)] \times \mathcal{B}[\chi_{bJ}(1P) \to h_i]$. The $\chi_{bJ}(1P)$ state can decay to many hadronic final states. As for the charged hadronic final states, we focus on the following 26 modes identical to Ref. [11]:

$2(\pi^+\pi^-)$, $3(\pi^+\pi^-)$, $4(\pi^+\pi^-)$, $5(\pi^+\pi^-)$, $\pi^+\pi^-K^+K^-$, $2(\pi^+\pi^-)K^+K^-$, $3(\pi^+\pi^-)K^+K^-$, $4(\pi^+\pi^-)K^+K^-$, $2(K^+K^-)$, $\pi^+\pi^-2(K^+K^-)$, $2(\pi^+\pi^-K^+K^-)$, $3(\pi^+\pi^-)2(K^+K^-)$, $\pi^+\pi^-p\overline{p}$, $2(\pi^+\pi^-)p\overline{p}$, $3(\pi^+\pi^-)p\overline{p}$, $4(\pi^+\pi^-)p\overline{p}$, $\pi^+\pi^-K^+K^-p\overline{p}$, $2(\pi^+\pi^-)K^+K^-p\overline{p}$, $3(\pi^+\pi^-)K^+K^-p\overline{p}$, $\pi^\pm K^\mp K^0_S$, $\pi^+\pi^-\pi^\pm K^\mp K^0_S$, $2(\pi^+\pi^-)\pi^\pm K^\mp K^0_S$, $3(\pi^+\pi^-)\pi^\pm K^\mp K^0_S$, $\pi^+\pi^-2K^0_S$, $2(\pi^+\pi^-K^0_S)$, and $3(\pi^+\pi^-)2K^0_S$.

One π^0 is added to the above charged final states, excluding $2(\pi^+\pi^-)\pi^0$, $3(\pi^+\pi^-)\pi^0$, $4(\pi^+\pi^-)\pi^0$ and $5(\pi^+\pi^-)\pi^0$ that are forbidden by the G-parity conservation [7]. The following 22 modes with one π^0 are reconstructed:

$\pi^+\pi^-K^+K^-\pi^0$, $2(\pi^+\pi^-)K^+K^-\pi^0$, $3(\pi^+\pi^-)K^+K^-\pi^0$, $4(\pi^+\pi^-)K^+K^-\pi^0$, $2(K^+K^-)\pi^0$, $\pi^+\pi^-2(K^+K^-)\pi^0$, $2(\pi^+\pi^-K^+K^-)\pi^0$, $3(\pi^+\pi^-)2(K^+K^-)\pi^0$, $\pi^+\pi^-p\overline{p}\pi^0$, $2(\pi^+\pi^-)p\overline{p}\pi^0$, $3(\pi^+\pi^-)p\overline{p}\pi^0$, $4(\pi^+\pi^-)p\overline{p}\pi^0$, $\pi^+\pi^-K^+K^-p\overline{p}\pi^0$, $2(\pi^+\pi^-)K^+K^-p\overline{p}\pi^0$, $3(\pi^+\pi^-)K^+K^-p\overline{p}\pi^0$, $\pi^\pm K^\mp K^0_S\pi^0$, $\pi^+\pi^-\pi^\pm K^\mp K^0_S\pi^0$, $2(\pi^+\pi^-)\pi^\pm K^\mp K^0_S\pi^0$, $3(\pi^+\pi^-)\pi^\pm K^\mp K^0_S\pi^0$, $\pi^+\pi^-2K^0_S\pi^0$, $2(\pi^+\pi^-K^0_S)\pi^0$, and $3(\pi^+\pi^-)2K^0_S\pi^0$.

Further 26 modes are reconstructed with an addition of two π^0's to the charged final states mentioned above:

$2(\pi^+\pi^-)2\pi^0$, $3(\pi^+\pi^-)2\pi^0$, $4(\pi^+\pi^-)2\pi^0$, $5(\pi^+\pi^-)2\pi^0$, $(\pi^+\pi^-)K^+K^-2\pi^0$, $2(\pi^+\pi^-)K^+K^-2\pi^0$, $3(\pi^+\pi^-)K^+K^-2\pi^0$, $4(\pi^+\pi^-)K^+K^-2\pi^0$, $2(K^+K^-)2\pi^0$, $\pi^+\pi^-2(K^+K^-)2\pi^0$, $2(\pi^+\pi^-)K^+K^-2\pi^0$, $3(\pi^+\pi^-)2(K^+K^-)2\pi^0$, $\pi^+\pi^-p\overline{p}2\pi^0$, $2(\pi^+\pi^-)p\overline{p}2\pi^0$, $3(\pi^+\pi^-)p\overline{p}2\pi^0$, $4(\pi^+\pi^-)p\overline{p}2\pi^0$, $\pi^+\pi^-K^+K^-p\overline{p}2\pi^0$, $2(\pi^+\pi^-)K^+K^-p\overline{p}2\pi^0$, $3(\pi^+\pi^-)K^+K^-p\overline{p}2\pi^0$, $\pi^\pm K^\mp K^0_S2\pi^0$, $\pi^+\pi^-\pi^\pm K^\mp K^0_S2\pi^0$, $2(\pi^+\pi^-)\pi^\pm K^\mp K^0_S2\pi^0$, $3(\pi^+\pi^-)\pi^\pm K^\mp K^0_S2\pi^0$, $\pi^+\pi^-2K^0_S2\pi^0$, $2(\pi^+\pi^-)2K^0_S2\pi^0$, and $3(\pi^+\pi^-)2K^0_S2\pi^0$.

In total, 74 hadronic decay modes of the $\chi_{bJ}(1P)$ states are reconstructed. For each mode as well as for each of the three $\chi_{bJ}(1P)(J = 0, 1, 2)$ states half a million signal MC events are produced. As in Section 0.3, the decays $\Upsilon(2S) \to \gamma\chi_{bJ}(1P)$ are generated with the helicity amplitude formalism [12] and the hadronic decays of $\chi_{bJ}(1P)(J = 0, 1, 2)$ are modeled with phase space distribution, with an interface to PHOTOS [13].

The analysis procedure begins with the selection of charged particles and reconstruction of K_S^0 similar to the search of $X_{b\bar{b}}(9975)$ [11]. A π^0 is reconstructed from a pair of γ's, each having energy greater than 100 MeV. The reconstructed π^0 should have an invariant mass lying between [113, 157] MeV/c^2, which is $\pm 3.5\sigma$ around the nominal π^0 mass [16]. A $\chi_{bJ}(1P)$ system is formed by combining an appropriate number and type of charged ($\pi^{\pm}, K^{\pm}$ and $p/\overline{p}$) and neutral hadrons(K_S^0 and π^0).

An isolated cluster in the ECL that has an energy greater than 30 MeV and a cluster shape consistent with an electromagnetic shower is selected as a photon candidate. Expected energy of the $\chi_{bJ}(1P)$ signal photon is 110 – 230, 90 – 190, and 80 – 160 MeV for $J = 0,\ 1,$ and 2, respectively. Photons detected only from the barrel part of the ECL are included to suppress the beam-related background. A veto is applied for the photon selected as the radiative decay product, not to come from a π^0 decay.

An $\Upsilon(2S)$ candidate is formed by combining a photon candidate with the $\chi_{bJ}(1P)$ system. To suppress the continuum background, a criterion on $|\cos\theta_T| < 0.8$ is imposed, where θ_T is the angle between the photon candidate and the thrust axis in the event.

In our previous analysis, the 4C-fit is used for improving the signal resolution as well as for the best candidate selection. In addition, the χ^2 from the 4C-fit can be used as a selection criterion for the signal. We have also verified that applying a requirement on the χ^2 is equivalent to applying requirements on the three variables: ΔE, $P^*_{\Upsilon(2S)}$ and $\theta_{\gamma(b\bar{b})}$. Hence, after the preselection and continuum suppression described above, an optimised χ^2 cut is applied for further background suppression. The optimisation is done by using a figure-of-merit $S/\sqrt{S+B}$, where S (B) is the expected signal (background) yield. Signal is estimated by using the branching fractions mentioned in Ref. [7]. We find $\chi^2 < 3$ to be the optimal criterion for signal selection.

After all selection criteria applied, the $\Upsilon(2S)$ data is fitted in terms of $\Delta M \equiv M[(\chi_{bJ}(1P))\gamma] - M[\chi_{bJ}(1P)]$. The fit range of ΔM distribution in data is $(40, 240)$ MeV/c^2, which includes the three $\chi_{bJ}(1P)(J=0,1,2)$ signal components. In data, signal components are parametrised by a sum of a Gaussian and an asymmetric Gaussian functions. The signal shape parameters are taken from MC samples, and a common calibration factor for all three signal components is used to account for the modest difference in the detector resolution between data and MC simulations. The background is modeled by a sum of an exponential function and a first order Chebyshev polynomial. Using a fitting procedure similar to the previous analysis, the ΔM distribution in data is fitted for the sum of all the 74 modes reconstructed. Signal yields for the $\chi_{bJ}(1P)$ (1200, 4750, and 3050 events for J=0, 1, and 2, respectively) found in this analysis is almost 5 times than our earlier analysis. We also find that the angular distribution of the photon in data is in agreement with the helicity amplitude formalism [12] for each signal of $\chi_{bJ}(1P)$ $(J=0,1,2)$.

With signal shape parameters fixed to the values obtained from fitting the ΔM distribution of the sum of 74 modes in data, the ΔM distribution in each mode is fitted and the significance is determined as $\sqrt{-2\ln(\mathcal{L}_0/\mathcal{L}_{max})}$, where $\mathcal{L}_{max}$ and $\mathcal{L}_0$ are likelihoods from the fit in each mode with the signal yield as a free parameter and fixed to zero, respectively. In total, 41 modes are identified that have at least 5σ significance in any of the $\chi_{bJ}(1P)(J=0,1,2)$ signals. The product branching fraction, $\mathcal{B}[\Upsilon(2S) \to \gamma\chi_{bJ}(1P)] \times \mathcal{B}[\chi_{b1}(1P) \to h_i]$, for each $\chi_{bJ}(1P)$ where the significance is greater than 3σ are summarised in Table 1. The branching fractions indicated by the symbol † in the table (in total, 85 of them) are the first observation of the signal in that mode.

TABLE 1: Product branching fraction, $\mathcal{B}[\Upsilon(2S) \to \gamma\chi_{bJ}(1P)] \times \mathcal{B}[\chi_{b1}(1P) \to h_i]$ for each $\chi_{bJ}(1P)(J=0,1,2)$ in units of 10^{-5}. Upper limits at 90% CL are calculated for the modes having a significance less than 3σ. The quoted uncertainties in the table are statistical and systematic, respectively. The table continues to the next page.

Mode	$\boldsymbol{\chi_{b0}(1P)}$	$\boldsymbol{\chi_{b1}(1P)}$	$\boldsymbol{\chi_{b2}(1P)}$
$2\pi^+2\pi^-$	$0.13 \pm 0.05 \pm 0.02$†	$0.3 \pm 0.1 \pm 0.04$†	$0.2 \pm 0.1 \pm 0.02$†
$3\pi^+3\pi^-$	$0.7 \pm 0.1 \pm 0.06$†	$1.8 \pm 0.1 \pm 0.2$	$1 \pm 0.1 \pm 0.1$
$4\pi^+4\pi^-$	$0.8 \pm 0.1 \pm 0.1$†	$2.8 \pm 0.2 \pm 0.4$	$1.8 \pm 0.2 \pm 0.2$
$5\pi^+5\pi^-$	$0.5 \pm 0.1 \pm 0.1$†	$1.5 \pm 0.2 \pm 0.3$†	$1.7 \pm 0.2 \pm 0.3$†
$\pi^+\pi^-K^+K^-$	$0.15 \pm 0.03 \pm 0.03$†	$0.17 \pm 0.03 \pm 0.03$†	$0.15 \pm 0.04 \pm 0.03$†
$2\pi^+2\pi^-K^+K^-$	$0.5 \pm 0.1 \pm 0.1$	$1.2 \pm 0.1 \pm 0.1$	$0.8 \pm 0.1 \pm 0.1$

Product branching fraction, $\mathcal{B}[\Upsilon(2S) \to \gamma\chi_{bJ}(1P)] \times \mathcal{B}[\chi_{bJ}(1P) \to h_i]$ for each $\chi_{bJ}(1P)(J = 0, 1, 2)$ in units of 10^{-5}. Upper limits at 90% CL are calculated for the modes having a significance less than 3σ. The quoted uncertainties in the table are statistical and systematic, respectively. The table continues from the previous page.

Mode	$\boldsymbol{\chi_{b0}(1P)}$	$\boldsymbol{\chi_{b1}(1P)}$	$\boldsymbol{\chi_{b2}(1P)}$
$3\pi^+3\pi^-K^+K^-$	$0.6 \pm 0.1 \pm 0.1$	$1.7 \pm 0.2 \pm 0.2$	$1.2 \pm 0.2 \pm 0.1\dagger$
$4\pi^+4\pi^-K^+K^-$	$1.2 \pm 0.2 \pm 0.2\dagger$	$1.6 \pm 0.2 \pm 0.2\dagger$	$1.6 \pm 0.2 \pm 0.2\dagger$
$\pi^+\pi^-2K^+2K^-$	$0.18 \pm 0.05 \pm 0.02\dagger$	$0.4 \pm 0.1 \pm 0.03\dagger$	$0.3 \pm 0.1 \pm 0.03\dagger$
$2\pi^+2\pi^-2K^+2K^-$	$0.3 \pm 0.1 \pm 0.03\dagger$	$0.6 \pm 0.1 \pm 0.1\dagger$	$0.6 \pm 0.1 \pm 0.1\dagger$
$3\pi^+3\pi^-2K^+2K^-$	$0.3 \pm 0.1 \pm 0.1\dagger$	$0.4 \pm 0.1 \pm 0.1\dagger$	$0.7 \pm 0.2 \pm 0.1\dagger$
$2\pi^+2\pi^-p\overline{p}$	< 0.2	$0.5 \pm 0.1 \pm 0.1\dagger$	$0.2 \pm 0.1 \pm 0.03\dagger$
$3\pi^+3\pi^-p\overline{p}$	$0.2 \pm 0.1 \pm 0.03\dagger$	$0.7 \pm 0.1 \pm 0.1\dagger$	$0.3 \pm 0.1 \pm 0.04\dagger$
$\pi^+\pi^-K^+K^-p\overline{p}$	$0.13 \pm 0.04 \pm 0.02\dagger$	$0.2 \pm 0.1 \pm 0.03\dagger$	$0.2 \pm 0.1 \pm 0.03\dagger$
$2\pi^+2\pi^-K^+K^-p\overline{p}$	$0.3 \pm 0.1 \pm 0.1\dagger$	$0.4 \pm 0.1 \pm 0.1\dagger$	$0.2 \pm 0.1 \pm 0.03\dagger$
$\pi^+\pi^-\pi^\pm K^\mp K^0_S$	< 0.1	$0.7 \pm 0.1 \pm 0.1$	$0.3 \pm 0.1 \pm 0.1\dagger$
$2\pi^+2\pi^-\pi^\pm K^\mp K^0_S$	< 0.4	$1.9 \pm 0.2 \pm 0.2\dagger$	$1.1 \pm 0.2 \pm 0.1\dagger$
$3\pi^+3\pi^-\pi^\pm K^\mp K^0_S$	< 0.7	$1.6 \pm 0.3 \pm 0.1\dagger$	$0.8 \pm 0.2 \pm 0.1\dagger$
$2\pi^+2\pi^-2K^0_S$	$0.2 \pm 0.1 \pm 0.04\dagger$	$0.3 \pm 0.1 \pm 0.03\dagger$	$0.3 \pm 0.1 \pm 0.03\dagger$
$3\pi^+3\pi^-2K^0_S$	< 0.6	$0.5 \pm 0.2 \pm 0.1\dagger$	$0.4 \pm 0.2 \pm 0.1\dagger$
$\pi^+\pi^-K^+K^-\pi^0$	< 0.2	$0.8 \pm 0.1 \pm 0.1$	$0.4 \pm 0.1 \pm 0.04$
$2\pi^+2\pi^-K^+K^-\pi^0$	$0.8 \pm 0.2 \pm 0.2\dagger$	$4.2 \pm 0.3 \pm 0.7$	$2.8 \pm 0.3 \pm 0.5$
$3\pi^+3\pi^-K^+K^-\pi^0$	$1.8 \pm 0.4 \pm 0.4\dagger$	$6.0 \pm 0.6 \pm 1.1$	$3.8 \pm 0.5 \pm 0.7$
$4\pi^+4\pi^-K^+K^-\pi^0$	< 1.7	$4.0 \pm 0.7 \pm 1.0\dagger$	$2.4 \pm 0.6 \pm 0.6\dagger$
$\pi^+\pi^-2K^+2K^-\pi^0$	$0.3 \pm 0.1 \pm 0.1\dagger$	$0.9 \pm 0.2 \pm 0.2\dagger$	$0.5 \pm 0.1 \pm 0.1\dagger$
$2\pi^+2\pi^-2K^+2K^-\pi^0$	$0.7 \pm 0.3 \pm 0.1\dagger$	$1.1 \pm 0.3 \pm 0.2\dagger$	$0.7 \pm 0.3 \pm 0.1\dagger$
$\pi^+\pi^-p\overline{p}\pi^0$	< 0.1	$0.2 \pm 0.1 \pm 0.04\dagger$	$0.1 \pm 0.1 \pm 0.02\dagger$
$\pi^+\pi^-K^+K^-p\overline{p}\pi^0$	< 0.5	$0.5 \pm 0.1 \pm 0.2\dagger$	$0.3 \pm 0.1 \pm 0.1\dagger$
$\pi^+\pi^-\pi^\pm K^\mp K^0_S\pi^0$	< 0.5	$2.2 \pm 0.3 \pm 0.2\dagger$	$1.2 \pm 0.2 \pm 0.2\dagger$
$2\pi^+2\pi^-\pi^\pm K^\mp K^0_S\pi^0$	$1.3 \pm 0.4 \pm 0.2\dagger$	$5.3 \pm 0.6 \pm 0.8$	$2.6 \pm 0.5 \pm 0.5\dagger$
$3\pi^+3\pi^-\pi^\pm K^\mp K^0_S\pi^0$	$2.4 \pm 0.7 \pm 0.5\dagger$	$4.6 \pm 0.8 \pm 1.0\dagger$	$2.9 \pm 0.7 \pm 0.6\dagger$
$2\pi^+2\pi^-2\pi^0$	$0.8 \pm 0.2 \pm 0.2\dagger$	$4.5 \pm 0.4 \pm 1.0$	$3.4 \pm 0.3 \pm 0.8$
$3\pi^+3\pi^-2\pi^0$	$3.6 \pm 0.6 \pm 0.5\dagger$	$16.8 \pm 0.9 \pm 2.3$	$9.7 \pm 0.9 \pm 1.5$
$4\pi^+4\pi^-2\pi^0$	$4.8 \pm 1.0 \pm 1.0\dagger$	$22.3 \pm 1.5 \pm 4.7$	$15.5 \pm 1.5 \pm 3.3$
$5\pi^+5\pi^-2\pi^0$	< 5.1	$10.8 \pm 1.6 \pm 2.4\dagger$	$11 \pm 1.9 \pm 2.5\dagger$
$\pi^+\pi^-K^+K^-2\pi^0$	$0.5 \pm 0.2 \pm 0.1\dagger$	$1.1 \pm 0.2 \pm 0.3\dagger$	$0.9 \pm 0.2 \pm 0.2\dagger$
$2\pi^+2\pi^-K^+K^-2\pi^0$	$1.7 \pm 0.5 \pm 0.4\dagger$	$4.9 \pm 0.6 \pm 1.1$	$3.5 \pm 0.6 \pm 0.8$
$3\pi^+3\pi^-K^+K^-2\pi^0$	$3.2 \pm 1.0 \pm 0.8\dagger$	$8.9 \pm 1.2 \pm 2.2\dagger$	$6.4 \pm 1.2 \pm 1.6\dagger$
$2\pi^+2\pi^-p\overline{p}2\pi^0$	< 1.8	$1.8 \pm 0.5 \pm 0.3\dagger$	$1.6 \pm 0.5 \pm 0.3\dagger$
$\pi^+\pi^-\pi^\pm K^\mp K^0_S2\pi^0$	$2 \pm 0.5 \pm 0.3\dagger$	$3.6 \pm 0.5 \pm 0.4\dagger$	$1.7 \pm 0.5 \pm 0.2$
$2\pi^+2\pi^-\pi^\pm K^\mp K^0_S2\pi^0$	$3 \pm 1.0 \pm 0.6\dagger$	$9.0 \pm 1.3 \pm 1.7\dagger$	$5.1 \pm 1.2 \pm 1.0\dagger$

Our branching fraction results are consistent with the ones observed in CLEO's analysis. Also, a $\chi_{bJ}(1P)(J = 0, 1, 2)$ signal has been observed for the first time in 27, 28 and 30 modes, respectively.

0.5 Research Values and Future Scope

The research outcome of our work gives us confidence in presenting it as my thesis towards the doctoral degree. The disconfirmation of the $X_{b\bar{b}}(9975)$ state was extremely important as its claim to be the $\eta_b(2S)$ was in disagreement with the Belle result and theory predictions. Also, the decay of $\chi_{bJ}(1P)$ in to states of light-quark hadrons tells us how initial quarks and gluons turn into observable hadrons [17]. Our measurement updated the previous study as well as discovered 85 new decay modes. Various theoretical models summarised in Ref. [18], predicts the $\chi_{b0}(1P)$ width can be as large as 2 MeV. Future scope of our analysis is to measure the width of $\chi_{b0}(1P)$ for the first time from the sum of 41 hadronic modes.

Though my thesis is mainly focused on the physics analysis of Belle data, as a collaborator of the Belle II experiment I am also participating in the assembly of the layer-4 of its silicon vertex detector. My task is to perform and optimize gluing operations between the pitch adapters and silicon sensors. Apart from gluing, I am also involved in aligning sensors during the module assembly using a precision three-dimensional coordinate measuring machine.

Bibliography

[1] B. Aubert *et al.* (BaBar Collaboration), Phys. Rev. Lett. **101**, 071801 (2008).

[2] R. Mizuk *et al.* (Belle Collaboration), Phys. Rev. Lett. **109**, 232002 (2012).

[3] S. Dobbs, Z. Metreveli, A. Tomaradze, T. Xiao, and K. Seth, Phys. Rev. Lett. **109**, 082001 (2012).

[4] T. J. Burns, Phys. Rev. D **87**, 034022 (2013).

[5] R. J. Dowdall *et al.*, arXiv:1309.5797v1 [hep-lat]

[6] G. Aad *et al.* (ATLAS Collaboration), Phys. Rev. Lett. **108**, 152001 (2012).

[7] D.M. Asner *et al.* (CLEO Collaboration), Phys. Rev. D **78**, 091103(R) (2008).

[8] A. Abashian *et al.* (Belle Collaboration), Nucl. Instrum. Methods Phys. Res., Sect. A **479**, 117 (2002); also, see the detector section in J. Brodzicka *et al.*, Prog. Theor. Exp. Phys., 04D001 (2012).

[9] S. Kurokawa and E. Kikutani, Nucl. Instrum. Methods Phys. Res., Sect. A **499**, 1 (2003), and other papers included in this volume; T. Abe *et al.*, Prog. Theor. Exp. Phys., 03A001 (2013) and following articles up to 03A011.

[10] T. Sjöstrand *et al.*, Comput. Phys. Commun. **178**, 852 (2008).

[11] S. Sandilya *et al.* (Belle Collaboration), Phys. Rev. Lett. **111**, 112001 (2013).

[12] M. Jacob and G. C. Wick, Annals Phys. **7**, 404 (1959); Annals Phys. **281**, 774 (2000).

[13] E. Barberio and Z. Wąs, Comput. Phys. Commun. **79**, 291 (1994); P. Golonka and Z. Wąs, Eur. Phys. J. C **45**, 97 (2006); P. Golonka and Z. Wąs, Eur. Phys. J. C **50**, 53 (2007).

[14] K.-F. Chen *et al.* (Belle Collaboration), Phys. Rev. D **72**, 012004 (2005).

[15] B. Aubert *et al.* (BaBar Collaboration), Phys. Rev. Lett. **103**, 161801 (2009).

[16] K. A. Olive *et al.* (Particle Data Group), Chin. Phys. C **38**, 090001 (2014).

[17] C. Patrignani, T.K. Pedlar and J.L. Rosner , Annu. Rev. Nucl. Part. Sci. **63**, 21-44 (2013).

[18] C.W. Hwang and R.S. Guo, Phys. Rev. D **82**, 034021 (2010).

List of Publications

(List of publications relevant to the thesis work)

Journals

- **'Search for Bottomonium States in Exclusive Radiative $\Upsilon(2S)$ Decays'**
  S. Sandilya *et al.* [Belle Collaboration].
  arXiv:1306.6212 [hep-ex]
  Phys. Rev. Lett. **111**, 112001 (2013)

- **'Evidence for the $\eta_b(2S)$ and observation of $h_b(1P) \to \eta_b(1S)\gamma$ and $h_b(2P) \to \eta_b(1S)\gamma$'**
  R. Mizuk *et al.* [Belle Collaboration].
  arXiv:1205.6351 [hep-ex]
  Phys. Rev. Lett. **109**, 232002 (2012)

Proceedings

- **'Exclusive Study of Bottomonium States in Radiative $\Upsilon(2S)$ Decays'**
  S. Sandilya
  arXiv:1401.4695 [hep-ex]
  PoS Hadron **2013**, 080 (2013)

Belle Notes (internal)

- **'Search for Bottomonium States in $\Upsilon(2S) \to \gamma(b\bar{b})$'**
  S. Sandilya, K. Trabelsi, and G. B. Mohanty,
  Belle Note # 1248

- **'Study of $\chi_{bJ}(1P)$ properties using the radiative decay of $\Upsilon(2S)$'**
  S. Sandilya, G. B. Mohanty, and K. Trabelsi.
  Belle Note # 1333

List of Figures

List of Tables

Contents

CHAPTER 1

Introduction

Bottomonium, the bound system of a bottom quark (b) and a bottom antiquark ($\bar{b}$), in a similitude with the positronium or even with the hydrogen atom, exhibits several energy levels or resonances. It offers a unique laboratory to study strong interactions as the b quark is heavier[1] than other quarks (u, d, s, c), thence can be well described by the non-relativistic quantum mechanics.

This thesis presents a study of radiative transitions between various bottomonium states and their decays to several hadronic final states, based on the data recorded with the Belle detector located at the KEKB asymmetric-energy e^+e^- collider. In this chapter, a theoretical context of the bottomonium and its discovery is briefly introduced followed by the recent experimental findings that are related to and have motivated our thesis work.

1.1 Bottomonium: Theory

Two-particle bound states have played an important role in improving our understanding about the fundamental interactions [1]. Starting from the hydrogen atom – a bound state of an electron and a proton – from which quantum mechanics developed, the deuteron, a bound state of a neutron and a proton, played a crucial role in advancement of our knowledge of nuclear force. Study of the electron-positron bound states or positronium energy levels is essential for the verification of quantum electrodynamics (QED) and quantum field theory of electromagnetic

[1]The top quark, the heaviest among the known quarks, decays before it can hadronize.

interactions. Similarly, *bottomonium* provides a resourceful ground to test the theory of strong interactions.

Starting with the case of positronium, where the potential between the bound fermions has an electromagnetic form,

$$V_{\text{em}} = -\frac{\alpha}{r}, \tag{1.1}$$

where r is the distance between the electron and positron, and α is the fine structure constant. Its principal energy levels can be derived using the non-relativistic Schrödinger equation as in case of the hydrogen atom,

$$E_n = -\frac{\alpha^2 \mu c^2}{2n^2}, \tag{1.2}$$

where n is the principal quantum number, c is the velocity of light, and $\mu = m_e m_p/(m_e + m_p)$ is the reduced mass with m_e and m_p being the mass of an electron and a proton, respectively. In case of positronium, $\mu = m_e/2$ and Eq. 1.2 can thus be written for positronium as,

$$E_n = -\frac{\alpha^2 m_e c^2}{4n^2}. \tag{1.3}$$

Relativistically, energy levels are split by the spin-orbit interaction (fine structure splitting) as well as by the spin-spin interaction (hyperfine splitting) [2]. The level schemes of positronium and bottomonium have a remarkable similarity, although in case of bottomonium (or, quarkonium in general) the exact form of the potential is yet to be understood. The shape of the potential at smaller distance between the quarks (r) can be pursued by the perturbation theories of quantum chromodynamics (QCD). At its lowest order, the strong interaction is mediated by the massless vector gluons, and this picture is similar to QED that is mediated by the massless vector photons. For larger distances, a linear variation of the potential describes well the experimental observations. One of the most popular models is the *Cornell potential* which is the sum of a Coulomb-type and a linear term [3, 4], given by,

$$V_{\text{QCD}} = -\frac{4}{3}\frac{\alpha_s}{r} + \kappa r, \tag{1.4}$$

where α_s is the strong coupling constant, the factor $4/3$ appears as the color factor, and κ is the slope of the linear term. The Cornell potential is plotted as a function of r in Figure 1.1, where values of $\alpha_s = 0.2$ and $\kappa = 1$ GeV fm^{-1} are assumed.

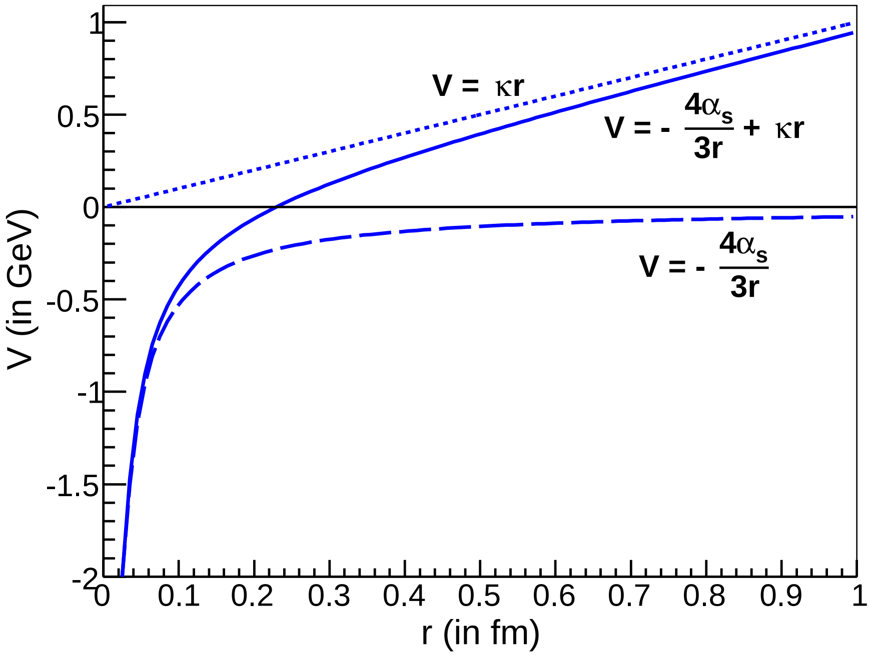

FIGURE 1.1: Cornell potential as a function of distance, the blue dashed curve represents the Coulomb-type term for smaller distance, the blue dotted line denotes the linear term, and the blue solid curve is the combination of the two.

The energy-level diagram of the bottomonium states is shown in Figure 1.2. These $(b\bar{b})$ states are characterized by their spin $S = 0$ or 1, owing to an antiparallel or a parallel configuration of b and $\bar{b}$ spins, orbital angular momentum (L), and total angular momentum (J) that is the vector sum of L and S. In the spectroscopic notation a state can be denoted as $n^{2S+1}L_J$, where $n = 1, 2, 3, \ldots$ is the principal quantum number for radial excitations, and the notations $S, P, D, \ldots$ are used for $L = 0, 1, 2, \ldots$, respectively. The parity (P) of the state is determined from its L value as $P = (-1)^{L+1}$, because the spherical harmonics have parity $(-1)^L$ and an extra -1 factor appears due to the opposite intrinsic parity of a fermion and an antifermion, b and $\bar{b}$ in this case. For the $(b\bar{b})$ system, symmetry under particle exchange for the spin wave function is $(-1)^{S+1}$ and that for the spatial wavefunction is $(-1)^{L+1}$. Thus the total symmetry under exchange of spin and space, which is an equivalent of the charge conjugation operation C, is $(-1)^{L+S}$ [2]. The states are also often referred to by their J^{PC} quantum numbers.

The singlet states with $L = 0$, n^1S_0, are known as $\eta_b(nS)$ with $\eta_b(1S)$ being the bottomonium ground state. Vector mesons with $L = 0$, n^3S_1, have $J^{PC} = 1^{--}$ are called $\Upsilon(nS)$. The P-wave singlets and triplets are known as $h_b(nP)$ and $\chi_{bJ}(nP)(J = 0, 1, 2)$, respectively.

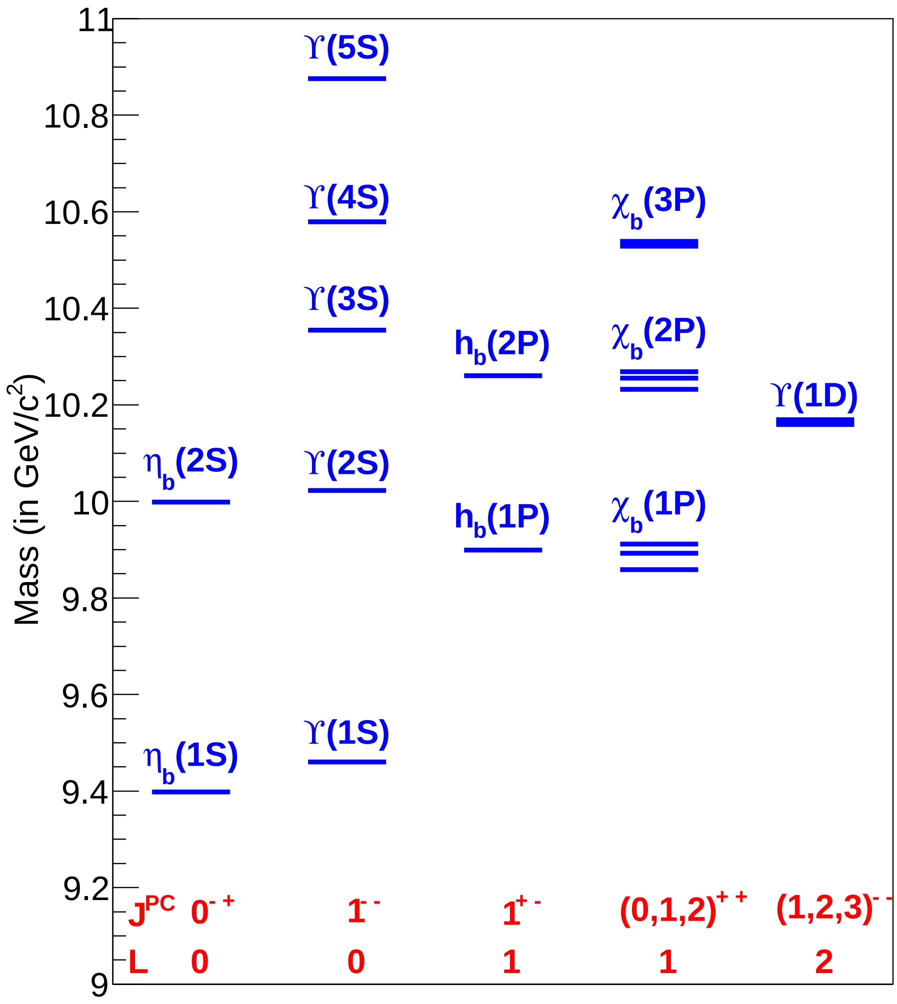

FIGURE 1.2: Experimentally known bottomonium states are shown by blue horizontal lines. Their J^{PC} values depending upon the spin and orbital momentum are given in red texts. The $\chi_{bJ}(3P)$ and $\Upsilon(1D)$ states are shown by thicker lines as their splitting are not yet observed.

The significance of relativistic effects in quarkonia can be approximately estimated from the mass of resonances [5],

$$\frac{v^2}{c^2} \sim \frac{\Delta M}{M} \tag{1.5}$$

where for bottomonia, ΔM is the mass difference between the $\Upsilon(2S)$ and $\Upsilon(1S)$ states, and M is the $\Upsilon(1S)$ mass. The relativistic term for bottomonia is ~ 0.08

Table 1.1: Comparison of the relativistic term v^2/c^2 between various quarkonium systems.

System	Ground triplet state (1^3S_1)		v^2/c^2
	Name	Mass (MeV/c^2)	
$u\bar{u}$, ($d\bar{d}$)	ρ	770	~ 1.0
$s\bar{s}$	ϕ	1020	~ 0.8
$c\bar{c}$	J/ψ	3100	~ 0.2
$b\bar{b}$	Υ	9460	~ 0.08

and its comparison with other quarkonium systems is done in Table 1.1. Not being overly complicated by relativistic effects, the bottomonium system provides an ideal tool to study the inter-quark dynamics.

The non-relativistic potential model in the Eq. 1.4 is further extended to include spin-dependent interactions that results in three additional type of terms: (1) spin-orbit interaction, (2) tensor interaction, and (3) spin-spin interaction. Description of these terms and their forms are discussed in Refs. [1, 5, 6]. The spin-orbit and tensor interactions give rise to the fine structure splitting of a state, while the spin-spin interaction results in the hyperfine splitting between spin-singlet and -triplet states.

1.2 Bottomonium: Experiment

The first evidence of the bottomonium was found by the E288 Collaboration in 1977 at Fermilab [7]. The $\Upsilon(1S)$ and its radially excited state were observed while analyzing the spectrum of $\mu^+\mu^-$ pairs produced in the collision of 400 GeV/c proton with copper nuclei. These were the first particles containing a bottom quark to be discovered.

Bottomonia can also be produced in e^+e^- collisions, when the total center-of-mass (CM) energy is close to the resonance mass. The positron and electron annihilate giving rise to a virtual photon of which $\Upsilon(nS)$ states can be directly produced as they have $J^{PC} = 1^{--}$, same as that of the photon. The Feynman diagram for the corresponding process is shown in Figure 1.3.

The measured cross-section of the process $e^+e^- \to$ hadrons *vs.* the total CM energy near the 10 GeV region by the CUSB detector is shown in Figure 1.4. The

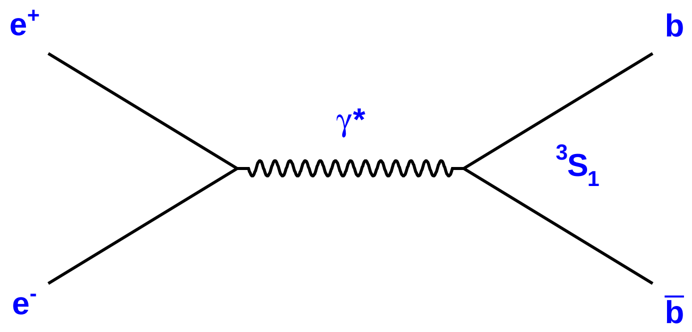

FIGURE 1.3: Feynman diagram for the process $e^+e^- \to \gamma^\star \to \Upsilon(nS)$.

four peaking structures in the plot correspond to various $\Upsilon(nS)$ states. In e^+e^- collisions other bottomonium states are mostly produced from the $\Upsilon(nS)$ decays. Experimental status of these states are described in the following subsections.

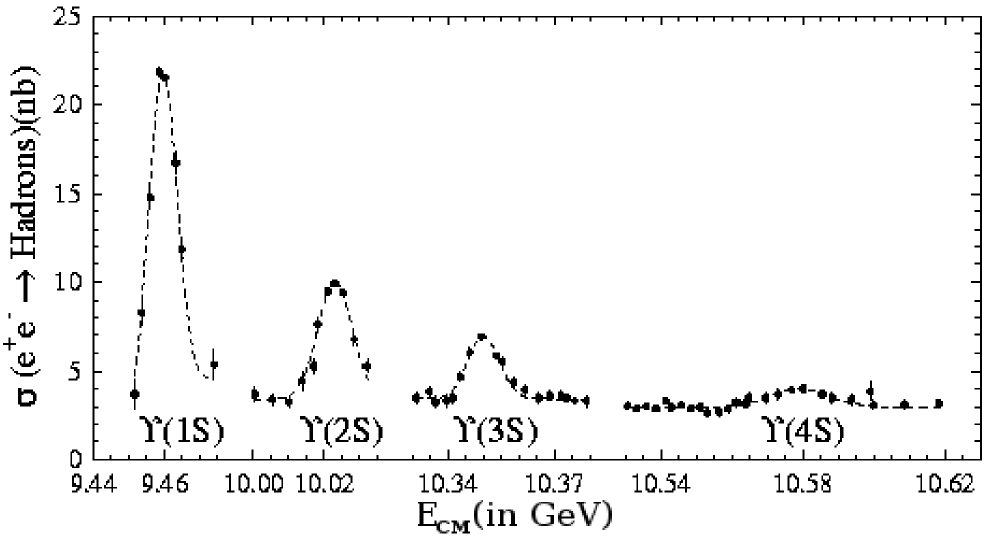

FIGURE 1.4: Cross-section of $e^+e^- \to$ hadrons *vs.* the total CM energy near 10 GeV region [8].

1.2.1 $\chi_{bJ}(1P)$ States

The P-wave spin triplet states of bottomonia, $\chi_{bJ}(nP)$, especially the $\chi_{bJ}(1P)$ and $\chi_{bJ}(2P)$ states are discovered by the CUSB Collaboration at the CESR e^+e^- collider [9–12] nearly 30 years ago. They can be promptly produced from the $\Upsilon(nS)$ states through electric dipole (E1) radiative transitions. Similarly they can also decay to lower $\Upsilon(nS)$ states through E1 transitions. Branching fractions [for states below $\Upsilon(4S)$] of these decays are listed in Table 1.2.

TABLE 1.2: Branching fractions of the radiative $\Upsilon(nS)$ decays to $\chi_{bJ}(mP)$ $(n > m)$ (top), and $\chi_{bJ}(nP)$ decays to $\Upsilon(mS)$ $(n \geq m)$ radiatively (bottom). These values (in %) are taken from the Particle Data Group [13]

.

Decay mode	$J = 0$	$J = 1$	$J = 2$
$\Upsilon(3S) \to \gamma\chi_{bJ}(2P)$	5.9 ± 0.6	12.6 ± 1.2	13.1 ± 1.6
$\Upsilon(3S) \to \gamma\chi_{bJ}(1P)$	–	–	0.99 ± 0.13
$\Upsilon(2S) \to \gamma\chi_{bJ}(1P)$	3.8 ± 0.4	6.9 ± 0.4	7.15 ± 0.35

Decay mode	$J = 0$	$J = 1$	$J = 2$
$\chi_{bJ}(2P) \to \gamma\Upsilon(2S)$	4.6 ± 2.1	19.9 ± 1.9	10.6 ± 2.6
$\chi_{bJ}(2P) \to \gamma\Upsilon(1S)$	0.9 ± 0.6	9.2 ± 0.8	7.0 ± 0.7
$\chi_{bJ}(1P) \to \gamma\Upsilon(1S)$	1.76 ± 0.35	33.9 ± 2.2	19.1 ± 1.2

These states can also be produced in hadronic interactions, via dominant gluon fusion to form a C-even $\chi_{bJ}(nP)$ state, which further can decay radiatively to $\Upsilon(mS)$ states as illustrated in Figure 1.5.

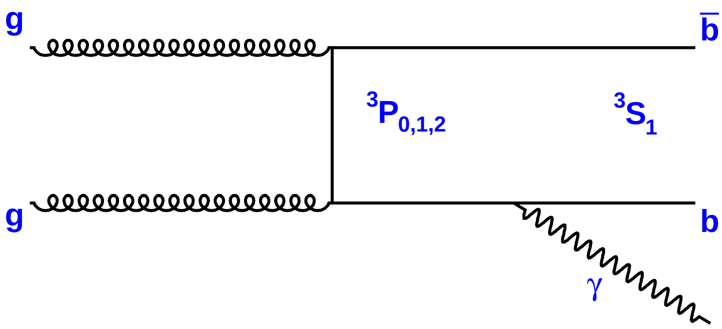

FIGURE 1.5: Feynman diagram of a possible mechanism of the χ_{bJ} production at hadron colliders with its subsequent radiative decays to Υ state.

Recently, the $\chi_{bJ}(3P)$ state was first observed at the large hadron collider (LHC) by the ATLAS Collaboration [14], and later confirmed by DØ [15] and LHCb [16].

Among the χ_{bJ} states, χ_{b0} and χ_{b2} can annihilate via two real photons or gluons. In contrast, according to the Landau-Yang theorem a $J = 1$ particle cannot decay to two identical massless spin-1 bosons, so the $\chi_{b1}(1P)$ cannot decay to two real gluons or photons. Note that this process can occur if one of the gluons is virtual giving rise to a quark-antiquark pair [1]. Most of the theoretical calculations concern the two-gluon width ($\Gamma_{\text{total}} \approx \Gamma_{2g}$) of the $\chi_{b0}(1P)$ ($J^{\text{PC}} = 0^{++}$) and $\chi_{b2}(1P)$ ($J^{\text{PC}} = 2^{++}$) states. The ratio of the two-gluon annihilation rate of a

0^{++} to 2^{++} state, in the approximation of zero binding, is

$$\Gamma_{2g}(0^{++})/\Gamma_{2g}(2^{++}) = 15/4, \tag{1.6}$$

which is independent of any parameter [17]. Various theoretical calculations for the $\chi_{b0}(1P)$ and $\chi_{b2}(1P)$ decay widths are summarised in Table 1.3. All of them predict the width of $\chi_{b0}(1P)$ to be larger than that of $\chi_{b2}(1P)$. On the experimental front also, in the charmonium family, the width of $\chi_{c0}(1P)$ is measured to be 10.3 ± 0.6 MeV, compared to a $\chi_{c2}(1P)$ width of 1.97 ± 0.11 MeV [13]. Not a single measurement exists for the width of any $\chi_{bJ}(1P)$.

Table 1.3: Theoretical predictions for two-gluon decay widths in keV of the $\chi_{b0}(1P)$ and $\chi_{b2}(1P)$ states assuming $\Gamma_{\text{total}} \approx \Gamma_{2g}$.

$\Gamma[\chi_{b0}(1P)]$	$\Gamma[\chi_{b2}(1P)]$	Theoretical approach used	Ref.
431^{+45}_{-49}	214^{+1}_{-0}	Covariant light-front approach	[18]
887	220	Relativistic (Salpeter method) corrections	[19, 20]
960(2740)	330(250)	Perturbative (nonperturabtive) calculations	[21]
653	109	Relativistic quark model	[22]
2150(2290)	220(330)	QCD potential (alternative treatment)	[23]
672	123	Relativistic quark model	[24]

In 2008, the CLEO Collaboration reported the first observations of the $\chi_{bJ}(1P)$ and $\chi_{bJ}(2P)$ decays into specific final states of light hadrons, where these states are produced in the radiative transitions of the $\Upsilon(2S)$ and $\Upsilon(3S)$ resonances, respectively [25]. CLEO used a data sample corresponding to $(9.3 \pm 0.1) \times 10^6$ $\Upsilon(2S)$ and $(5.9 \pm 0.1) \times 10^6$ $\Upsilon(3S)$ decays. In that analysis, the $\chi_{bJ}(1P)$ and $\chi_{bJ}(2P)$ are reconstructed from a combination of 12 or fewer particles, defined as a photon, $\pi^{\pm}$, $K^{\pm}$, $p/\overline{p}$, and K^0_S (photons must be paired into either a π^0 or a η). Out of the total 659 modes reconstructed, 14 modes were identified having at least a significance of 5 standard deviations (σ) from both $\chi_{bJ}(1P)$ and $\chi_{bJ}(2P)$ decays. The left plot in Figure 1.6 is the invariant mass distribution from the sum of 659 reconstructed modes, whereas the right plot is the invariant-mass distribution from the sum of 14 significant modes. The branching fractions for these modes are listed in Table 1.4.

These results motivated us to study the hadronic decays of $\chi_{bJ}(1P)$ in the dataset recorded by Belle experiment at the $\Upsilon(2S)$ resonance, which is the world's largest

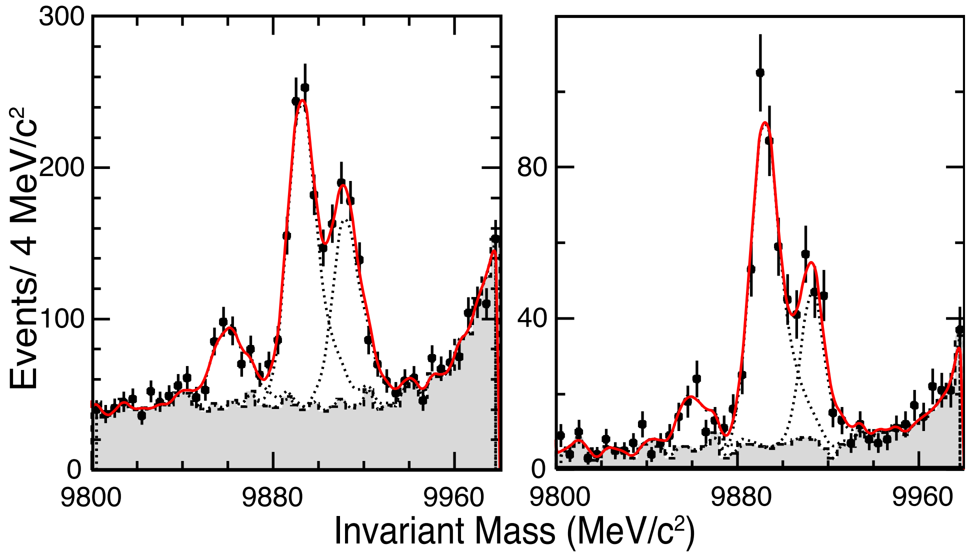

FIGURE 1.6: Invariant mass distributions in CLEO data, from the sum of 659 reconstructed hadronic modes (left) and the sum of 14 significant modes (right). The plot is taken from Ref. [25].

e^+e^- collision data near that resonance. We can not only improve the measurements made by CLEO but can also discover many new hadronic decay modes. Our study is discussed in detail Chapter 4 where we have obtained a large signal yield of $\chi_{bJ}(1P)$.

1.2.2 $h_b(nP)$ States

The hyperfine splitting at leading order is proportional to the square of the wave-function at the origin, which vanishes for the P-wave states [26, 27]. Hence, the P-wave spin singlet states, $h_b(nP)$, are expected to have a mass closer to the spin-weighted average mass of the P-wave triplet $\chi_{bJ}(nP)$ states, $\langle M(n^3P_J)\rangle = [5M(n^3P_2) + 3M(n^3P_1) + M(n^3P_0)]/9$.

The Belle Collaboration reported the first observation of the $h_b(1P)$ and $h_b(2P)$ states in a 121.4 fb^{-1} data sample collected near the $\Upsilon(5S)$ resonance [28], with anomalously high signal yields. These states are observed in the $\pi^+\pi^-$ missing mass (M_{miss}) spectrum, $M_{miss} = \sqrt{[P_{\Upsilon(5S)} - P_{\pi^+\pi^-}]^2}$, where $P_{\Upsilon(5S)}$ is the four-momentum of the $\Upsilon(5S)$ determined from the beam momenta and $P_{\pi^+\pi^-}$ is the four-momentum of the $\pi^+\pi^-$ system. The background-substracted M_{miss} spectrum is shown in Figure 1.7. The peaks in the data distributions from left to right are due to $\Upsilon(5S) \to \Upsilon(1S)\pi^+\pi^-$, $\Upsilon(5S) \to h_b(1P)\pi^+\pi^-$, $\Upsilon(3S) \to \Upsilon(1S)\pi^+\pi^-$,

TABLE 1.4: Values of product branching fractions ($\mathcal{B}[\Upsilon(2S) \to \gamma\chi_{bJ}(1P)] \times \mathcal{B}[\chi_{bJ}(1P) \to h_i]$) in units of 10^{-5}. Upper limits at 90% C.L. are set for the modes with less than 3σ.

Modes	$\mathcal{B}_{\Upsilon(2S)\to\gamma\chi_{bJ}(1P)} \times \mathcal{B}_{\chi_{bJ}(1P)\to h_i}(10^{-5})$		
	$\chi_{b0}(1P)$	$\chi_{b1}(1P)$	$\chi_{b2}(1P)$
$\pi^+\pi^-K^+K^-\pi^0$	< 0.6	$1.4 \pm 0.3 \pm 0.3$	$0.6 \pm 0.3 \pm 0.2$
$\pi^+\pi^-\pi^\pm K^\mp K^0_S$	< 0.2	$0.9 \pm 0.3 \pm 0.2$	< 0.7
$\pi^+\pi^-\pi^\pm K^\mp K^0_S 2\pi^0$	< 1.8	< 4.2	$3.8 \pm 1.4 \pm 1.0$
$2\pi^+2\pi^-2\pi^0$	< 0.8	$5.5 \pm 0.9 \pm 1.4$	$2.5 \pm 0.8 \pm 0.6$
$2\pi^+2\pi^-K^+K^-$	$0.4 \pm 0.2 \pm 0.1$	$1.0 \pm 0.3 \pm 0.2$	$0.8 \pm 0.2 \pm 0.2$
$2\pi^+2\pi^-K^+K^-\pi^0$	< 1.0	$2.4 \pm 0.6 \pm 0.6$	$1.5 \pm 0.5 \pm 0.4$
$2\pi^+2\pi^-K^+K^-2\pi^0$	< 2.0	$5.9 \pm 1.4 \pm 1.7$	$2.8 \pm 1.1 \pm 0.7$
$2\pi^+2\pi^-\pi^\pm K^\mp K^0_S\pi^0$	< 0.6	$6.4 \pm 1.6 \pm 1.6$	< 3.6
$3\pi^+3\pi^-$	< 0.3	$1.3 \pm 0.3 \pm 0.3$	$0.5 \pm 0.2 \pm 0.1$
$3\pi^+3\pi^-2\pi^0$	< 2.2	$11.9 \pm 1.8 \pm 3.2$	$7.3 \pm 1.6 \pm 2.0$
$3\pi^+3\pi^-K^+K^-$	$0.9 \pm 0.4 \pm 0.2$	$1.8 \pm 0.4 \pm 0.4$	< 0.6
$3\pi^+3\pi^-K^+K^-\pi^0$	< 3.7	$5.2 \pm 1.1 \pm 1.1$	$2.6 \pm 0.8 \pm 0.7$
$4\pi^+4\pi^-$	< 0.3	$1.8 \pm 0.4 \pm 0.5$	$0.6 \pm 0.2 \pm 0.2$
$4\pi^+4\pi^-2\pi^0$	< 7.7	$9.6 \pm 2.4 \pm 2.9$	$13.2 \pm 3.1 \pm 4.0$

$\Upsilon(5S) \to \Upsilon(2S)\pi^+\pi^-$, $\Upsilon(5S) \to \Upsilon(1D)\pi^+\pi^-$, $\Upsilon(5S) \to h_b(2P)\pi^+\pi^-$, $\Upsilon(2S) \to \Upsilon(1S)\pi^+\pi^-$, and $\Upsilon(5S) \to \Upsilon(3S)\pi^+\pi^-$, respectively, where $\Upsilon(3S)$ and $\Upsilon(2S)$ are produced either inclusively in the $\Upsilon(5S)$ decays, or via initial state radiation and later decay to $\Upsilon(1S)\pi^+\pi^-$. The mass of $h_b(1P)$ and $h_b(2P)$ states are measured as $9898.2^{+1.1+1.0}_{-1.0-1.1}$ MeV/c^2 and $10259.8 \pm 0.6^{+1.4}_{-1.0}$ MeV/c^2 at a significance of 5.5σ and 11.2σ, respectively. The corresponding P-wave hyperfine splittings are consistent with zero as per theory prediction, $\Delta M_{HF}(1P) = +1.7 \pm 1.5$ MeV/c^2 and $\Delta M_{HF}(2P) = +0.5^{+1.6}_{-1.2}$ MeV/c^2, where $\Delta M_{HF}(nP) = \langle M(n^3P_J)\rangle - M(n^1P_1)$. Furthermore, the productions of $h_b(1P)$ and $h_b(2P)$ are not suppressed relative to the productions of $\Upsilon(1S)$, $\Upsilon(2S)$, and $\Upsilon(3S)$ despite the fact that the former requires a spin flip of a b quark.

1.2.3 $\eta_b(nS)$ States

Mass of the S-wave spin singlet states provides the hyperfine splitting from their spin triplet states, $\Delta M_{HF}(nS) = M[\Upsilon(nS)] - M[\eta_b(nS)]$, which in turn constitutes an important piece of information about spin-spin interactions between the quark

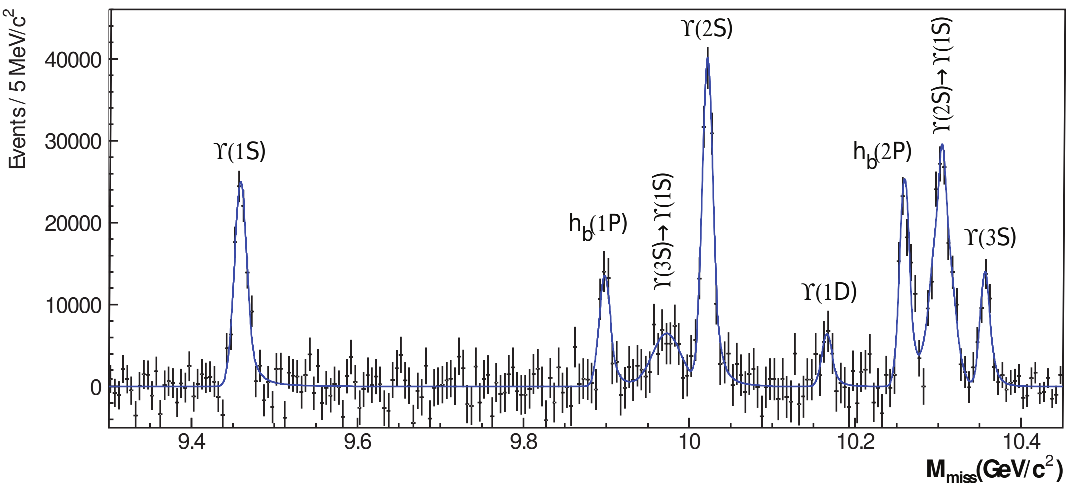

FIGURE 1.7: Missing mass spectrum against $\pi^+\pi^-$ in the data recorded with the Belle detector at $\Upsilon(5S)$ resonance. The plot is taken from Ref. [28].

and antiquark. The ground state of bottomonia, $\eta_b(1S)$, was discovered in 2008 by the BaBar Collaboration in the radiative transition $\Upsilon(3S) \to \gamma\eta_b(1S)$ [29]. This was followed by observations in $\Upsilon(2S) \to \gamma\eta_b(1S)$ by BaBar [30] and in $\Upsilon(3S) \to \gamma\eta_b(1S)$ by CLEO [31]. The large signal yield of $h_b(nP)$ seen by the Belle experiment [28] (discussed in Section 1.2.2), opened a new perspective to study the $\eta_b(nS)$ states. Belle reported the first evidence for the $\eta_b(2S)$ and the most precise mass measurement of $\eta_b(1S)$ including its width for the first time [32]. A 133.4 fb^{-1} data sample collected near the $\Upsilon(5S)$ resonance is used to study the process $e^+e^- \to \Upsilon(5S) \to h_b(nP)\pi^+\pi^-, h_b(nP) \to \eta_b(mS)\gamma$ for $n \geq m = 1$ and 2, in which the $\eta_b(mS)$ states are not exclusively reconstructed. To identify signal events, only a photon and $\pi^+\pi^-$ pair are reconstructed and a missing mass against $\Upsilon(5S)$ is defined as $M_{miss}(X) = \sqrt{(E_{\mathrm{CM}} - E_X^\star)^2 - p_X^{\star 2}}$, where E_{CM} is the CM energy, and E_X^* and p_X^* are the energy and momentum of the recoiling system X measured in the CM frame. The missing mass against the $\pi^+\pi^-$ pair, $M_{miss}(\pi^+\pi^-)$, is used in selecting $h_b(nP)$ signal events, while the $\eta_b(mS)$ signal is identified with the variable, $M_{miss}^{(n)}(\pi^+\pi^-\gamma) = M_{miss}(\pi^+\pi^-\gamma) - M_{miss}(\pi^+\pi^-) + m_{h_b(nP)}$. The $h_b(nP)$ yield *vs.* $M_{miss}^{(n)}(\pi^+\pi^-\gamma)$ distribution is shown in Figure 1.8, where the peak near 9.4 GeV/c^2 is identified as the $\eta_b(1S)$.

The mass of the $\eta_b(1S)$ state is measured as $9402.4 \pm 1.5 \pm 1.8$ MeV/c^2, which is the most precise measurement till date. The corresponding hyperfine splitting $[\Delta M_{HF}(1S)]$ is 57.9 ± 2.3 MeV/c^2. Its comparison with other experimental results and theoretical predictions is shown in Figure 1.9. The $\eta_b(1S)$ width is also measured in the same analysis and found to be $10.8^{+4.0+4.5}_{-3.7-2.0}$ MeV.

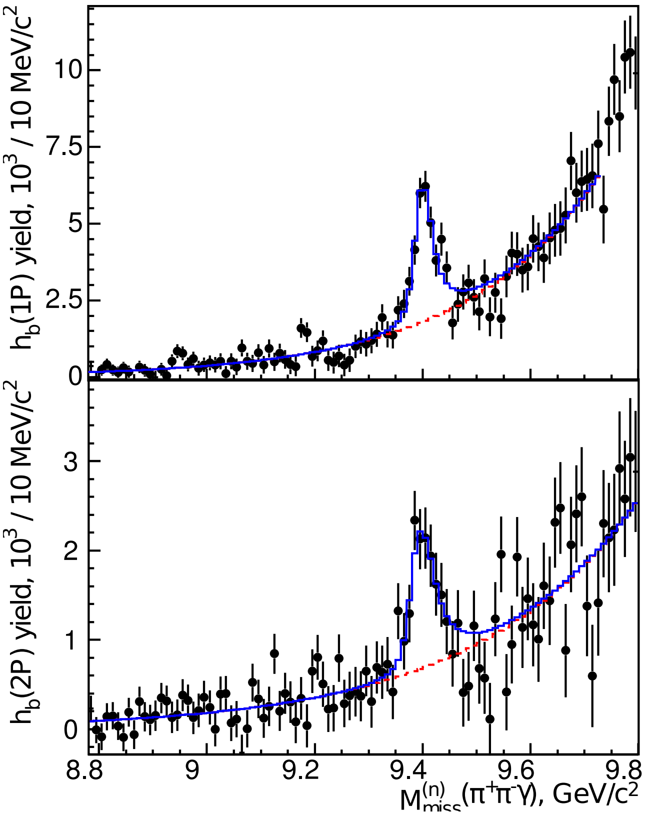

FIGURE 1.8: $h_b(1P)$ yield *vs.* $M^{(1)}_{miss}(\pi^+\pi^-\gamma)$ (top), and $h_b(2P)$ yield *vs.* $M^{(2)}_{miss}(\pi^+\pi^-\gamma)$ (bottom) distribution in the $\eta_b(1S)$ region. Points with error bars are the data, blue solid histograms are the result from a fit and the red dashed histograms are the background component of the fit. The plot is taken from Ref. [32].

The $h_b(2P)$ yield *vs.* $M^{(2)}_{miss}(\pi^+\pi^-\gamma)$ distribution is shown in Figure 1.10, where the peak near $10.0\,\mathrm{GeV}/c^2$ is identified as the $\eta_b(2S)$. The significance of the $\eta_b(2S)$ signal is 4.2σ and its mass is $9999.0 \pm 3.5^{+2.8}_{-1.9}\,\mathrm{MeV}/c^2$, which corresponds to a hyperfine splitting for $2S$, $\Delta M_{HF} = 24.3^{+4.0}_{-4.5}\,\mathrm{MeV}/c^2$.

1.2.4 $X_{b\bar{b}}(9975)$ State

There is a recent claim of observation of a bottomonium state, $X_{b\bar{b}}(9975)$, in the radiative $\Upsilon(2S)$ decay based on an analysis performed on a data sample of 9.3×10^6 $\Upsilon(2S)$ decays recorded with the CLEO detector [35]. The $X_{b\bar{b}}(9975)$ state is exclusively reconstructed in 26 hadronic final states, and is measured with a significance of about 5σ at a mass of $9974.6 \pm 2.3(\mathrm{stat.}) \pm 2.1(\mathrm{syst.})$ MeV/c^2. Figure 1.11 shows the distribution of the variable $\Delta M = M[\Upsilon(2S)] - M[(b\bar{b})]$,

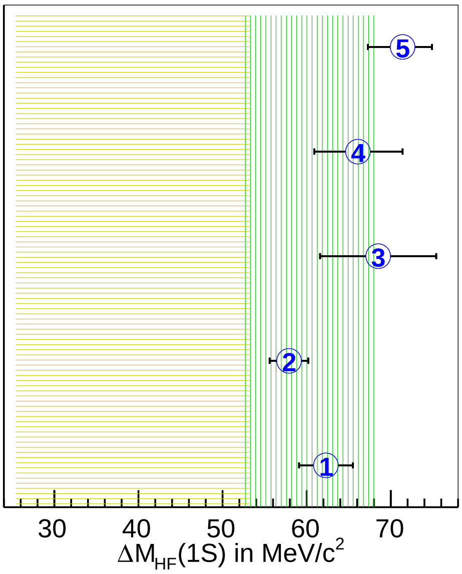

FIGURE 1.9: Comparison of experimental results and theoretical predictions for the hyperfine splitting for $1S$. The open numbered circles with error bars are experimental measurements: (5) by BaBar in $\Upsilon(3S) \to \gamma\eta_b(1S)$ [29], (4) by BaBar in $\Upsilon(2S) \to \gamma\eta_b(1S)$ [30], (3) by CLEO in $\Upsilon(3S) \to \gamma\eta_b(1S)$ [31], (2) by Belle in $h_b(nP) \to \eta_b(1S)$ $(n = 1, 2)$ [32], and (1) the world average value (excluding Belle measurement) [13]. Green vertical-line shaded area is the prediction from lattice QCD [33] while the yellow horizontal-line shaded area is the prediction from potential non-relativistic QCD [34].

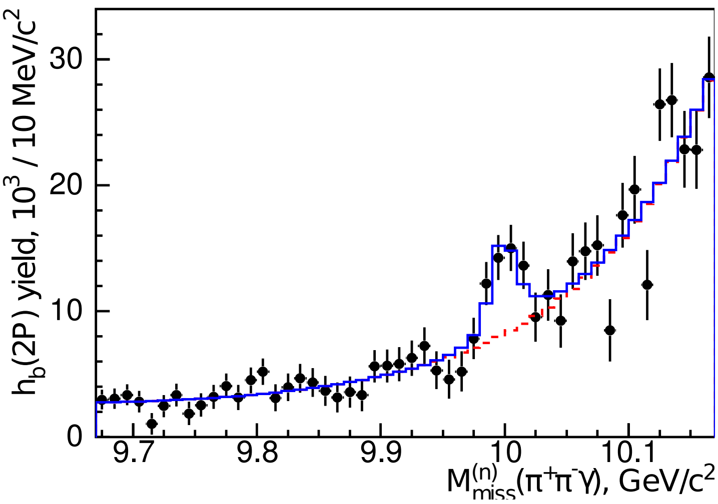

FIGURE 1.10: $h_b(2P)$ yield *vs.* $M^{(2)}_{miss}(\pi^+\pi^-\gamma)$ distribution in the $\eta_b(2S)$ region. Points with error bars are the data, the blue solid histogram is the result from a fit and the red dashed histogram is the background component of the fit. The plot is taken from Ref. [32].

where M[$(b\bar{b})$] is invariant mass formed from the final state hadrons. The enhancement seen near $\Delta M \sim 49$ MeV/c^2 is the claimed $X_{b\bar{b}}(9975)$ signal. Furthermore, this enhancement is assigned to the $\eta_b(2S)$, which corresponds to the hyperfine splitting, $\Delta M_{\mathrm{HF}}(2S) = 48.6 \pm 3.1$ MeV/c^2.

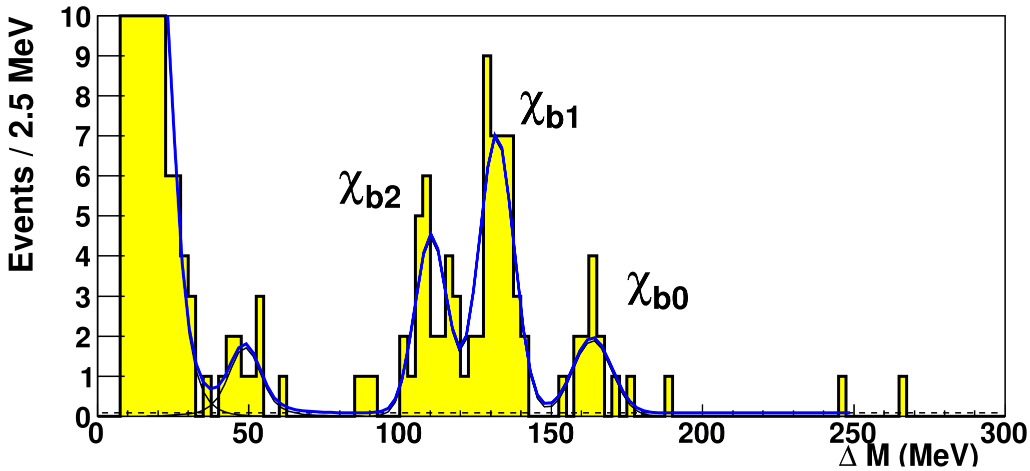

FIGURE 1.11: Distribution of ΔM in data recorded at the $\Upsilon(2S)$ resonance with the CLEO detector. The blue thick solid curve is the result from a fit while the black thin dashed curves are individual components of the fit. The three peaks from the right side are $\chi_{bJ}(1P)(J = 0, 1, 2)$, and the enhancement near $\Delta M \sim 49$ MeV/c^2 is $X_{b\bar{b}}(9975)$. The plot is taken from Ref. [35].

The claim of the $X_{b\bar{b}}(9975)$ state to be the $\eta_b(2S)$ is in contradiction with the Belle result, while the latter is in agreement with the lattice QCD, potential model and other related theoretical predictions summarized in Refs. [36, 37] and shown in Figure 1.12.

With 17 times more data recorded by the Belle detector at the $\Upsilon(2S)$ compared to CLEO and with similar charged hadron identification and photon reconstruction capabilities, we should be able to unambiguously confirm or refute the aforementioned observation of the $X_{b\bar{b}}(9975)$ signal. Our search for $X_{b\bar{b}}(9975)$ signal is presented in Chapter 3. The $X_{b\bar{b}}(9975)$ is reconstructed exclusively from the same 26 hadronic modes and in the same analysis we have also looked for the $\eta_b(1S)$ state.

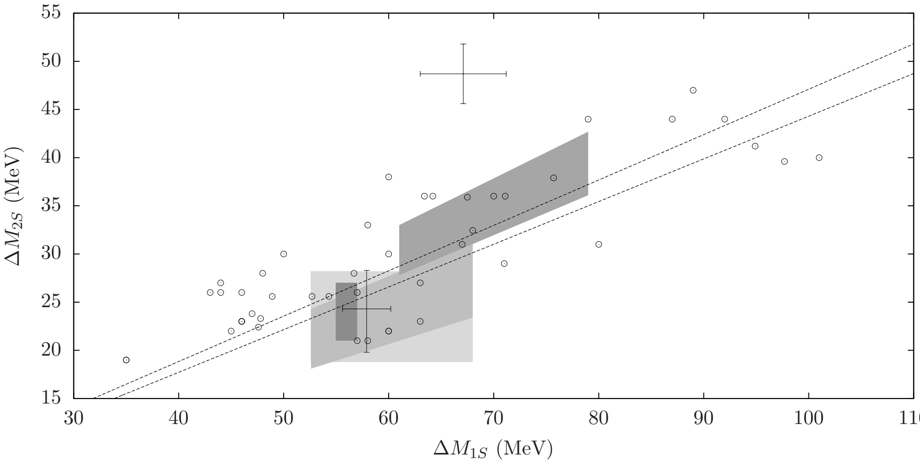

FIGURE 1.12: Theoretical prediction for $\Delta M_{HF}(1S)$ is along the horizontal axis and for $\Delta M_{HF}(2S)$ in the vertical axis of the plot. The predictions from lattice QCD are shown by the grey shaded area, model independent mass relation by dotted lines and potential models by the circles. The experimental measurements are shown by the error bars, Belle measurement is near $\Delta M_{HF}(2S) \sim 24\,\mathrm{MeV}/c^2$, closer to theory predictions, whereas the measurement in CLEO data is near $\Delta M_{HF}(2S) \sim 49\,\mathrm{MeV}/c^2$. The plot is taken from Ref. [36].

CHAPTER 2

Experimental Setup

The analyses mentioned in this thesis are performed with the datasets recorded by the Belle detector. The main goal of the Belle experiment was to observe the phenomenon of CP violation in the B-meson system. Therefore, the Belle detector [38, 39] was designed and optimised for this purpose, nevertheless it was a general purpose device. It was a large-solid-angle magnetic spectrometer located at the KEKB asymmetric-energy e^+e^- collider [40, 41]. An excellent performance of KEKB led to the world's highest instantaneous luminosity (2.11×10^{34} cm^{-2}s^{-1}) for a high-energy accelerator, enabling Belle to collect over 1000 fb^{-1} or, 1 ab^{-1} of e^+e^- collision data. In 2001, Belle (along with BaBar [42], a similar experiment located at Stanford, California) reported an observation of large CP violation asymmetries in B-meson decays as proposed by Kobayashi and Maskawa [43]. The importance of these results was recognized in the 2008 Physics Nobel Prize citation [44]. Now, KEKB is being upgraded to SuperKEKB to achieve 40-fold increase in luminosity. To cope with the such rise in luminosity Belle detector is also being upgraded to Belle II, for which the former was stopped recording data on 30 June 2010. The aim of the next generation Belle II experiment is to accumulate almost 50 times more data than Belle in a pursuit for physics beyond the standard model. The Belle II detector and our participation in its upgrade are described briefly in Appendix A.

In a bid to study properties of mainly B mesons, most of the Belle data are collected at the $\Upsilon(4S)$ resonance, because it predominantly ($> 96\%$) decays to a $B\overline{B}$ pair [13]. Belle has also recorded data samples near $\Upsilon(1S)$, $\Upsilon(2S)$, $\Upsilon(3S)$ and $\Upsilon(5S)$ resonance for studying other important topics, such as properties of B_s^0 mesons and charm physics, τ lepton, two-photon physics, and hadron spectroscopy.

This chapter introduces the KEB accelerator and then describes various components of the Belle detector as well as the datasets recorded by it. Towards the end, the particle identification techniques and analysis framework used within Belle are explained.

2.1 KEKB Accelerator

The KEKB accelerator is a two ring, asymmetric energy e^+e^- collider, which is designed to produce copious pairs of B and $\overline{B}$ mesons via the $\Upsilon(4S)$ decays. A high-energy (8 GeV) electron ring (HER) and a low-energy (3.5 GeV) positron ring (LER), each of about 3 km long, are installed side by side in a tunnel 11 m below the ground level. Figure 2.1 presents a schematic layout of the KEKB accelerator. The electron beam starts its journey from an electron gun, whereas positrons are produced by hitting electrons onto a positron production target, namely a water-cooled 14 mm tungsten plate.

After production, electrons and positrons are accelerated in a linear accelerator (Linac) and injected at full energies to each ring near the Fuji area shown in Figure 2.1. Designed current storage in the rings are 1.1 A for the HER and 2.6 A for the LER. The beams are distributed in about 5000 bunches with a bunch spacing of 0.59 m. The KEKB has one interaction point (IP) near the Tsukuba area (shown in Figure 2.1) around which the Belle detector is built. The typical beam size at the IP is 90 μm along the horizontal direction and 1.9 μm along the vertical direction. The two counter-rotating beams collide with a finite crossing angle of ± 11 mrad (0.63°) at the IP. The finite-angle collision scheme does not require any separation dipole magnets and thus significantly reduces beam-related background in the detector. Furthermore, with this scheme bunches are separated soon after the collision, which allows a minimal bunch spacing of 59 cm and filling all RF buckets with the beam. To cope up with the possible luminosity loss due to finite-angle beam crossing, specially designed crab-cavities are introduced near the IP.

A schematic diagram of the crab crossing concept is shown in Figure 2.2. In this scheme, electron and positron bunches are tilted near the IP by using a time-dependent strong transverse kick in the superconducting crab cavities to make

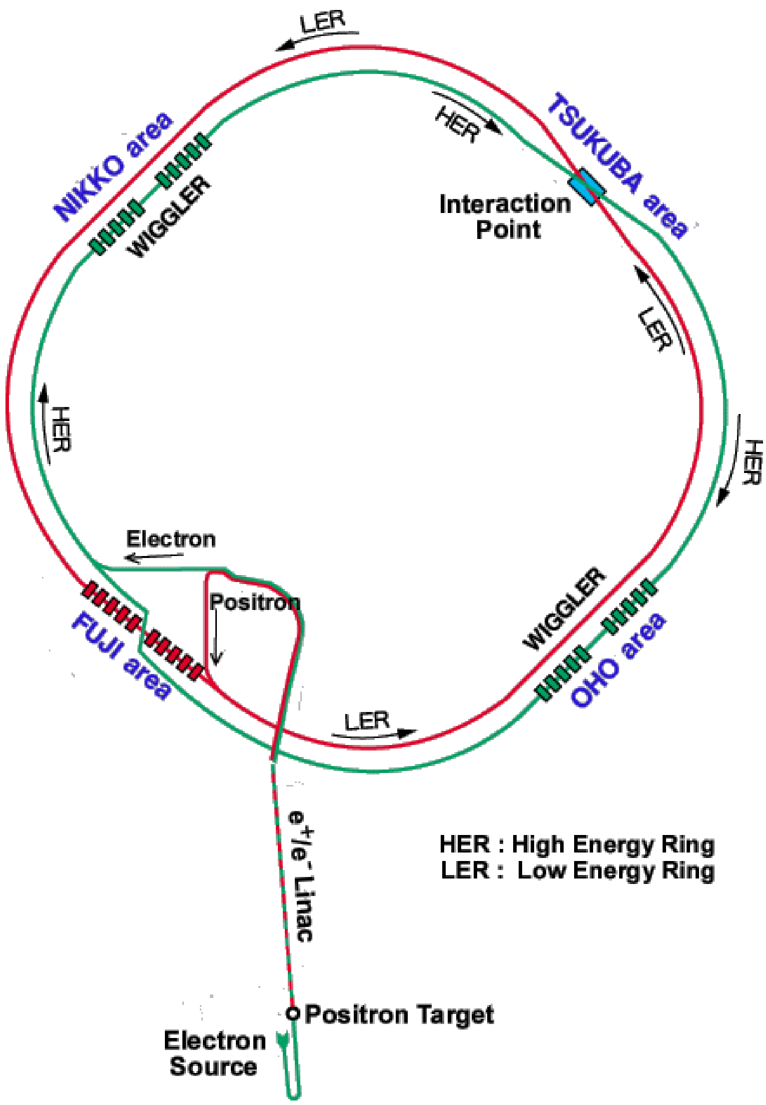

FIGURE 2.1: Schematic layout of the KEKB accelerator [45].

the collision head-on. After beam-crossing, the bunches are kicked back to their original orientation by other crab cavities.

Main parameters for the KEKB accelerator are listed in Table 2.1, which were designed to give an instantaneous luminosity of 1×10^{34} cm^{-2}s^{-1}. With an introduction of crab cavities the luminosity rose to 2.11×10^{34} cm^{-2}s^{-1}, breaking all records for the instantaneous luminosity for a high energy accelerator, which helped Belle to record more than 1 ab^{-1} of data.

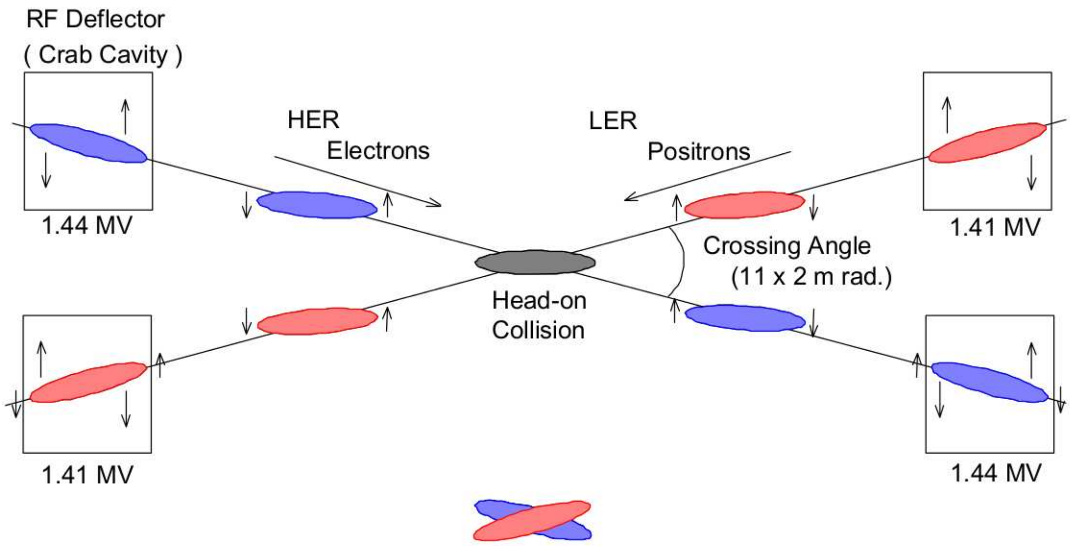

FIGURE 2.2: Beam rotation by crab cavities near the interaction region and non-crab crossing scheme (shown in bottom) [40].

2.2 Belle Detector

The Belle detector is composed of several sub-detectors assembled around a superconducting solenoid that provides a 1.5 T magnetic field. A silicon vertex detector (SVD) is placed closest to the interaction region in order to precisely locate the vertex of short-lived particles, in particular B mesons. Trajectories of charged particles in the magnetic field are recorded by a central drift chamber (CDC), which also provides information about specific ionization (dE/dx) of the particles. The identity of charged particles, especially pions and kaons is determined using this dE/dx information in conjunction with the Cerenkov light emitted in an array of silica aerogel Cerenkov counters (ACC) and the time-of-flight time measured in a barrel-like arrangement of plastic scintillation counters (TOF). The ACC and TOF are situated radially outside the CDC. An array of CsI(Tl) crystals is used as an electromagnetic calorimeter (ECL). All these sub-detectors are located inside the solenoid coil. The K_L^0 and muons (KLM) are identified using an array of resistive plate chambers interspersed in the iron yoke. Extreme forward calorimeter (EFC), an array of bismuth germanate crystals is located in the forward and rear end of the interaction region of Belle, which provides an active shield from beam background as well as helping to monitoring the luminosity. A three-dimensional schematic view of the Belle detector with its sub-detectors in different colors is

TABLE 2.1: Designed main parameters of KEKB [40].

Parameter	LER	HER	unit
Energy	3.5	8.0	GeV
Circumference	3.02		km
Luminosity	1×10^{34}		$\mathrm{cm^{-2}s^{-1}}$
Crossing angle	± 11		mrad
Beta function at IP ($\beta_x^\star/\beta_y^\star$)	0.33/0.01		m
Beam current	2.6	1.1	A
Natural bunch length (σ_z)	0.4		cm
Energy spread (σ_ε)	7.1×10^{-4}	6.7×10^{-4}	GeV
Bunch spacing (s_b)	0.59		m
Particle per bunch	3.3×10^{10}	1.4×10^{10}	
Emittance ($\varepsilon_x/\varepsilon_y$)	1.8×10^{-8}	3.6×10^{-10}	
RF voltage	6.5	12	MV
RF frequency	508.89		MHz
Harmonic number	5120		
Bending radius	16.3	104.5	m
Length of bending magnet	0.915	5.86	m

shown in Figure 2.3. All these sub-detectors are briefly described in the following subsections.

2.2.1 Interaction Region

The e^+ beam is aligned with the axis of the detector solenoid because lower-momentum charged particles would suffer more bending in the solenoid if they are off-axis. As there is a crossing angle (± 11 mrad) between the two beams, the e^- beam makes an angle of 22 mrad with the detector solenoid axis. The z-axis of the Belle detector is thus defined to be opposite of the e^+ beam while the y-axis is vertically upward, as shown in Figure 2.4.

Closer to the IP, the beam pipe is made up of beryllium with minimum thickness to minimize multiple Coulomb scattering, while its front and rear parts are in aluminum. In Figure 2.5, a schematic diagram of the beam pipe near the IP is shown. The central beryllium part is a double-wall cylinder that has an inner radius 20 mm and the thickness of both the walls is 0.5 mm. The gap between the walls is 2.5 mm, where helium gas is channeled for cooling. Total material

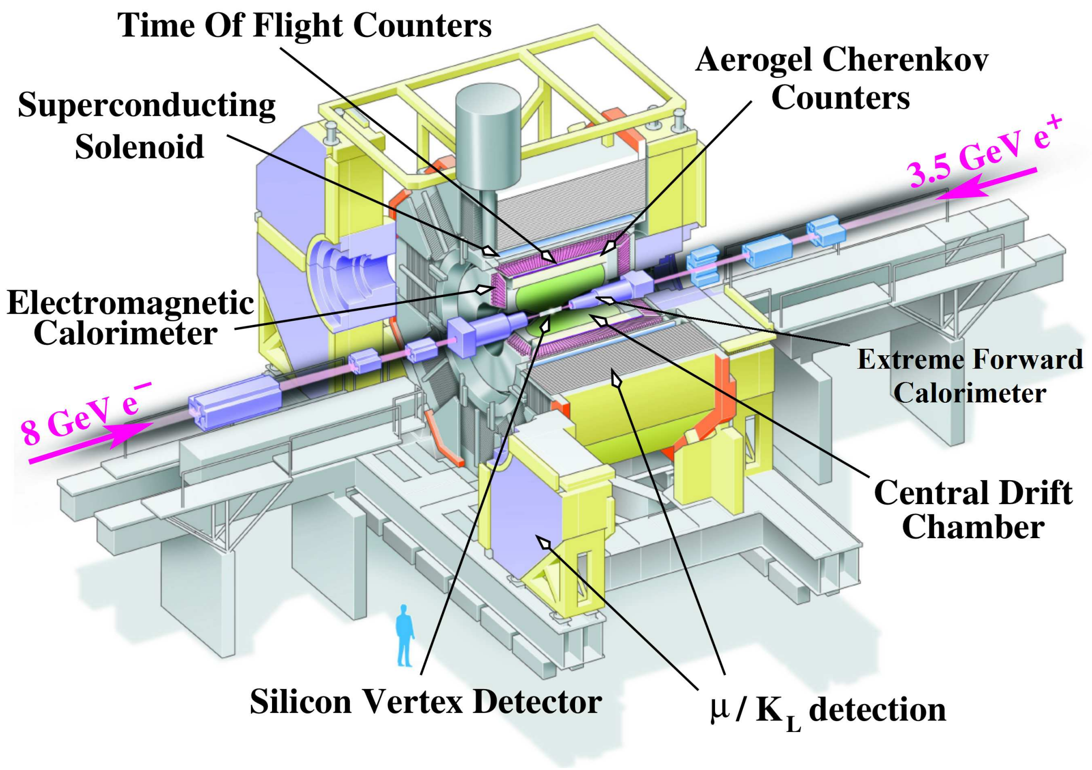

FIGURE 2.3: Schematic of the Belle detector. [38].

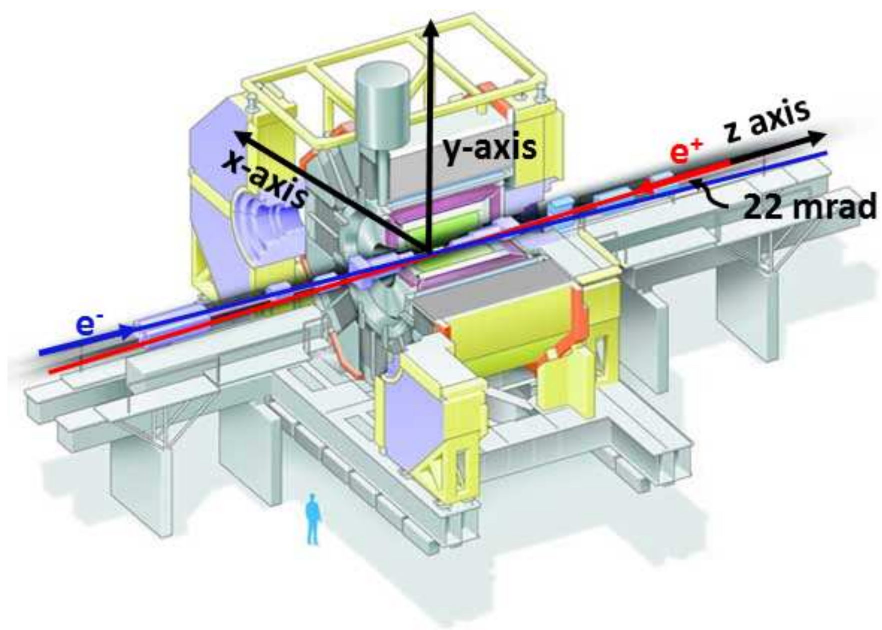

FIGURE 2.4: Definition of the coordinate system for Belle.

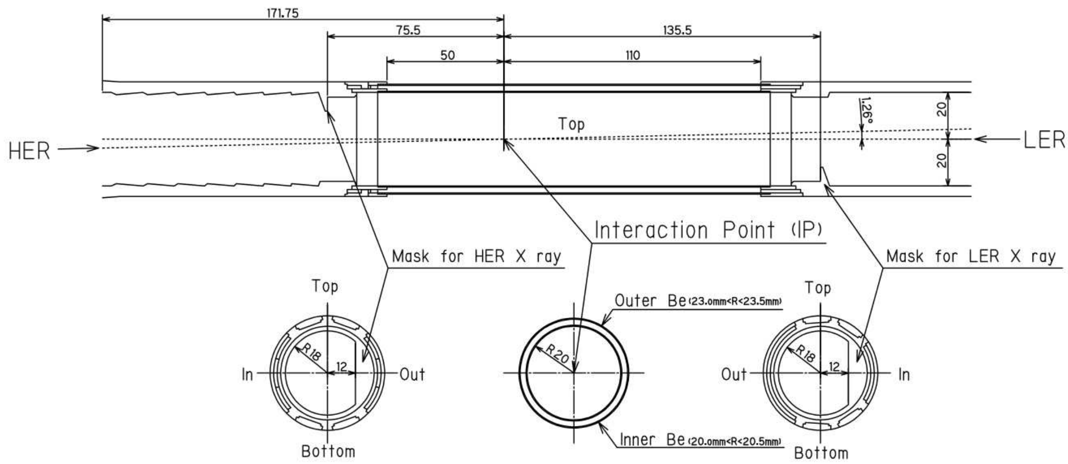

FIGURE 2.5: Layout of the interaction region [40].

thickness of the central part corresponds to 0.3% of a radiation length and has a length spread -4.6 cm$\leq z \leq 10.1$ cm. Outside the beryllium cylinder, a gold sheet of thickness $20\,\mu$m (0.6% of a radiation length) is attached to reduce the X-ray background.

2.2.2 Extreme Forward Calorimeter

The Extreme Forward Calorimeter (EFC), covers the angular ranges $[6.4°, 11.5°]$ and $[163.3°, 171.2°]$. It acts as a mask to protect the CDC from the beam background, and is used to monitor luminosity and as a tagging device for two-photon physics. Bismuth Germanate (BGO), $Bi_4Ge_3O_{12}$, is used in EFC as it is radiation hard and non-hygroscopic in nature, and has a short radiation length (1.12 cm) and suitable scintillating properties with decay time of about 300 ns. The BGO crystals are contained inside 1 mm thick steel, and the arrangement of the crystals in the forward and backward direction of the IP is shown in Figure 2.6.

The distance between the front surface of the detector and the IP is 60 cm and 43.5 cm, respectively, in the forward and backward direction. Due to limited space, forward and backward BGO crystals have 12 and 11 radiation lengths, respectively. Scintillation light is collected by two photo-diodes (Hamamatsu S5106) for each crystal, except for the two innermost layers, where one photo-diode is used. The energy resolution for the forward EFC is 7.3% at 8 GeV and that for the backward EFC is 5.8% at 3.5 GeV.

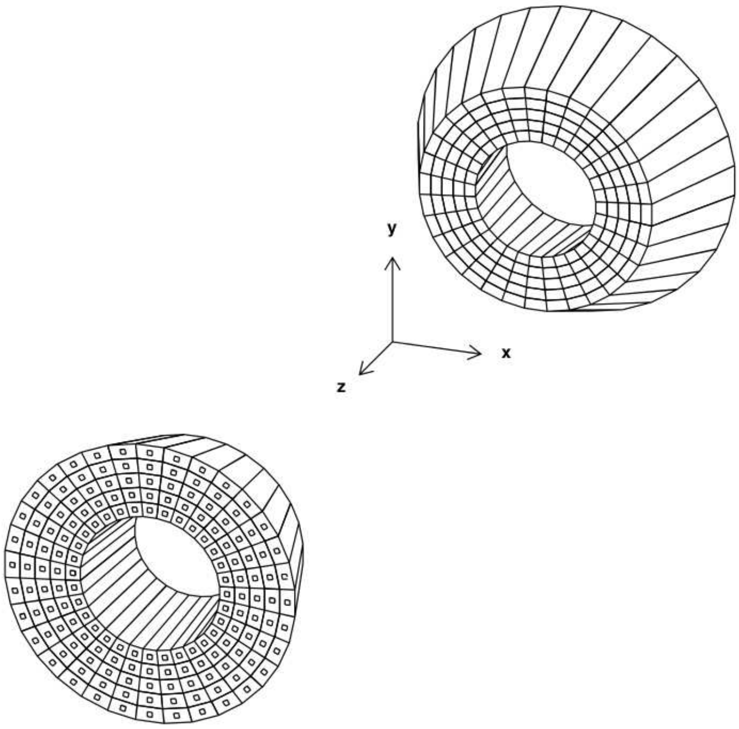

FIGURE 2.6: BGO crytal arrangement in the EFC [38].

2.2.3 Silicon Vertex Detector

The aim of the Silicon Vertex Detector (SVD) is to precisely measure the vertex position of B mesons and other short-lived particles like τ lepton and D mesons. In order to observe CP asymmetry in the B meson system, the difference in decay vertices of the two B mesons along the z axis needs to be determined with a precision of $\sim 100\,\mu$m. In addition to successfully accomplishing this task, the SVD also contributes towards the tracking of low-momentum charged particles.

The first version of the SVD (SVD1) had three layers of double-sided silicon microstrip detectors (DSSDs) that led to many excellent results including the discovery of CP violation in B meson decays in 2001. Despite its success, the SVD1 was mainly limited by a readout electronics with poor radiation tolerance. Therefore, it was later replaced by a new SVD (SVD2), which is more tolerant to radiation (successfully tested for a radiation hardness up to 20 Mrad) and has a better trigger capability to cope up with the higher luminosity phase of KEKB [46].

The SVD2 has a four-layer structure with the innermost one being 20 mm away from the beam pipe, and each layer consists of an assembly of DSSDs as shown in Figure 2.7. The SVD2 has a polar-angle coverage: $17° < \theta < 150°$. Its main

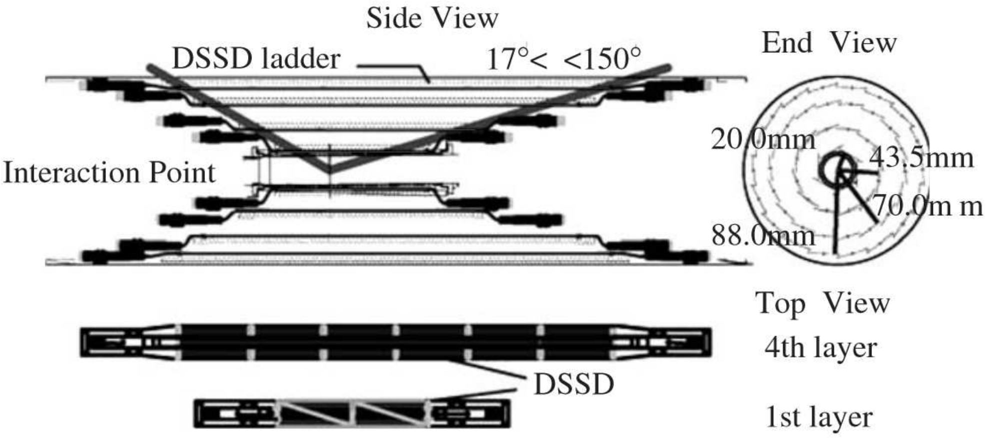

FIGURE 2.7: Schematic layout of the SVD2 [46].

parameters are listed in Table 2.2, where the strip pitch is the separation between two strips. The measured hit resolution in the transverse r-ϕ plane and along the z-axis are 12 μm and 19 μm, respectively [47].

TABLE 2.2: Main parameters of the SVD [46, 47]

.

Parameter	Layers 1–3		Layer 4	
Size (mm^3)	$79.2 \times 28.4 \times 0.3$		$76.4 \times 34.9 \times 0.3$	
Side	n(r-ϕ)	p(z)	n(r-ϕ)	p(z)
Strip pitch (μm)	50	75	65	73
Strip width (μm)	10	50	12	55
Number of strips	512	1024	512	1024

2.2.4 Central Drift Chamber

The Central Drift Chamber (CDC) is designed to: a) precisely determine three-dimensional trajectories (tracking) of charged particles in the magnetic field, b) measure the momentum and specific ionization (dE/dx), and c) provide fast-track information for discriminating interesting physics events from the beam-induced background at the trigger level [48, 49]. The majority of the particles (mostly coming from a B meson decay) have a momentum less than 1 GeV/c. Thus to minimise multiple coulomb scattering and improve the momentum resolution, a low-Z gas – a mixture of 50% helium and 50% ethane – is used. This gas mixture has a long radiation length of 640 m, and a drift velocity that saturates at about 4 cm/μs for a 2 kV/cm electric field.

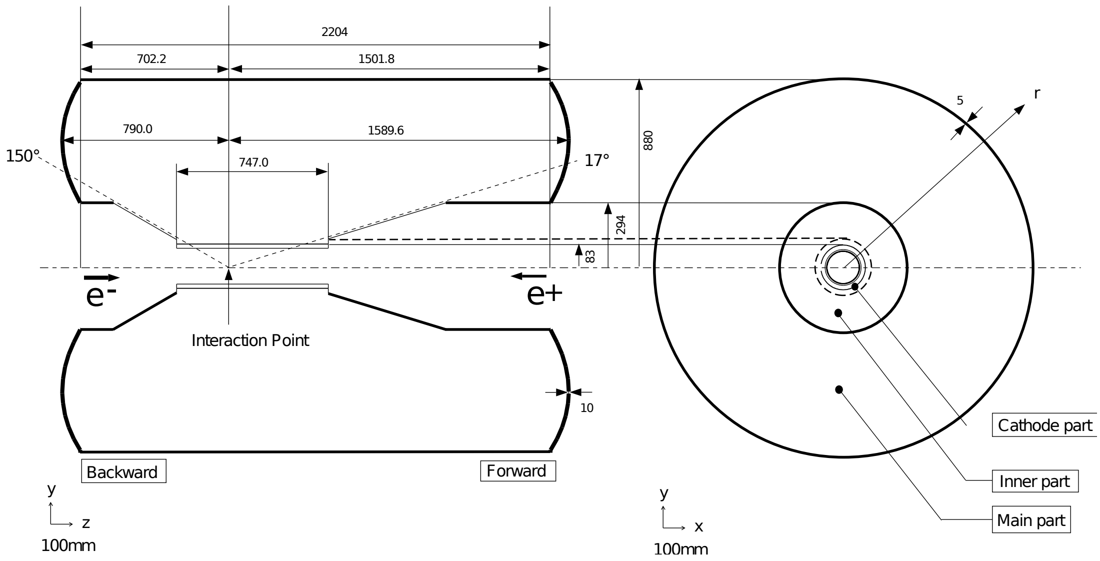

FIGURE 2.8: A sketch of the CDC structure (length in mm) [38].

The Belle CDC is asymmetric along the z-axis and has an angular coverage $17° \leq \theta \leq 150°$. The drift cylinder length is about 2.4 m with an inner radius 83 mm and an outer radius 874 mm; its design is shown in Figure 2.8. The CDC is basically a cylindrical wire drift chamber composed of 50 layers of anode wires. Each layer contains between three to six axial or small-angle-stereo layers, the innermost part having three cathode-strip layers. The drift chamber has in total 8400 drift cells, each cell having one positively biased sense wire surrounded by eight field wires, as shown in Figure 2.9. The sense wires are gold-plated tungsten wires of diameter 30 μm, while the field wires are made from aluminium of diameter 126 μm in order to keep the electric field at the wire surface below 20 kV/cm to avoid potential radiation damage. For the innermost three layers, a cathode image readout system is used in combination with small-angle-stereo anode wires for a better z-position measurement and thus an improved CDC-to-SVD track matching. Momentum resolution (σ_{p_t}/p_t) for a charged track as a function of its transverse momentum (p_t) can be given as [39],

$$\sigma_{p_t}/p_t = 0.0019\ p_t[\mathrm{GeV/c}] \oplus 0.0030/\beta, \tag{2.1}$$

where $\beta = v/c$, v is velocity of the charged particle and c is the velocity of light.

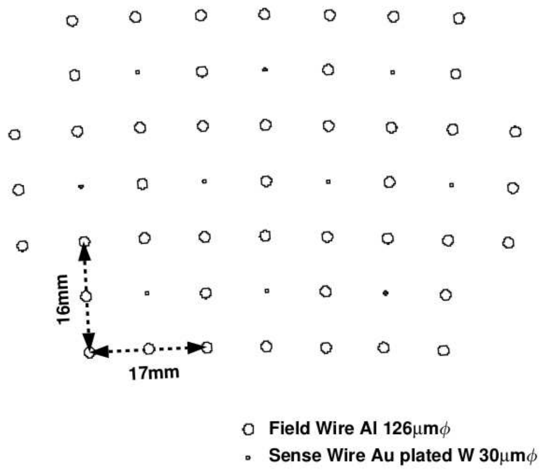

FIGURE 2.9: Cell structure of the CDC.

2.2.5 Aerogel Cerenkov Counters

An array of silica aerogel Cerenkov counters (ACC) provides charged particle identification (PID), especially for pions and kaons. It extends the momentum coverage of the Belle PID system up to 3.5 GeV/c. It is a threshold type Cerenkov counter, where the Cerenkov radiation is emitted for charged pions (and charged particles less massive than pions), for that silica aerogels with a refractive index 1.01 to 1.03 are used [50].

The ACC counters are arranged in the central cylindrical (barrel) and forward endcap part of the Belle detector. The barrel part consists of in total 960 modules, segmented in 60 counters in the ϕ circle with a range of refractive index between 1.010 to 1.028, depending on the polar angle. The forward endcap is comprised of 228 counters in a five concentric arrangement having an refractive index 1.03. The refractive index of aerogel of barrel part depends on the polar angle. For the forward endcap part, refractive index is tuned for flavor tagging. Since there is no TOF counter in the endcap, ACC has to cover a lower momentum region. The configuration of the counter modules is shown in Figure 2.10.

The counter module in the barrel region contains five aerogel tiles inside an aluminium box, to which one or two fine-mesh photomultiplier tubes (FM-PMTs) are attached for the Cerenkov photon detection. In the forward endcap part, five areogel tiles are placed inside a carbon-fiber reinforced polymer (CFRP) box and

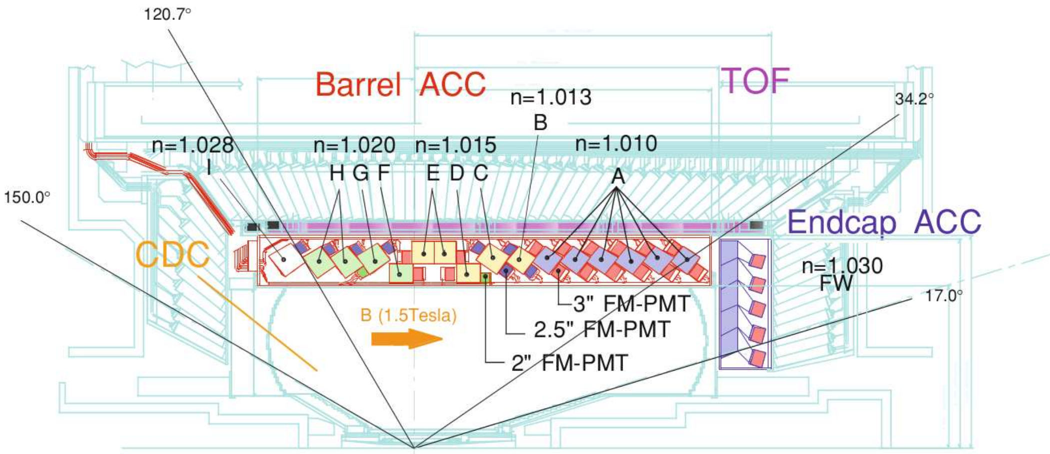

FIGURE 2.10: Configuration of the ACCs in the Belle Detector [38].

the FM-PMTs are attached to it through air light guide. For a better light collection, the inner surface of the module box is lined with diffusive reflector sheets (Goretex). A schematic of the counter modules is shown in Figure 2.11.

2.2.6 Time-of-flight System

The time-of-flight (TOF) system is useful in identifying charged particles with a momentum less than 1.2 GeV/c. For a 1.2 m flight path, the TOF should have a time resolution of 100 ps to distinguish between pions and kaons. To achieve this goal the Belle TOF system has adopted following design strategies: a) fast scintillator with an attenuation length longer than 2.5 m, b) no light guides to minimize time dispersion of scintillation photons, and c) PMTs with larger photocathodes to maximise light collection [51].

Each TOF module consists of two counters with FM-PMTs as readout mounted directly at both the ends, and one thin trigger scintillation counter with the readout at the rear end only. Design of a TOF module is shown in Figure 2.12. The acceptance of TOF is $33° < \theta < 121°$, while the minimum transverse momentum to reach the TOF system in the 1.5 T magnetic field is 0.28 GeV/c.

2.2.7 Electromagnetic Calorimeter

To reconstruct neutral particles such as photons, π^0 and η mesons (decaying to two photons) the electromagnetic calorimeter (ECL) plays a crucial role. It is also used

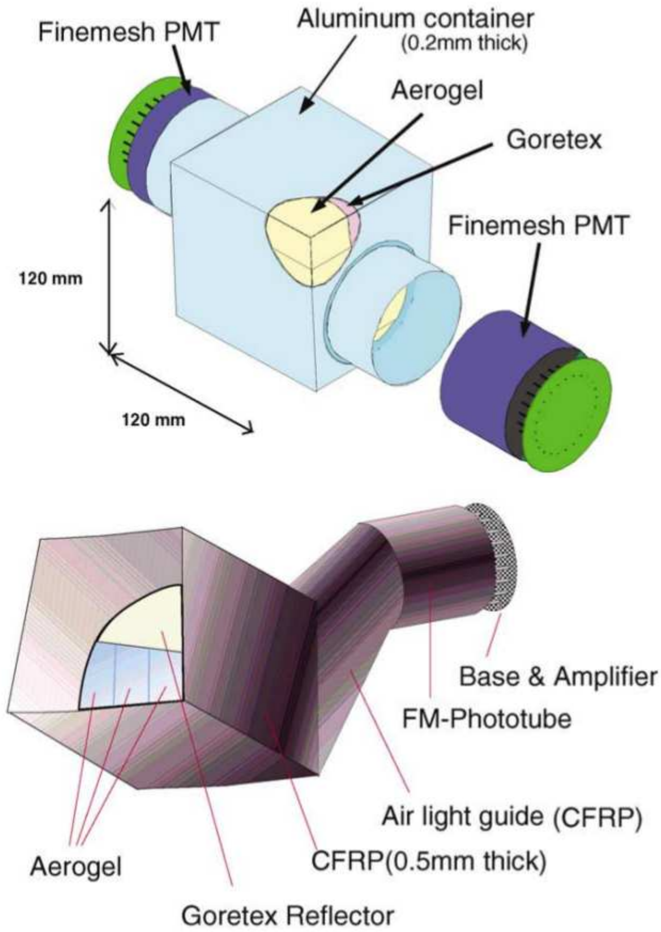

FIGURE 2.11: A schematic drawing of ACC modules: (top) modules in the barrel region, and (bottom) modules in the forward endcap region [38].

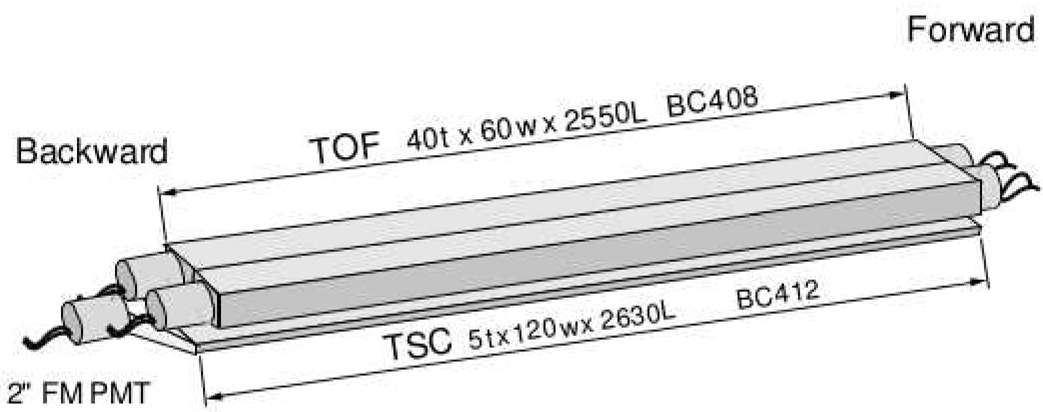

FIGURE 2.12: Design of a TOF module [52].

in the electron identification. Most of the photons in Belle are the end products of cascade decays and have a relatively low energy (less than 500 MeV). Processes like $B \to \pi^0\pi^0$ or $B \to K^{\star}\gamma$ have photon energies up to 4 GeV. Also, for the luminosity measurement and detector calibration purpose the Bhabha scattering and $e^+e^- \to \gamma\gamma$ processes are used, in which the photon energy ranges to 8 GeV. The Belle ECL is thus designed to cover a wide range of photon energy starting from 20 MeV to 8 GeV [53].

The ECL is a segmented array of CsI(Tl) crystals and size of each crystal is determined by the condition that about 80% of total energy deposited by a photon injected at the center of the crystal is contained in that crystal. The segmented ECL is needed mainly to detect high momentum π^0 from nearby photon clusters. As, these crystals are installed inside a 1.5 T magnetic field, silicon photodiodes are used as the readout device. Overall structure of the ECL is shown in Figure 2.13.

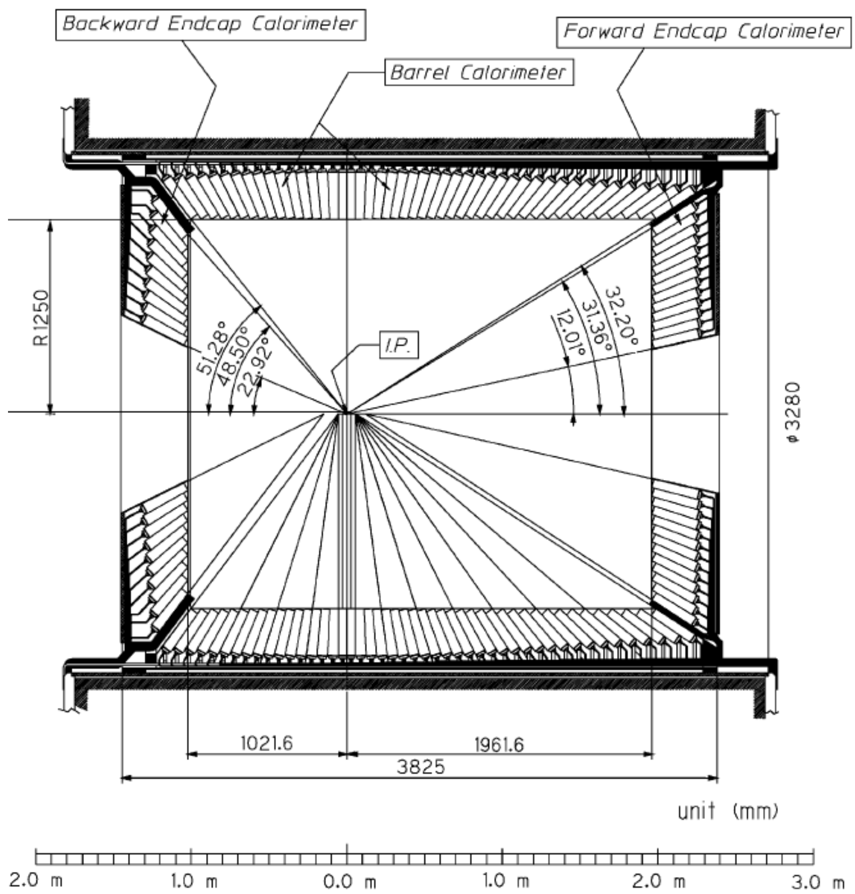

FIGURE 2.13: Configuration of the Belle ECL [53].

The ECL covers in the polar angle $12^\circ < \theta < 155^\circ$, and is made from in total 8736 CsI(Tl) crystals of which 6624 are in the barrel and 1152 (960) are in the forward (backward) endcap region. Each CsI(Tl) crystal is 30 cm long that corresponds to 16.2 radiation lengths, chosen to avoid any degradation of energy resolution at higher energy due to fluctuations in shower leakages at the back-end of the counters. Crystals in the barrel region have a front-face area 5.5×5.5 cm^2 and back-end area 6.5×6.5 cm^2. The overall energy resolution of the ECL can be written as [54],

$$\frac{\sigma_E}{E} = \frac{0.0066\%}{E} \oplus \frac{1.53\%}{E^{1/4}} \oplus 1.18\%, \tag{2.2}$$

E is in GeV. The first term corresponds to the electronic noise, the second term originate from the stochastic fluctuations in the showering process and third term comes from the shower leakage in the crystal.

2.2.8 Superconducting Solenoid

A magnetic field of 1.5 T inside the Belle detector is produced by a superconducting solenoid, made from a niobium-titanium alloy in a copper matrix (NbTi/Cu) and stabilized by aluminium. The cryostat cylinder has an outer and inner radius 2.0 m and 1.7 m, respectively, and is 4.4 m long. The stored energy in the superconducting coil is about 35 MJ and has a nominal current 4400 A. The iron support structure of Belle serves as the return yolk for the magnetic flux and also as an absorber for KLM (see the next subsection). An schematic of the magnet and a cross-sectional view of the coil is shown in Figure 2.14.

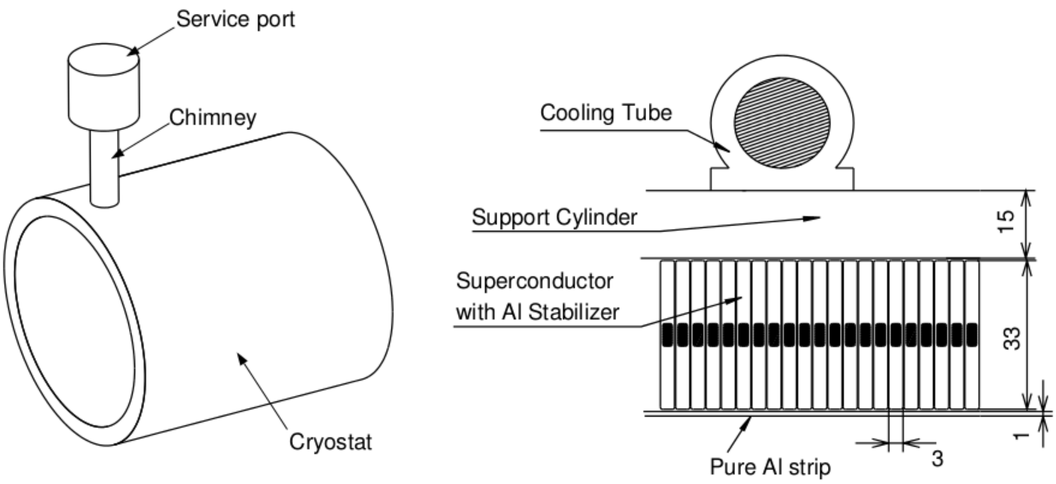

FIGURE 2.14: (left)An schematic of the magnet and (right) a cross-sectional view of the coil [38].

2.2.9 K_L and Muon Detector

The K_L and Muon Detector (KLM) consists of alternating layers of 4.7-cm thick iron plates and super-layers of glass resistive plate chambers (RPCs). Cross section of the KLM in the barrel region is octagonal in shape and has 15 RPC super-layers and 14 iron layers, while in both the endcaps there are 14 RPC super-layers. The detector is designed to identify K_Ls and muons, and provides a total of 3.9 nuclear interaction length in addition to 0.8 interaction length of material in the ECL for K_Ls to convert in the shower of ionizing particles. Then, the RPC layers allow to differentiate between charged hadrons and muons, as muons travel much farther with a small deflection. The KLM covers an angular range from 20° to 155°. RPCs, arranged in the super-layer of the KLM, have two parallel-plate glass electrodes with bulk resistivity $\geq 10^{10}$ Ω cm, and are operated at the atmospheric pressure.

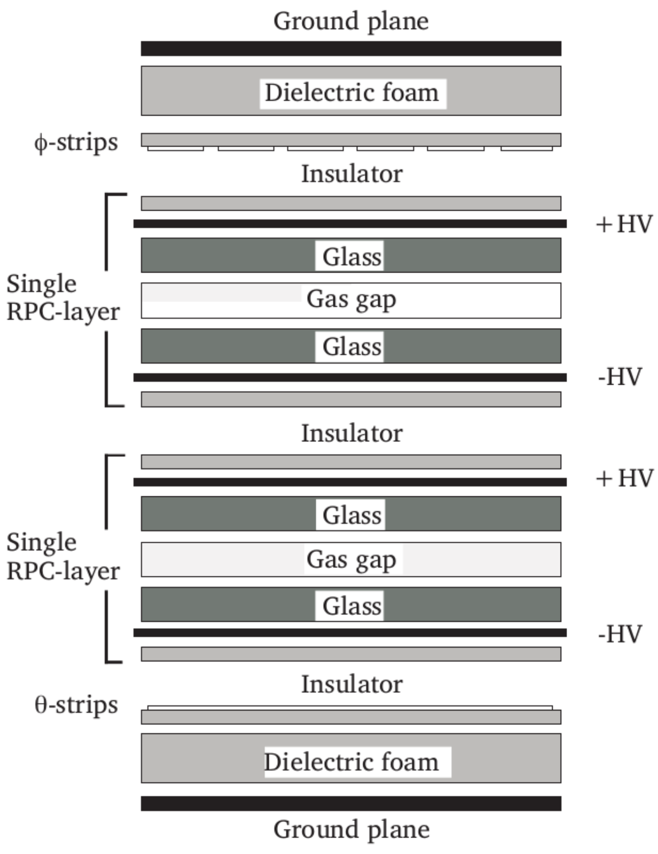

FIGURE 2.15: Schematic of a super-layer of the KLM [38].

A cross-sectional view of a super-layer is shown in Figure 2.15, in which two RPCs are placed in between the orthogonal pickup strips, one along θ (bottom pickup strip) and other along ϕ (top pickup strip).

2.2.10 Trigger and DAQ

The trigger is an online system that quickly discards uninteresting events while retaining potentially interesting physics events for further analysis, and allows the data acquisition (DAQ) system to record the latter. The cross sections and expected trigger rates of various interesting physics processes with the nominal luminosity 1.0×10^{34} cm^{-2}s^{-1} at the $\Upsilon(4S)$ resonance are listed in Table 2.3.

.
TABLE 2.3: Cross section and trigger rates of various interesting physics processes with $\mathcal{L} = 10^{34}$ cm^{-2}s^{-1} [55]

Physics process	Cross section (nb)	Rate (Hz)
$\Upsilon(4S) \to B\overline{B}$	1.15	11.5
$e^+e^- \to q\overline{q}$ $(q = u, d, s, c)$	2.8	28
$e^+e^- \to \mu^+\mu^-/\tau^+\tau^-$	1.6	16
Bhabha $(e^+e^- \to e^+e^-)$ $(\theta_{\text{lab}} \geq 17^\circ)$	44	4.4[a]
$e^+e^- \to \gamma\gamma$ $(\theta_{\text{lab}} \geq 17^\circ)$	2.4	0.24[a]
Two-photon events $(\theta_{\text{lab}} \geq 17^\circ, p_T \geq 0.1\,\text{GeV}/c)$	$\sim$15	$\sim$35[b]
Total	$\sim$67	$\sim$96

[a] pre-scaled by a factor 0.01
[b] with restricted condition $p_t \geq 0.3\,\text{GeV}/c$

The Bhabha and $e^+e^- \to \gamma\gamma$ events are useful in monitoring the luminosity and calibrating detector. These events are prescaled due to their large cross sections. Two-photon events are suppressed as they have a large cross section and topologically resemble with the beam background. In total, physics events have trigger rate of about 100 Hz. Beam related backgrounds mainly coming from the spent electron and positrons, have rate $\sim$ 100 Hz, estimated from simulation studies. Hence for the luminosity 1.0×10^{34} cm^{-2}s^{-1}, a total trigger rate of $\sim$ 200 Hz is expected. However, the trigger system is required to be built robust against any expected high background rate, kept within the tolerance of DAQ (max. 500 Hz) and efficient for the interesting physics events.

The Belle trigger system has two parts: (1) trigger system from individual subdetectors, and (2) central trigger system. It is described in detail in Refs. [38, 55–57].

2.3 Particle Identification in Belle

Particle identification (PID) plays an important role in tagging the B and D mesons. The PID is also needed to reconstruct exclusive decay modes of other hadrons. Energy loss due to ionisation (dE/dx) by a charged particle inside the CDC volume can be used to identify it, as shown in Figure 2.16.

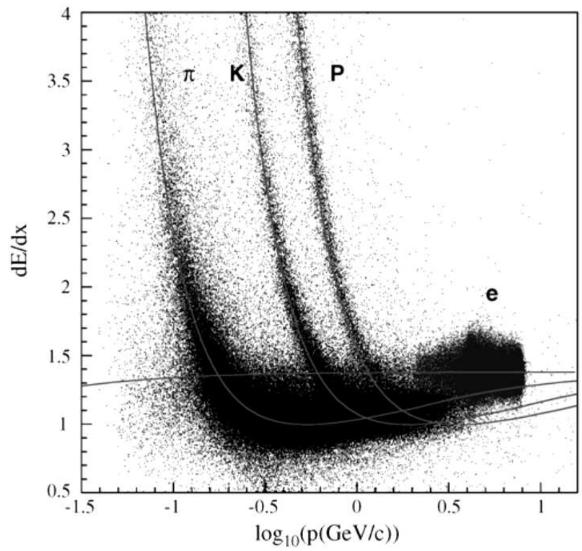

FIGURE 2.16: dE/dx *vs* momentum (in the log scale) for electron, pion, kaon and proton [58].

From the dE/dx information from the CDC, a χ_i^2 for each charged particle is calculated as

$$\chi_i^2 = \left(\frac{(dE/dx)_{meas.} - (dE/dx)_i}{\sigma_{(dE/dx)}}\right)^2, \tag{2.3}$$

where $(dE/dx)_{meas.}$ is the measured energy loss, $(dE/dx)_i$ is the expected energy loss for the i-th type of particle ($i = e, \mu, \pi, K$ or p) type, and $\sigma_{(dE/dx)}$ is the resolution of the measured dE/dx. Then a likelihood is calculated, assuming a Gaussian distribution, as

$$P_i^{\mathrm{CDC}} = \frac{e^{-\chi_i^2/2}}{\sqrt{2\pi}\sigma_{(dE/dx)}}. \tag{2.4}$$

Less than 100 ps resolution of the TOF system allows a 3 standard deviation (σ) separation between charged pions and kaons.The mass distribution in Figure 2.17, shows clearly separated pion, kaon and proton peaks, and is obtained

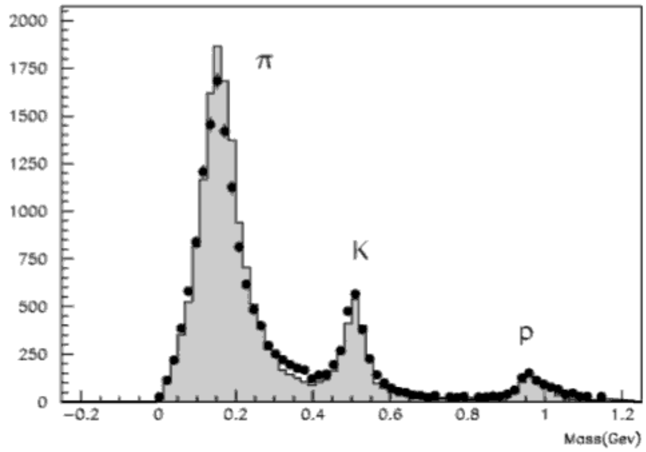

FIGURE 2.17: Mass distribution from the TOF measurement [51].

from Eq. (2.5). Also, in the mass distribution plot in the data points agree well with MC predictions, represented by the gray shaded histogram.

$$\text{mass}^2 = \left(\frac{1}{\beta^2} - 1\right) p^2 = \left[\left(\frac{cT_{obs}^{corr.}}{L_{path}}\right) - 1\right] p^2 \tag{2.5}$$

where p and L_{path} is the momentum and path length of the particle. respectively, obtained from the CDC assuming a muon mass, and $T_{obs}^{corr.}$ is the corrected observed time as defined in Ref. [51]. A χ_i^2 for TOF is constructed from the expected and observed time difference for PMT readout at each end, $\Delta_i^k = t_{meas.}^k - t_i^k$, where k is 0 or 1 indicating the two readouts of the PMT. Then, the χ_i^2 and likelihood are defined in Eqs. (2.6) and (2.7) respectively,

$$\chi_i^2 = \Delta_i^T E^{-1} \Delta_i \tag{2.6}$$

$$P_i^{\text{TOF}} = \frac{e^{-\chi_i^2/2}}{\prod_{l=1}^{ndf} \sqrt{2\pi}\sigma_{\text{TOF}}} \tag{2.7}$$

where Δ_i are elements of the vector Δ_i^k, E is the 2×2 error matrix, and σ_{TOF} is the TOF resolution. The particle likelihood for the ACC, P_i^{ACC}, is obtained from the number of photoelectron distribution for each particle species expected from Monte Carlo simulations.

The three individual likelihoods obtained from the CDC, TOF and ACC are combined to get a total likelihood for each particle type,

$$P_i = P_i^{\text{ACC}} \times P_i^{\text{TOF}} \times P_i^{\text{CDC}}. \tag{2.8}$$

In order to distinguish between the two particle species i and j, the following likelihood ratio is then used,

$$\mathcal{L}_{i/j} = \frac{P_i}{P_i + P_j}. \tag{2.9}$$

In case information from one of the sub-detectors is not available for the examined track, a value of 0.5 is assigned for the corresponding sub-detector likelihood for any particle species [59]. This can be noticed as a peak at 0.5 in the $\mathcal{L}_{i/j}$ distribution, shown in Figures 3.4, 3.5, 4.2, and 4.3 .

An electron is identified by matching a charged track in the CDC extrapolated to the cluster centroid in the ECL and subsequently using the energy to momentum ratio, electromagnetic shower shape, dE/dx and Cerenkov light yield in the ACC [60]. Muons are identified using information solely from the KLM subdetector.

2.4 Data recorded by Belle

As already mentioned, Belle has recorded e^+e^- collision data at various $\Upsilon(nS)$ resonances, with most of which are at the $\Upsilon(4S)$. The e^- and e^+ beam energies at these resonances are listed in Table 2.4. Energy in the center of mass (CM) frame ($\mathrm{E_{CM}}$) can be calculated as,

$$\mathrm{E_{CM}} = \sqrt{2(1+\cos\theta)\mathrm{E_{HER}}\mathrm{E_{LER}}} \approx 2\sqrt{\mathrm{E_{HER}}\mathrm{E_{LER}}} \tag{2.10}$$

where θ is the beam crossing angle (22 mrad), $\mathrm{E_{HER}}$ and $\mathrm{E_{LER}}$ are energy of the electron and positron beams respectively in the laboratory frame. The asymmetric energy of two beams provides a boost to the CM system, mainly aimed at measuring the time-dependent CP asymmetry in decays of B mesons coming from the $\Upsilon(4S)$ resonance. The detector is designed to be asymmetric owing to the boosted CM frame, and hence the boost vector is kept constant while running at different resonances. This is achieved by tuning the energy of both the beams, as shown in Figure 2.18.

TABLE 2.4: Data recorded at various $\Upsilon(nS)$ resonances [39].

Resonance	HER (GeV)	LER (GeV)	E_{CM} (GeV)	On-peak (Off-peak) luminosity in fb^{-1}
$\Upsilon(1S)$	7.15	3.13	9.46	5.7 (1.8)
$\Upsilon(2S)$	7.58	3.31	10.02	24.7 (1.7)
$\Upsilon(3S)$	7.83	3.42	10.35	2.9 (0.25)
$\Upsilon(4S)$	8.00	3.50	10.58	711.0 (89.4)
$\Upsilon(5S)$	8.22	3.59	10.86	121.4 (1.7)

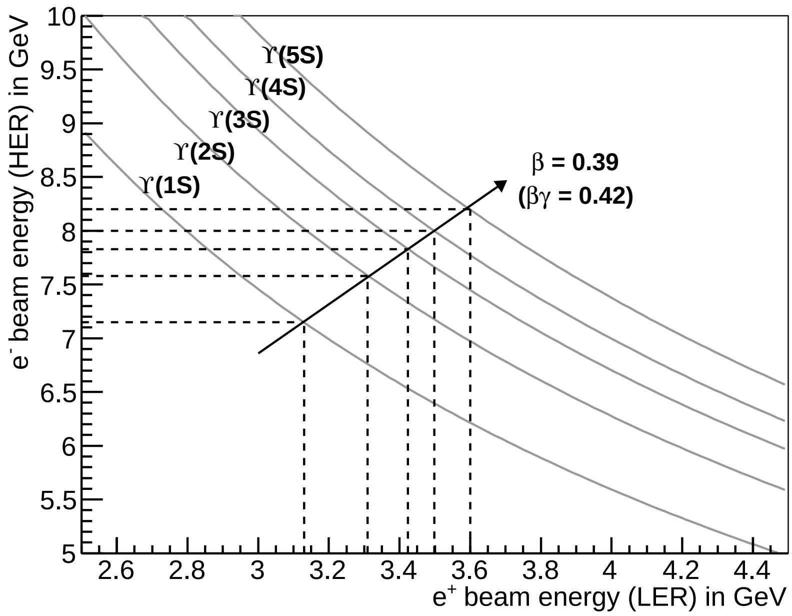

FIGURE 2.18: Variation of E_{HER} and E_{LER} at different resonances keeping the boost constant.

The datasets recorded by Belle at $\Upsilon(1S)$, $\Upsilon(2S)$ and $\Upsilon(4S)$ resonances are the world's largest samples, whereas its dataset at the $\Upsilon(5S)$ resonance is a unique sample collected in e^+e^- collisions. Figure 2.19 compares the number of $\Upsilon(nS)(n \neq 4)$ resonances recorded by the Belle, BaBar and CLEO experiments.[1]

Studies presented in this thesis are mostly based on the data collected at the $\Upsilon(2S)$ resonance. A sample of 24.7 fb^{-1} at $\Upsilon(2S)$ corresponds to $(157.8 \pm 3.6) \times 10^6$ $\Upsilon(2S)$ decays [61], which is 17 and 1.6 times larger than the data collected with the CLEO and BaBar detector, respectively.

[1]The comparison is done for $\Upsilon(nS)(n \neq 4)$ resonances because these datasets are more important in the context of hadron spectroscopy.

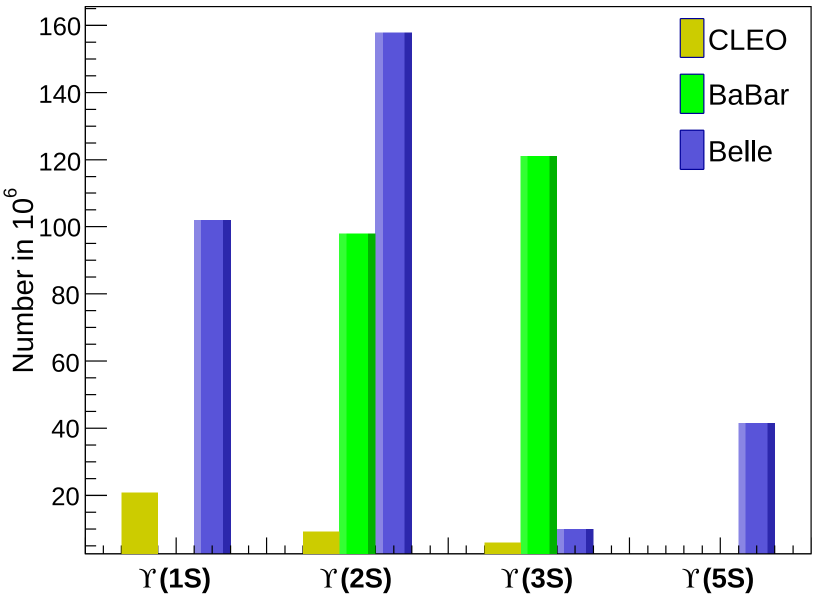

FIGURE 2.19: A Comparison of datasets collected at different $\Upsilon(nS)(n \neq 4)$ resonances between Belle, BaBar and CLEO experiments.

2.5 Analysis Framework

The Belle DAQ system is segmented into 7 subsytem running in parallel, each handling data from a subdetector. The data from each subdetector components are combined into a single event record by an event builder, which converts the parallel data stream from subdetectors to an 'event-by-event' data river. Events are stored onto data summary tapes (DSTs) by running reconstruction algorithms on the raw data. At this stage, only interesting physics events are accepted by a level-4 software filter (L4 trigger) [38], to be stored in DSTs. It also converts the raw data format of detector component outputs into physics objects, such as helix parameters, particle identification information, 4-vectors of momentum and position. In a physics analysis, all the information available in the DSTs are not needed. Hence, for this purpose a minimal set of parameters describing an event is stored in a mini-DST (MDST) format. The MDSTs are compact but sufficient enough to perform a physics analysis. A typical hadronic event in the MDST format has the size of about 40 KB.

The event processing framework of Belle is called BASF (Belle AnalysiS Framework), in which user's reconstruction and analysis codes are taken as modules and linked dynamically at the run time. A module is usually written as an object of a C++ class, though modules written in Fortran and C can also be linked using wrapper funtions. PANTHER [62], an event and I/O management package, is developed by the Belle Collaboration for the data transfer between the modules.

2.6 Monte Carlo Simulations

For a better understanding the nature of signal events and in order to select them from a sea of backgrounds Monte Carlo (MC) simulations are produced. MC events are also very useful in performing blind analyses in which signal region is kept hidden to reduce experimenter's bias. At Belle, the MC production can be divided in two steps. First physical processes involved in a decay are generated using the `EvtGen` [63] package. `EvtGen` is an event generation package that implements many detailed decay models, well suited for B physics. It has an interface to `JetSet` [64] and PYTHIA [65] for generation of continuum and to model the hadronization of quarks. Then, the detector effects to an already generated event is included by passing it through a GEANT [66] based MC simulator, which simulates the interactions between the particles and detector material. Detector parameters are updated in regular intervals during each experimental run to mimic the run-dependent conditions. Beam-background events, obtained from the real random-triggered data, are overlaid on the simulated MC events. Then, the simulated events are saved in MDST format and analysed in a similar way as the real data. MC samples generated for our studies are discussed in Chapters 3.1 and 4.1.

CHAPTER 3

Search for $X_{b\bar{b}}(9975)$

The $X_{b\bar{b}}(9975)$ state is an enhancement observed, corresponding to a mass (9974.6 $\pm$ 2.3 $\pm$ 2.1) MeV/c^2, in the data recorded with the CLEO detector at the $\Upsilon(2S)$ resonance. The $X_{b\bar{b}}(9975)$ is reconstructed from the sum of 26 Hadrian modes in the radiative $\Upsilon(2S)$ decays and attributed to the $\eta_b(2S)$ state in Ref. [35]. It has already been described in Chapter 1 that this claim is inconsistent with the observation of the $\eta_b(2S)$ by the Belle Collaboration at mass $(9999.0 \pm 3.5^{+2.8}_{-1.9})$ MeV/c^2 [32] as well as with the theoretical predictions.

Belle can unambiguously confirm or rule out this $X_{b\bar{b}}(9975)$ signal having about 17 times larger $\Upsilon(2S)$ data compared to CLEO, and similar charged hadron identification and photon reconstruction capabilities. This chapter describes a search of the $X_{b\bar{b}}(9975)$ state reconstructed in 26 hadronic final states comprising charged pions, kaons, protons, and K^0_S mesons, in the radiative decay of the $\Upsilon(2S)$. In addition, the $\eta_b(1S)$ state is also searched for in the decay $\Upsilon(2S) \to \gamma\eta_b(1S)$ from the sum of the same 26 modes, as follows:

$2(\pi^+\pi^-)$, $3(\pi^+\pi^-)$, $4(\pi^+\pi^-)$, $5(\pi^+\pi^-)$, $(\pi^+\pi^-)(K^+K^-)$, $2(\pi^+\pi^-)(K^+K^-)$, $3(\pi^+\pi^-)(K^+K^-)$, $4(\pi^+\pi^-)(K^+K^-)$, $2(K^+K^-)$, $(\pi^+\pi^-)2(K^+K^-)$, $2(\pi^+\pi^-)2(K^+K^-)$, $3(\pi^+\pi^-)2(K^+K^-)$, $(\pi^+\pi^-)p\bar{p}$, $2(\pi^+\pi^-)p\bar{p}$, $3(\pi^+\pi^-)p\bar{p}$, $4(\pi^+\pi^-)p\bar{p}$, $(\pi^+\pi^-)(K^+K^-)p\bar{p}$, $2(\pi^+\pi^-)(K^+K^-)p\bar{p}$, $3(\pi^+\pi^-)(K^+K^-)p\bar{p}$, $\pi^\pm K^\mp K^0_S$, $(\pi^+\pi^-)\pi^\pm K^\mp K^0_S$, $2(\pi^+\pi^-)\pi^\pm K^\mp K^0_S$, $3(\pi^+\pi^-)\pi^\pm K^\mp K^0_S$, $(\pi^+\pi^-)2K^0_S$, $2(\pi^+\pi^-)2K^0_S$, and $3(\pi^+\pi^-)2K^0_S$

In the search, the spin-triplet $\chi_{bJ}(1P)$ states serve as a good control sample as the E1 transitions $\Upsilon(2S) \to \gamma\chi_{bJ}(1P)$ have large branching fractions, $(3.8 \pm 0.4)\%$, $(6.9 \pm 0.4)\%$, and $(7.15 \pm 0.35)\%$ for $J = 0, 1,$ and 2, respectively [13].

3.1 Data and MC Samples

The study is performed with the $24.7\,\mathrm{fb}^{-1}$ data that contain $(157.8 \pm 3.6) \times 10^6$ $\Upsilon(2S)$ events [61]. A $1.7\,\mathrm{fb}^{-1}$ of off-resonance data sample, collected 30 MeV below the $\Upsilon(2S)$ peak, provides a good though small sample to study the $e^+e^- \to q\bar{q}$ $(q = u, d, s, c)$ continuum background. Hence, an $89.48\,\mathrm{fb}^{-1}$ of off-resonance data sample recorded 60 MeV below the $\Upsilon(4S)$ is also used.

Half a million signal MC events are produced for each of the 26 hadronic final states arising from the decay of all $(b\bar{b})$ states, i.e., $X_{b\bar{b}}(9975)$, $\eta_b(1S)$ and $\chi_{bJ}(1P)(J = 0, 1, 2)$ with the `EvtGen` [63] package. The radiative decay of $\Upsilon(2S)$ is generated using the helicity amplitude (`HELAMP`) formalism [67, 68], details of which are given in Appendix B.1. Later, we have also verified that the angular distribution of the photon in data is in agreement with the `HELAMP` prediction for each signal of $\chi_{bJ}(1P)$ $(J = 0, 1, 2)$; this cross-check is discussed in Appendix B.2. Furthermore, hadronic decays of the $(b\bar{b})$ are modeled with the phase space (`PHSP`) model, where to incorporate final state radiation effects an interface to `PHOTOS` [69–71] has been added. As $(b\bar{b})$ decays are generated with an assumption of a phase distribution, possible intermediate states such as $\rho^0 \to \pi^+\pi^-$, $\phi \to K^+K^-$, $K^\star(892)^0 \to K^\pm\pi^\mp$ and $K^\star(892)^\pm \to K^0_S\pi^\pm$ are considered to estimate systematic uncertainties on the efficiency.

Inclusive $\Upsilon(2S)$ MC events, generated using Pythia [65] with the same luminosity as the data, are utilised to investigate potential peaking backgrounds.

3.2 $\Upsilon(2S)$ Reconstruction

In all of the 26 modes, the final state particles are charged hadrons[1] that come from the $(b\bar{b})$ decay and a photon arising from the radiative decay of $\Upsilon(2S)$ to the $(b\bar{b})$ state. Figure 3.1 shows the sketch of an event which has six charged tracks in the final state, shown by blue dotted curves, and a photon whose direction is denoted by a red dashed arrow. Reconstruction of the $\Upsilon(2S)$ starts by selecting an appropriate number and type of charged particles. Selection criteria of these charged tracks are discussed in Section 3.2.1. By combining the four-momentum

[1] The K^0_S candidates are reconstructed from a pair of oppositely charged pions.

of these charged tracks a $(b\bar{b})$ system is formed. A photon, selected as a candidate for the radiative decay (see Section 3.2.2), is then combined with the $(b\bar{b})$ to get an $\Upsilon(2S)$ candidate.

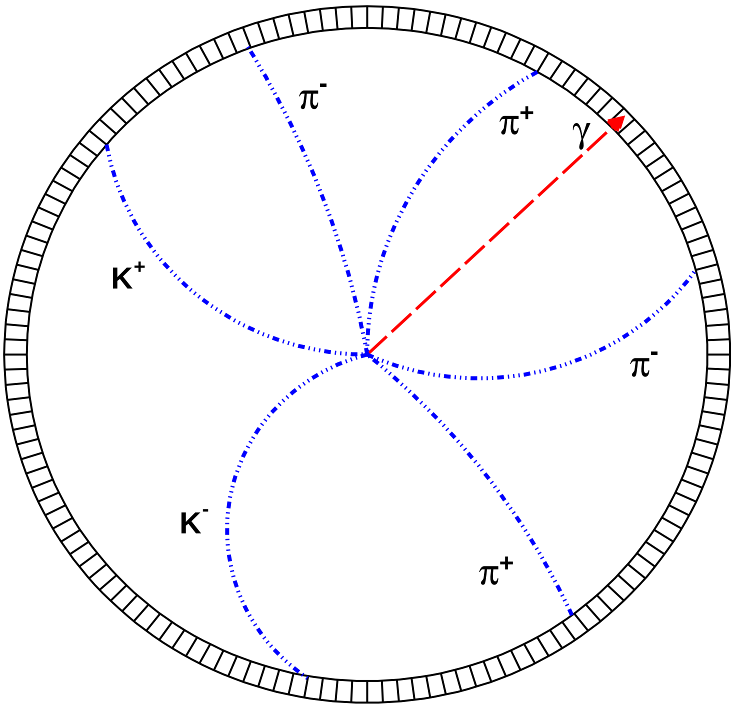

FIGURE 3.1: Sketch of a signal event with six charged tracks and a photon.

3.2.1 $(b\bar{b})$ Reconstruction

All charged tracks in the final state, except for those coming from $K_S^0 \to \pi^+\pi^-$, are selected as follows:

- Impact parameter: To ensure that charged tracks are originating from the interaction point (IP), conditions are applied on the distance of closest approach with respect to the IP. The impact parameters dr and dz are distances in the transverse xy plane and along the z-axis. Figure 3.2 shows the distribution of dr (left) and dz (right), and the corresponding conditions applied are $|dr| < 1\,\text{cm}$ and $|dz| < 4\,\text{cm}$.

- Number of good charged tracks: 'Good Tracks' are defined as the tracks with $p_T > 100$ MeV/c. Distribution of number of good charged tracks is shown in Figure 3.3 and a condition on it (4, 6, 8, or 10) is applied depending on the mode.

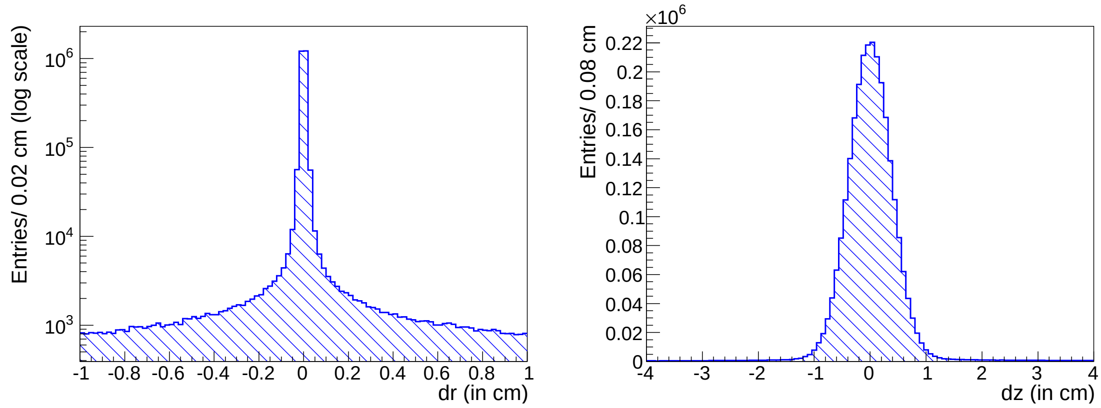

FIGURE 3.2: Impact parameter, dr (left) and dz (right), distributions in the signal MC sample of $X_{b\bar{b}}(9975) \to 3\pi^+3\pi^-$

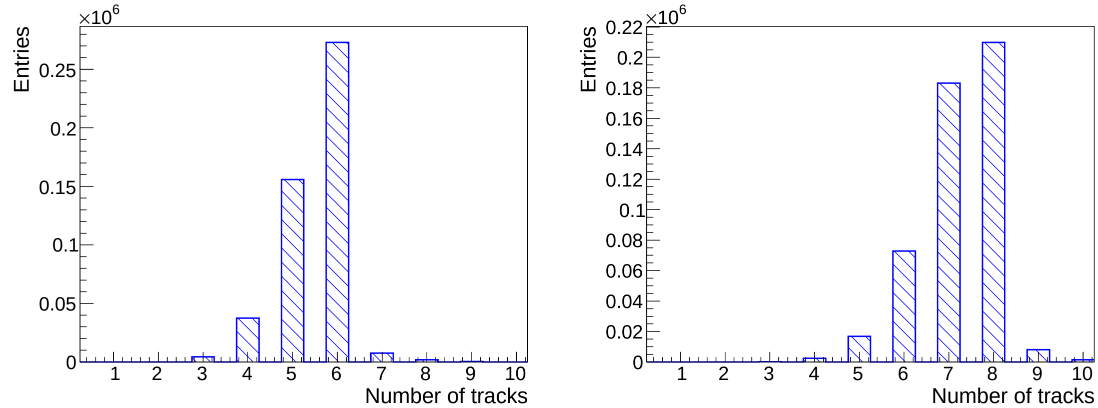

FIGURE 3.3: Distributions of number of good track in the signal MC samples of $X_{b\bar{b}}(9975) \to 3\pi^+3\pi^-$ (left) and $X_{b\bar{b}}(9975) \to 4\pi^+4\pi^-$ (right). It can be seen that the maximum of distributions is at the required number of tracks in that mode.

- Charged pion and kaon selection: Charged pions and kaons are identified based on the likelihood ratios $\mathcal{L}_{K/\pi} = \frac{\mathcal{L}_K}{\mathcal{L}_K+\mathcal{L}_\pi}$ and $\mathcal{L}_{\pi/K} = \frac{\mathcal{L}_\pi}{\mathcal{L}_K+\mathcal{L}_\pi}$ (or, $1 - \mathcal{L}_{K/\pi}$), where $\mathcal{L}_\pi$ and $\mathcal{L}_K$ are the likelihood for $\pi^\pm$ and $K^\pm$, respectively. They are calculated based on the number of photoelectrons from the ACC, information from the TOF and specific ionization in the CDC, explained in Section 2.3. The $\mathcal{L}_{K/\pi}$ distribution is shown in Figure 3.4.
  - $\mathcal{L}_{K/\pi} < 0.4$ for the selection of pions. Also $\pi^\pm$ should not be a daughter of any K_S^0 candidate.
  - $\mathcal{L}_{K/\pi} > 0.6$ for the selection of kaons.

  For the above mentioned condition, the kaon identification efficiency is $83-91\%$ with a pion misidentification probability of $8-10\%$. Pions are detected

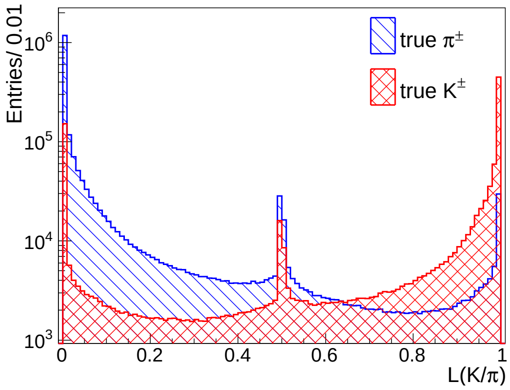

FIGURE 3.4: Distribution of $\mathcal{L}_{K/\pi}$ in the signal MC sample of $X_{b\bar{b}}(9975) \rightarrow 2(\pi^+\pi^-)(K^+\ K^-)$. The red cross-hatched histogram represents truth-matched kaons whereas the blue line hatched histogram denotes correctly reconstructed pions.

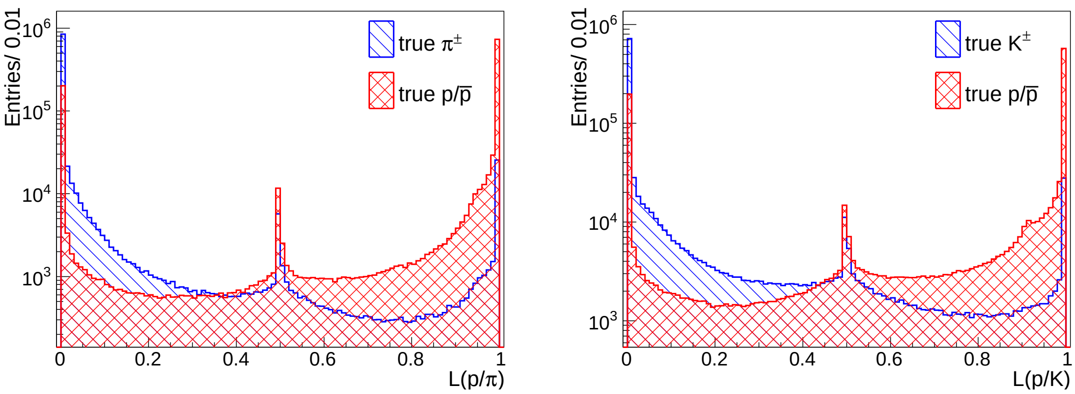

FIGURE 3.5: $\mathcal{L}_{p/\pi}$ (left) and $\mathcal{L}_{p/K}$ (right) distributions are plotted using the signal MC sample of $X_{b\bar{b}}(9975) \rightarrow 2(\pi^+\pi^-)K^+K^-p\bar{p}$.

with an efficiency of $87-89\%$ with a kaon-to-pion misidentification rate of $7-13\%$ [72].

- Selection of $p/\bar{p}$: Protons and antiprotons are identified using the likelihood ratios $\mathcal{L}_{p/K}$ and $\mathcal{L}_{p/\pi}$. The distributions of these ratios are shown in Figure 3.5.

  - $\mathcal{L}_{p/\pi} > 0.7$
  - $\mathcal{L}_{p/K} > 0.7$

  For the above mentioned conditions, the proton identification efficiency is 95%, while the probability of a kaon being misidentified as a proton is below 3% [73, 74].

TABLE 3.1: Good K_S^0 selection [75, 76].

Momentum (GeV/c)	δr (cm)	$\delta\phi$ (rad)	z_{dist} (cm)	f_l (cm)
< 0.5	> 0.05	< 0.3	< 0.8	–
$0.5 - 1.5$	> 0.03	< 0.1	< 1.8	> 0.08
> 1.5	> 0.02	< 0.03	< 2.4	> 0.22

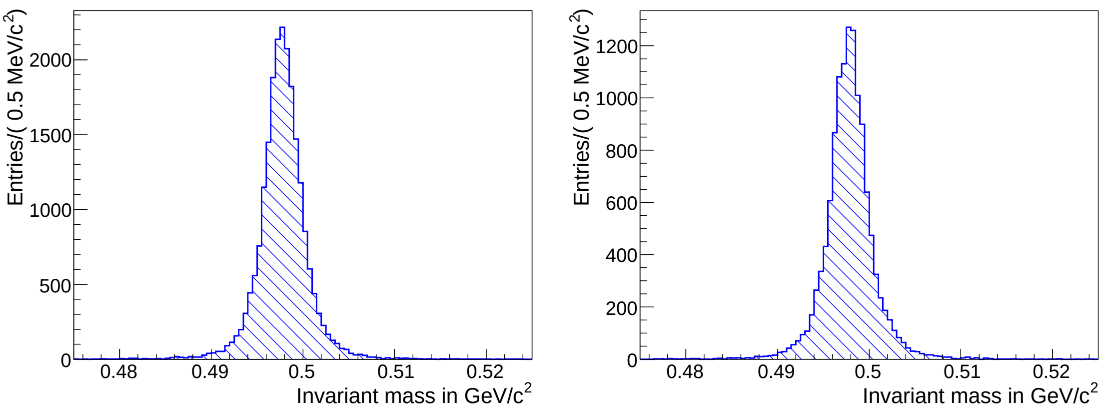

FIGURE 3.6: K_S^0 candidate invariant mass distribution, the signal MC sample used in the left distribution is $X_{b\bar{b}}(9975) \to (\pi^+\pi^-)(\pi^\pm K^\mp)K_S^0$ and in the right distribution is $X_{b\bar{b}}(9975) \to 2(\pi^+\pi^-)2K_S^0$.

- K_S^0 selection: The K_S^0 candidates are reconstructed from a pair of oppositely charged tracks that satisfy a set of criteria listed in Table 3.1. Here, δr is the smallest approach from the IP to both tracks in the xy plane, $\delta\phi$ is the azimuthal angle between the momentum and the decay vertex of the K_S^0 candidate, z_{dist} is the mismatch in the z direction at the K_S^0 vertex point for the charged tracks, and f_l is the flight length of the K_S^0 candidate in the transverse plane. These criteria are optimised for three K_S^0 momentum ranges and are known as Belle standard 'good K_S^0' selection, described in detail in Refs. [75, 76]. Further, the K_S^0 invariant mass from the pair of charged tracks is required to lie between 486 and 509 MeV/c^2, corresponding to 3 standard deviations around the nominal K_S^0 mass [13]. The K_S^0 invariant mass distribution is shown in Figure 3.6.

The $(b\bar{b})$ candidate is reconstructed using the appropriate number and types of selected particles according to the 26 mentioned hadronic modes.

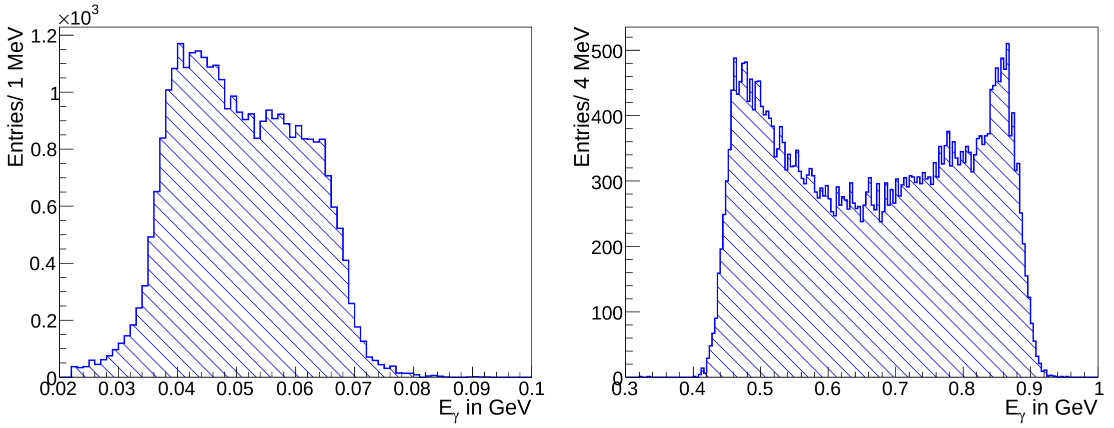

FIGURE 3.7: Distribution of energy of the correctly reconstructed signal photon for $X_{b\bar{b}}(9975)$ (left) and $\eta_b(1S)$ (right) in signal MC events.

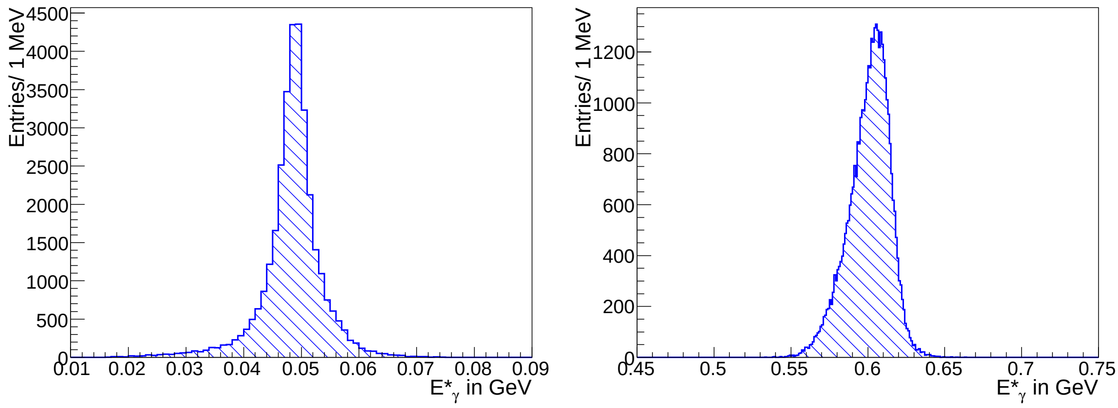

FIGURE 3.8: Distribution of energy of the correctly reconstructed signal photon in the CM frame for $X_{b\bar{b}}(9975)$ (left) and $\eta_b(1S)$ (right) in signal MC events.

3.2.2 γ Selection

The photon candidates coming from the radiative decay $\Upsilon(2S) \to \gamma(b\bar{b})$ are selected based on following quantities:

- Energy of the photon (E_γ): The signal photon has an energy 30 – 70 MeV for $X_{b\bar{b}}(9975)$ and 400 – 900 MeV for $\eta_b(1S)$, as shown in Figure 3.7. The broad energy distribution is due the boosted $\Upsilon(2S)$. On the other hand, the energy distribution in the CM frame $E^\star_\gamma$, (Figure 3.8) peaks at the expected value of 49 MeV for $X_{b\bar{b}}(9975)$ and 620 MeV for $\eta_b(1S)$. A condition $E_\gamma >$ 22 MeV is applied for the signal photon selection.

- E9/E25: Showers in the calorimeter have a variety of shapes and concentrations; sometimes shower shape can be used to identify the initiating particle.

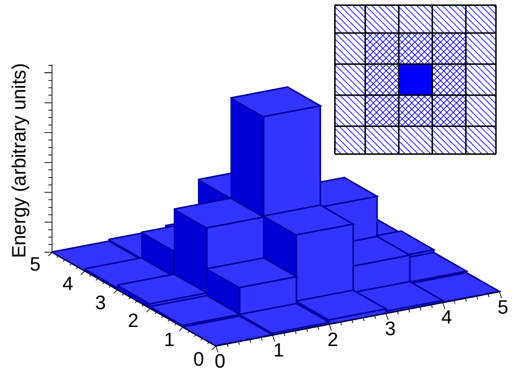

FIGURE 3.9: An illustration for the variable E9/E25. The 2D histogram represents a shower energy profile in the seed crystal and its neighbouring crystals. Inset shows the 5 × 5 crystal block (line filled area), 3×3 crystal block (crossed line filled) and the seed crystal (solid filled).

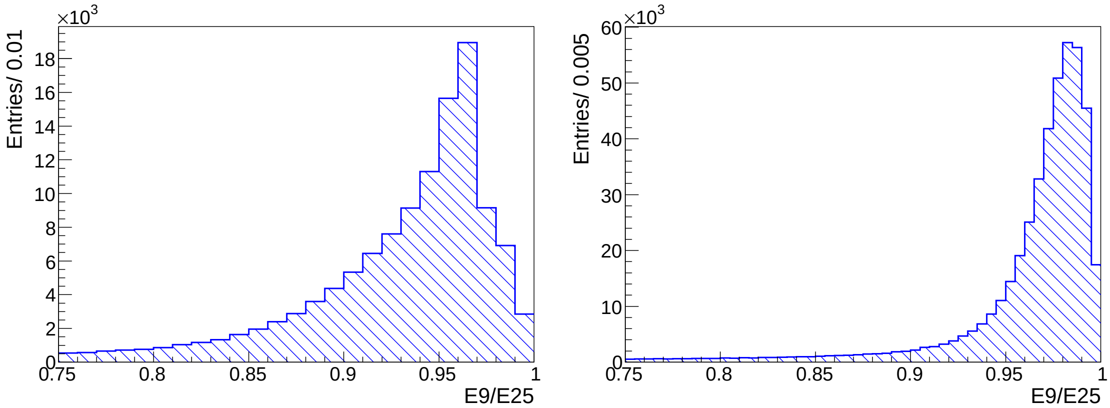

FIGURE 3.10: Distribution of E9/E25 of the correctly reconstructed signal photon for $X_{b\bar{b}}(9975)$ (left) and $\eta_b(1S)$ (right) in signal MC events.

Our requirement is to select the showers consistent with the electromagnetic shower shape. The variable E9/E25 compares the amount of energy deposited in a 3×3 crystal block (E9) to that in a 5×5 crystal block (E25) around the crystal which picks up the maximum energy (seed crystal), pictorially illustrated in Figure 3.9. Distribution of E9/E25 for the $X_{b\bar{b}}(9975)$ and $\eta_b(1S)$ signal photon is shown in Figure 3.10. For candidate photon selection, a condition E9/E25 > 0.85 is applied.

- Charged track matching: The photon cluster in the ECL should not match with a charged track(s) in the CDC. To check matching between the showers and tracks, the tracks are extrapolated up to the crystal front face of the ECL. If the extrapolated track reaches the CsI(Tl) crystal front face, which contains the maximum shower energy, the case is called "shower match" and a flag `match=1` is assigned. When the extrapolated track does not reach any crystal hits of the shower but reaches one of the crystals included in the connected region, `match=2` is assigned [77]. The showers that do not satisfy

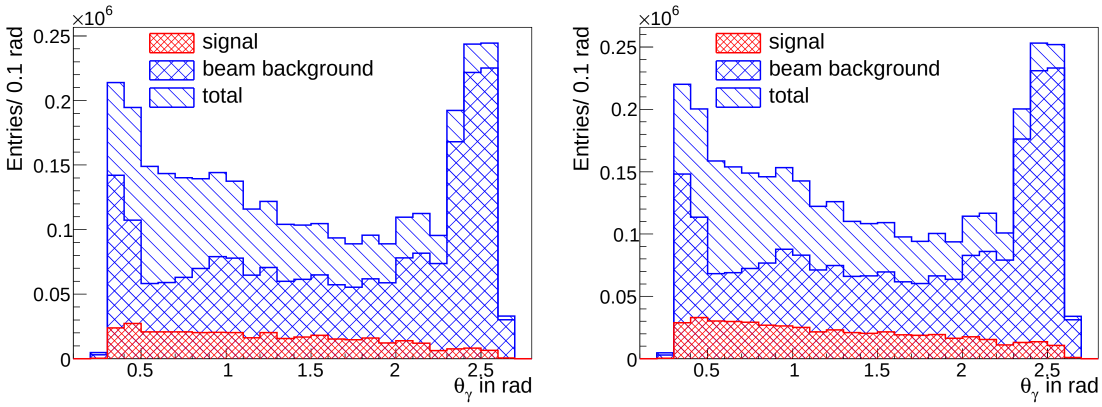

FIGURE 3.11: Polar angle distribution of the photon from $X_{b\bar{b}}(9975)$ (left) and $\eta_b(1S)$ (right) signal MC sample. Blue lined histogram is the total distribution, blue crossed lined histogram is for the photons coming from beam background and red crossed lined histogram is the signal photon.

either `match=1` or `match=2` are categorized as `match=0`. For the candidate photon, only `match=0` cases are retained.

- Polar angle of the photon (θ_γ): Figure 3.11 shows the distribution of the angle between the photon direction and the z-axis in the signal MC sample. Distribution for signal photon is mostly flat with a slight excess towards the forward endcap (coverage: $0.2 < \theta < 0.5$ rad) of the ECL, whereas photons coming from the beam background is predominantly in the backward endcap (coverage: $2.3 < \theta < 2.7$ rad). To suppress beam related background, a criterion $\theta_\gamma < 2.3$ rad is thus applied.

3.2.3 Continuum Suppression

The process $e^+e^- \to q\bar{q}$ ($q = u, d, s, c$), where the quark pairs produced hadronise into light hadrons, is a major source of background and referred to as the continuum background. Light hadrons produced from the quark pairs move along the initial quark direction, as shown in Figure 3.12 (right), and give rise to a back-to-back jet like structure in the CM frame. In contrast, signal events have a spherical topology (because the $\Upsilon(2S)$ is decaying almost at rest), illustrated in Figure 3.12 (left).

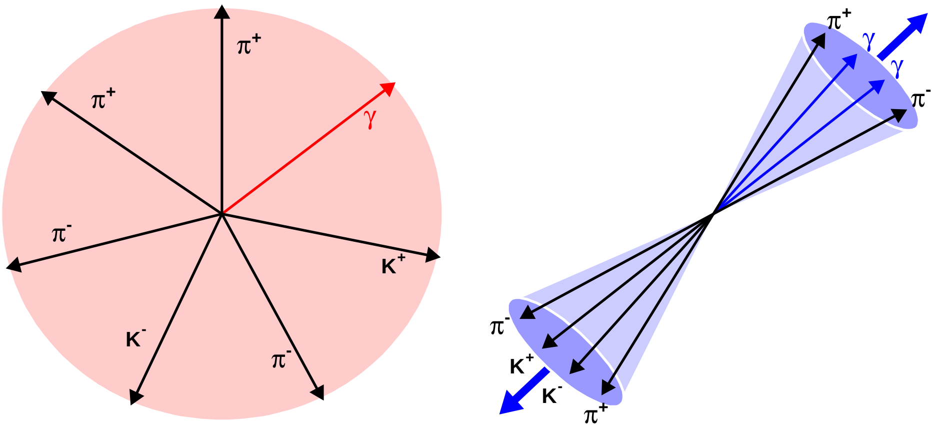

FIGURE 3.12: Schematic diagrams of signal (left) and continuum background event (right).

To exploit this difference in event topology for suppressing the continuum background, a 'thrust axis' is defined as

$$T = \max_{\hat{n_T}} \left(\frac{\sum_i |\vec{p_i} \cdot \hat{n_T}|}{\sum_i |\vec{p_i}|} \right) \tag{3.1}$$

where $\hat{n_T}$ is the thrust axis, along which the projection of the normalized momenta is maximized, $\vec{p_i}$ is momentum of the i-th particle. Once the thrust axis is calculated, the variable $|\cos\theta_T|$, where θ_T is the angle between the thrust axis and the candidate photon, can be used to distinguish between signal and continuum background. For signal events, the thrust axis does not have any preferred direction giving rise to a uniform distribution in $|\cos\theta_T|$, as shown in Figure 3.13, where in case of continuum events, the thrust axis is along either of the jet direction and hence gives the $|\cos\theta_T|$ distribution peaking near 1. The continuum events in the blue lined histogram are from the 1.7 fb^{-1} off-resonance data recorded 30 MeV below the $\Upsilon(2S)$ resonance, and signal events are from the signal MC sample. A requirement $|\cos\theta_T| < 0.8$ is applied for a substantial reduction (60%) of the continuum events at a modest loss (20%) of signal.

3.3 $\Upsilon(2S)$ Selection

An $\Upsilon(2S)$ candidate is formed by combining the reconstructed $(b\bar{b})$ (Section 3.2.1) with the selected photon (Section 3.2.2). The energy of the photon differs significantly between $X_{b\bar{b}}(9975)$ ($\sim$ 50 MeV) and $\eta_b(1S)$ ($\sim$ 600 MeV), and hence

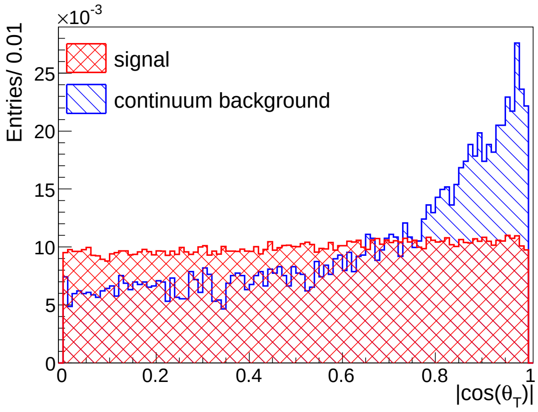

FIGURE 3.13: $|\cos\theta_T|$ (normalised) distribution, flat red-cross lined distribution of signal events are from signal MC sample ($X_{b\bar{b}}(9975) \to 3\pi^+3\pi^-$), and the blue lined distribution peaking near 1 is for continuum background events taken from the $\Upsilon(2S)$ off-resonance data.

following variables are separately optimised for the two signal samples.

- ΔE: It is the difference between the energy of the $\Upsilon(2S)$ candidate and the CM energy. As the beam energy in CM frame is almost equal to the $\Upsilon(2S)$ resonance peak, hence the ΔE distribution for signal is expected to peak near 0.
- $P^\star_{\Upsilon(2S)}$: $\Upsilon(2S)$ candidates are produced at rest, hence the $\Upsilon(2S)$ momentum in the CM frame ($P^\star_{\Upsilon(2S)}$) should also be peaking around 0.
- $\theta_{\gamma(b\bar{b})}$: The process $\Upsilon(2S) \to \gamma(b\bar{b})$ is basically a two-body decay. Therefore, the angle between the candidate photon and the reconstructed $(b\bar{b})$, $\theta_{\gamma(b\bar{b})}$, should be 180°, and can be used as a discriminating variable against background.

3.3.1 Optimization for $X_{b\bar{b}}(9975)$

The signal can be conveniently expressed in terms of ΔM [$= M(\gamma(b\bar{b})) - M(b\bar{b})$], which is the mass difference between the reconstructed $\Upsilon(2S)$ candidate and the $(b\bar{b})$ system. The ΔM distribution for correctly reconstructed $X_{b\bar{b}}(9975)$ events is shown in Figure 3.14. The signal region of $X_{b\bar{b}}(9975)$ is $\Delta M \in (0.04, 0.06)$ GeV/c^2, which constitutes a $\pm 3\sigma$ window around the mean of the distribution.

Dominance of the beam background in this region is evident in Figure 3.15, which is the θ_γ distribution in the generic MC sample, and to suppress this contamination

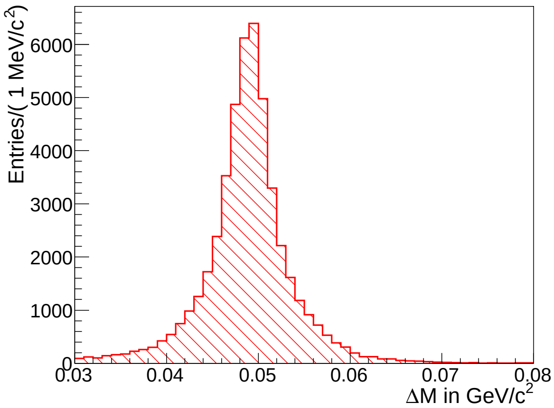

FIGURE 3.14: ΔM distribution for the correctly reconstructed $X_{b\bar{b}}(9975)$ signal in the signal MC sample $X_{b\bar{b}}(9975) \to 3(\pi^+\pi^-)$.

a condition $\theta_\gamma > 0.5$ is applied for the signal selection. In other word, $X_{b\bar{b}}(9975)$ signal photon is selected only from the barrel region of the ECL.

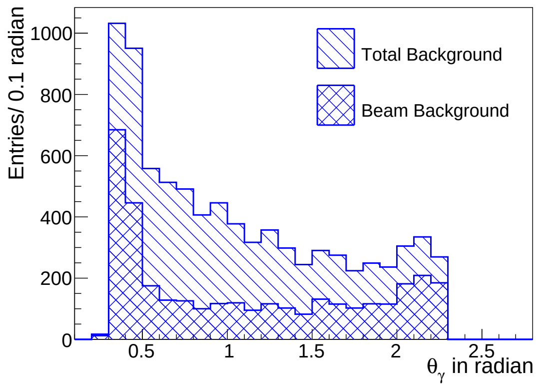

FIGURE 3.15: Polar angle (θ_γ) from the generic MC sample around the $X_{b\bar{b}}(9975)$ signal [$\Delta M \in (0.03, 0.08)\,\mathrm{GeV}/c^2$] region, blue lined histogram is the total background distribution, and blue cross-lined histogram is contrbution from the beam-background.

Optimisation of the selection criteria for $X_{b\bar{b}}(9975)$ signal photon is based on the maximization of the figure-of-merit (FOM) while varying the condition on the variable. The FOM is given by,

$$\mathrm{FOM} = \frac{\mathrm{S}}{\sqrt{\mathrm{S}+\mathrm{B}}} \tag{3.2}$$

where S (B) is the expected signal (background) events for the condition on variable. We estimate S as,

$$\mathrm{S} = N_{\Upsilon(2S)} \times \mathcal{B} \times \varepsilon, \tag{3.3}$$

where $N_{\Upsilon(2S)} = 157.8 \times 10^6$ is the total number of $\Upsilon(2S)$ decays [61] in the data sample, and $\mathcal{B} = 46.2 \times 10^{-6}$ [35] is the product branching fraction, $\mathcal{B}[\Upsilon(2S) \to X_{b\bar{b}}(9975)\gamma] \times \sum_i \mathcal{B}[X_{b\bar{b}} \to h_i]$, where h_i denotes the i-th hadronic state. The efficiency (ε) is calculated from the signal MC sample for the corresponding condition, and B is estimated from the generic MC and scaled[2] off resonance events in the signal window.

1. ΔE: The optimization procedure begins with the variable ΔE. Distribution for the ΔE, normalised to unity, is shown in Figure 3.16. The red-lined histogram is from the signal MC sample of $X_{b\bar{b}}(9975) \to 3(\pi^+\pi^-)$, blue-lined histogram is from the generic MC sample added with scaled off-resonance sample in the $\Delta M < 0.08\,\mathrm{GeV}/c^2$ region (expected background), where as points with error bars are from the data sample in the sideband ($\Delta M \in [0, 0.04] \cup [0.06, 0.08]\,\mathrm{GeV}/c^2$). The optimization plots for ΔE are shown in the bottom two plots of Figure 3.16, where the left (right) plot is for a variation in the negative (positive) side of ΔE. The optimal criterion for signal selection is found to be $\Delta E \in [-0.04, 0.05]\,\mathrm{GeV}$.

2. $P^{\star}_{\Upsilon(2S)}$: After applying conditions for ΔE, optimization of criterion on $P^{\star}_{\Upsilon(2S)}$ is performed. Figure 3.17 (left) shows $P^{\star}_{\Upsilon(2S)}$ distributions (normalized to unity) from signal MC sample, background and the data sideband. The variation of the FOM with conditions applied on the $P^{\star}_{\Upsilon(2S)}$ is shown in the right plot. Though, no clear FOM maximum is found, we apply a criterion for signal selection to be $P^{\star}_{\Upsilon(2S)} < 0.03\,\mathrm{GeV}/c$, which is the tightest condition to have the FOM closer to the maximum value.

3. $\theta_{\gamma(b\bar{b})}$: Figure 3.18 (left) shows $\theta_{\gamma(b\bar{b})}$ distributions from the signal MC, background and data sideband with conditions, $\Delta E \in [-0.04, 0.05]\,\mathrm{GeV}$ and $P^{\star}_{\Upsilon(2S)} < 0.03\,\mathrm{GeV}/c$ applied. Optimal condition is found to be $\theta_{\gamma(b\bar{b})} > 150°$.

3.3.2 Optimization for $\eta_b(1S)$

Distribution of ΔM for correctly reconstructed $\eta_b(1S)$ events is shown in Figure 3.19. The signal region of $\eta_b(1S)$ is $\Delta M \in (0.57, 0.65)\,\mathrm{GeV}/c^2$, which is $\pm 3\sigma$ window around the mean of the distribution.

[2]The off-resonance sample is scaled by a factor 24.7/1.7 (=14.7), as this off-resonance sample of $1.7\,\mathrm{fb}^{-1}$ is to be made equivalent to the $\Upsilon(2S)$ on-resonance sample of $24.7\,\mathrm{fb}^{-1}$.

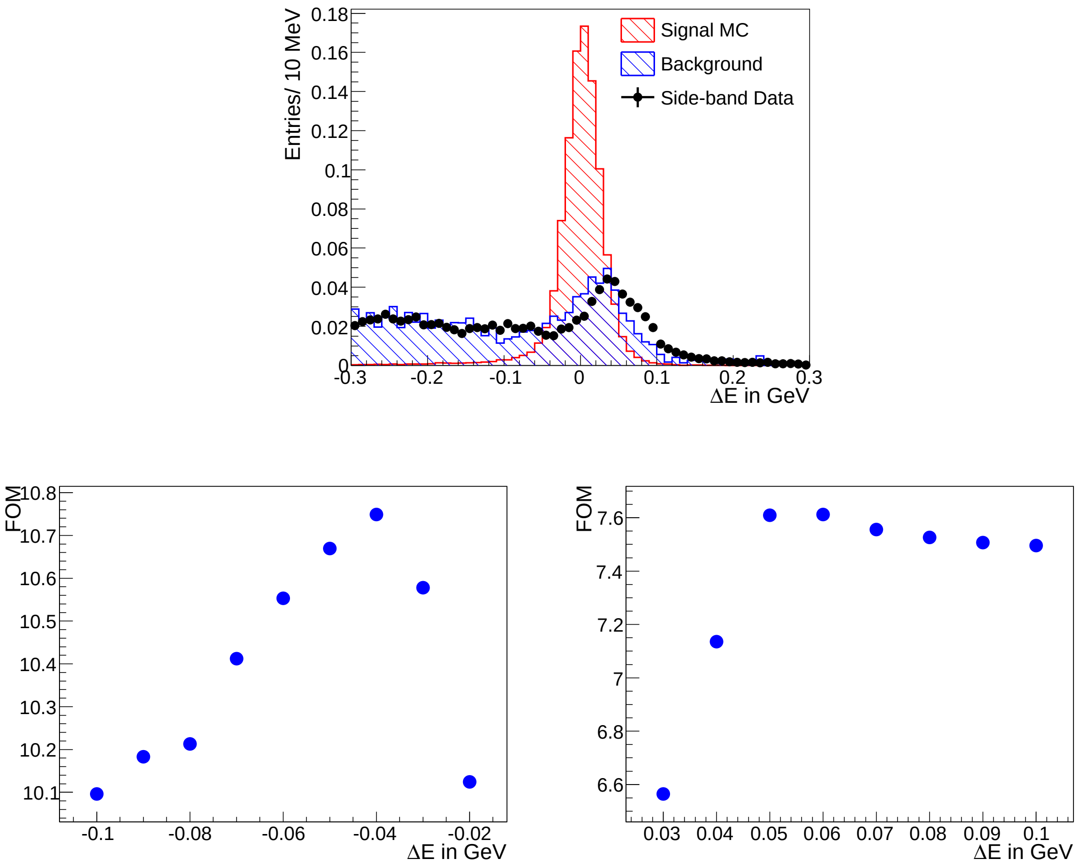

FIGURE 3.16: ΔE distribution (top) from the signal MC sample is red histogram, expected background is the blue histogram, and the data in the side-band are shown by black dots. Plots for FOM *vs.* conditions on ΔE are shown in bottom; the left (right) plot is for a variation in the negative (positive) side of the ΔE.

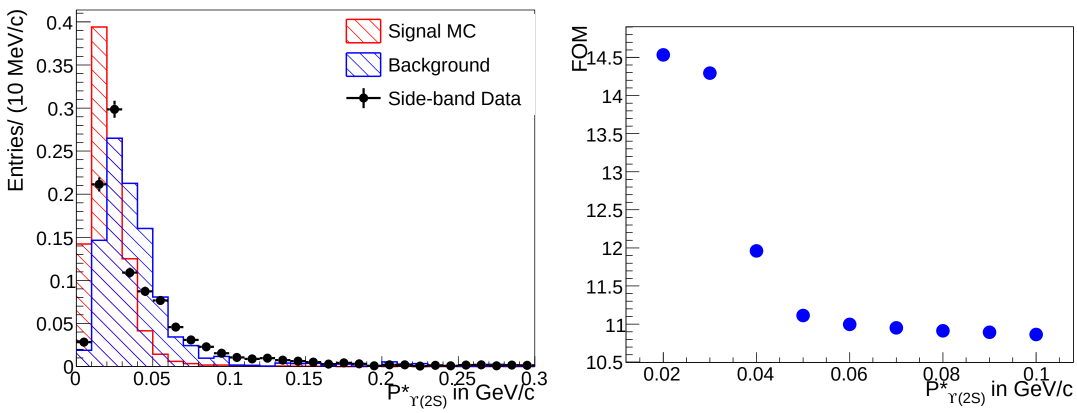

FIGURE 3.17: $P^{\star}_{\Upsilon(2S)}$ distribution (left) from the signal MC sample is red histogram, expected background is the blue histogram, and the data in the side-band are shown by black dots, and (right) variation of the FOM with conditions applied on the $P^{\star}_{\Upsilon(2S)}$.

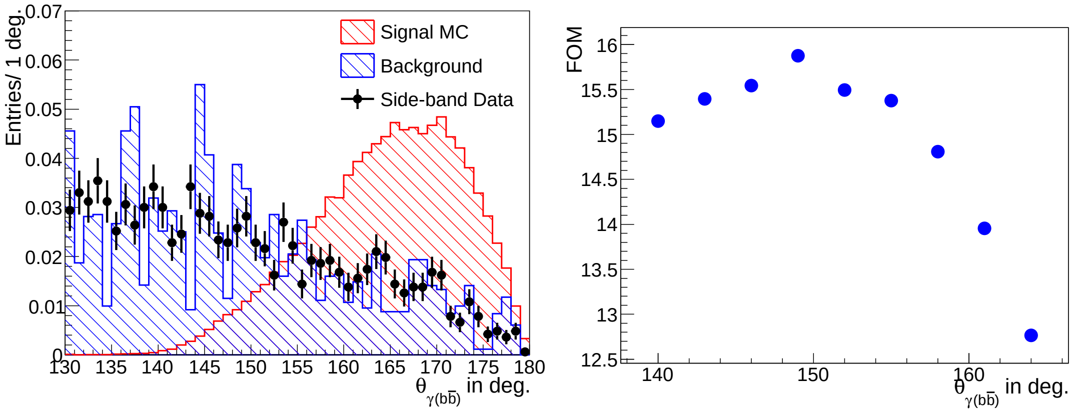

FIGURE 3.18: $\theta_{\gamma(b\bar{b})}$ distribution (left) from the signal MC sample is red histogram, expected background is the blue histogram, and the data in the side-band are shown by black dots, and (right) variation of the FOM with conditions applied on the $\theta_{\gamma(b\bar{b})}$.

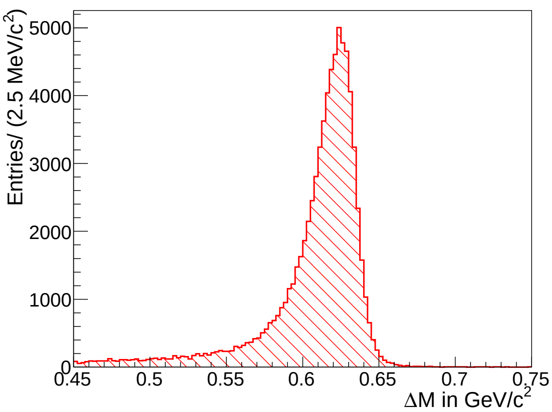

FIGURE 3.19: ΔM distribution for correctly reconstructed $\eta_b(1S)$ signal in the signal MC sample of $\eta_b(1S) \to 3(\pi^+\pi^-)$.

Optimisation of selection criteria for the $\eta_b(1S)$ signal photon is performed by maximising FOM already defined in Eq. (3.2). For estimating expected signal events given in Eq. (3.3), we use the product branching fraction value, $\mathcal{B}[\Upsilon(2S) \to \eta_b(1S)\gamma] \times \sum_i \mathcal{B}[\eta_b(1S) \to h_i] = 3.9 \times 10^{-6}$, where h_i denotes the i-th hadronic state. Here $\mathcal{B}[\Upsilon(2S) \to \eta_b(1S)\gamma] = 3.9 \times 10^{-4}$ is taken from Ref. [30] and $\mathcal{B}[\eta_b(1S) \to h_i]$ is assumed to be 1%. Number of background events is estimated from a combination of the generic MC and scaled off-resonance events in the signal window.

1. ΔE: Here also, the optimization procedure begins with the variable ΔE. Figure 3.20 (left) shows the same distribution (normalised to unity); the red line histogram is from the signal MC sample $\eta_b(1S) \to 3(\pi^+\pi^-)$, blue line histogram is from the generic MC sample added with scaled off-resonance

sample in the $\Delta M \in [0.45, 0.75]$ GeV/c^2 region (expected background), and black points with error bars are from the data sample in the sideband ($\Delta M \in [0.45, 0.57] \cup [0.65, 0.75]$ GeV/c^2). The sideband data points are in good agreement with the expected background distribution. The optimization plot for a variation in negative side of the ΔE is shown in the right plot of Figure 3.20. The optimal criterion for signal selection is found to be $\Delta E \in [-0.03, 0.08]$ GeV.[3]

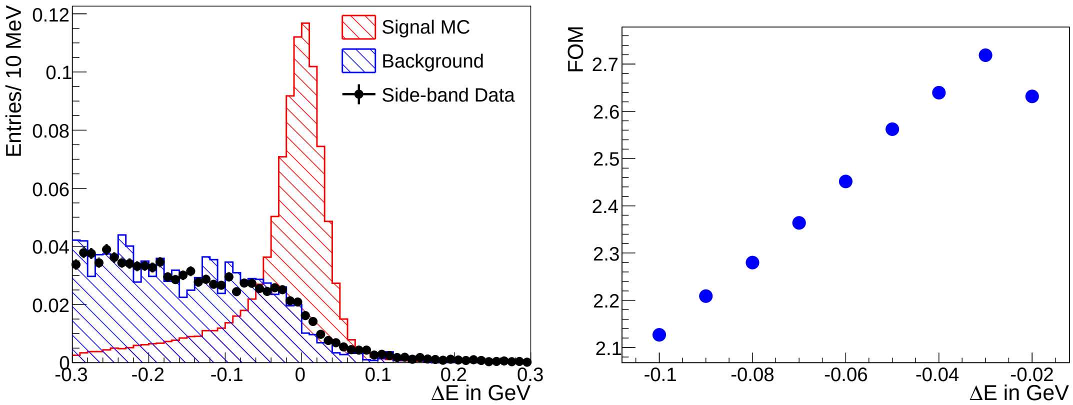

FIGURE 3.20: ΔE distribution (left) from the signal MC sample is red histogram, expected background is the blue histogram and the data in the sideband are shown by black dots. Plot for FOM *vs.* conditions on ΔE is shown in the right plot for a variation in the negative side of the ΔE.

2. $P^{\star}_{\Upsilon(2S)}$: After applying conditions for ΔE, optimization of criteria on $P^{\star}_{\Upsilon(2S)}$ is performed. Figure 3.21 (left) shows $P^{\star}_{\Upsilon(2S)}$ distributions from the signal MC sample, background and the data sideband. The variation of the FOM with conditions applied on $P^{\star}_{\Upsilon(2S)}$ is shown in the right. Optimal criterion for signal selection is found to be $P^{\star}_{\Upsilon(2S)} < 0.05$ GeV/c.

3. $\theta_{\gamma(b\bar{b})}$: Figure 3.22 (left) shows $\theta_{\gamma(b\bar{b})}$ distributions from signal MC, background and the data sideband with conditions, $\Delta E \in [-0.03, 0.08]$ GeV and $P^{\star}_{\Upsilon(2S)} < 0.05$ GeV/c applied. The optimal condition is found to be $\theta_{\gamma(b\bar{b})} > 177°$.

The $\eta_b(1S)$ signal region is found to be affected from photons coming from π^0 decays and to suppress this background we require a dedicated 'π^0 veto'. For this, the difference between the nominal π^0 mass [13] and an invariant mass formed from the signal photon and any other photon in the event is computed for each

[3] In the positive side of ΔE no clear FOM maximum is found, we apply $\Delta E < 0.08$, which is the tightest condition to have the FOM closer to the maximum value.

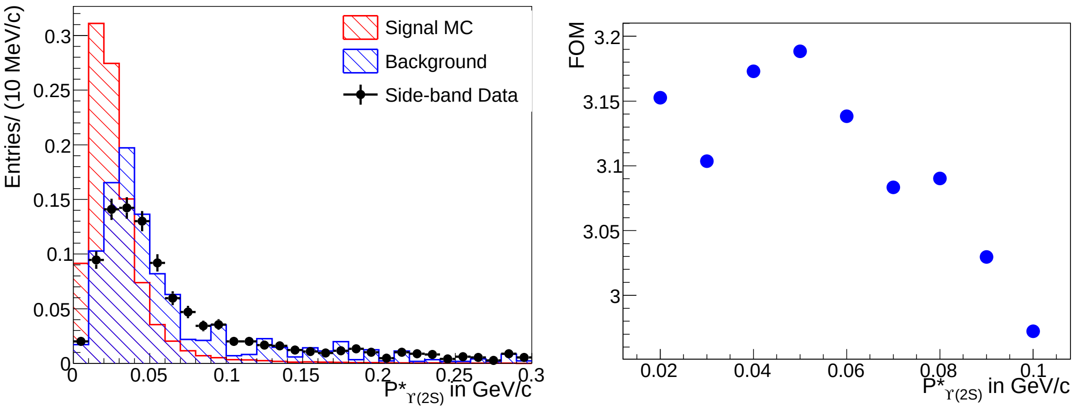

FIGURE 3.21: $P^{\star}_{\Upsilon(2S)}$ distribution (left) from the signal MC sample is red histogram, expected background is the blue histogram, and the data in the sideband are shown by black dots, and (right) variation of the FOM with conditions applied on the $P^{\star}_{\Upsilon(2S)}$.

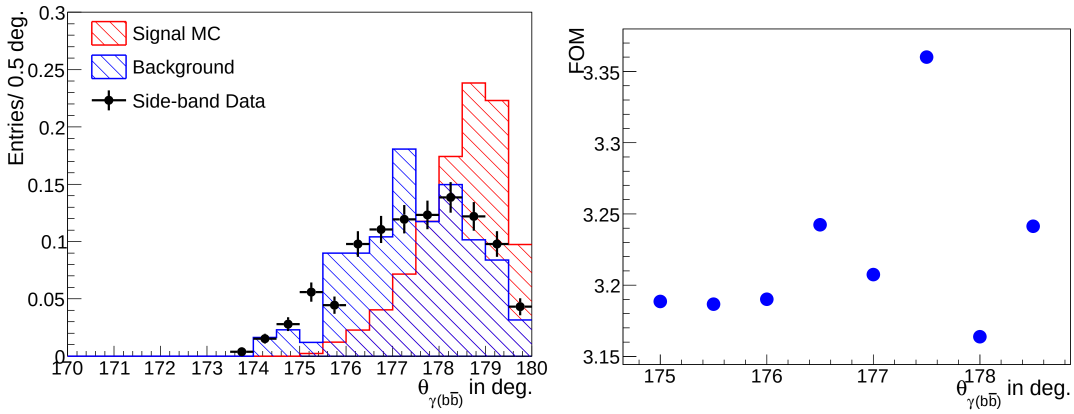

FIGURE 3.22: $\theta_{\gamma(b\bar{b})}$ distribution (left) from the signal MC sample is red histogram, expected background is the blue histogram and the data in the sideband are shown by black dots, and (right) variation of the FOM with conditions applied on the $\theta_{\gamma(b\bar{b})}$.

photon pair, and the smallest magnitude of these differences ($\Delta M_{\gamma\gamma}$) is recorded. Figure 3.23 (right) presents the $\Delta M_{\gamma\gamma}$ distribution from the generic MC sample with correctly reconstructed photons originating from a π^0 decay, shown in the crossed line histogram. In left of Figure 3.23 is the distribution from the signal MC sample as the red histogram, the expected background as the blue histogram and the sideband data are shown by black dots. To veto the background due to π^0, a condition $\Delta M_{\gamma\gamma} > 0.01\,\text{GeV}/c^2$ is applied.

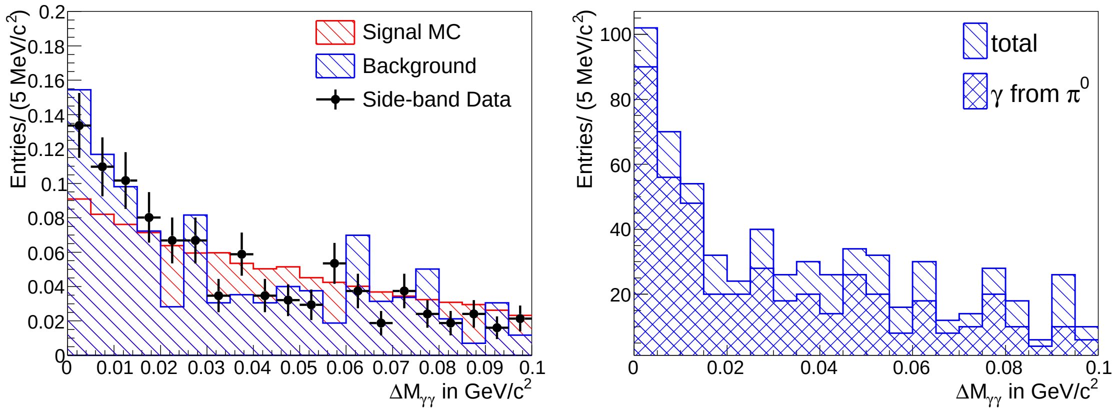

FIGURE 3.23: $\Delta M_{\gamma\gamma}$ distribution (left) from the signal MC sample is red histogram, expected background is the blue histogram and the data in the sideband are shown by black dots, and (right) in the generic MC sample with photons originating from a π^0 decay.

3.3.3 Kinematic Fit

After all above event selection criteria applied, we perform a kinematic fit (discussed in Appendix B.3) on the selected $\Upsilon(2S)$ candidates by imposing energy-momentum conservation. The resolution of the ΔM distribution for $\eta_b(1S)$ is significantly improved by this fit, from approximately 14 to 8 MeV/c^2 as shown in Figure 3.24 (left). The improvement in the mass resolution is modest for the $X_{b\bar{b}}(9975)$ signal, shown in Figure 3.24 (right), as the photon has so little energy.

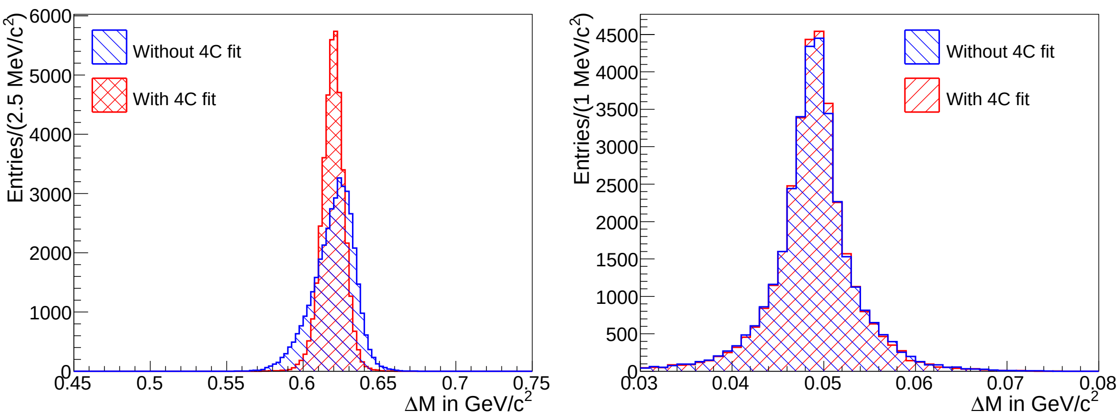

FIGURE 3.24: Effect of kinematic fit on the resolution of ΔM distribution for the $\eta_b(1S)$ and $X_{b\bar{b}}(9975)$ candidate.

There is a possibility of multiple $\Upsilon(2S)$ candidates appearing in an event. Candidate multiplicity arises largely due to more than one photon, originating mostly from beam related backgrounds that pass all the selection criteria applied. In case of $\eta_b(1S)$, there is no multiple candidates found as shown in Figure 3.25 (left).

However, multiple candidate appears in about 10% of the events satisfying the $X_{b\bar{b}}(9975)$ selection. The χ^2 from the kinematic fit (aka 4C fit) can be used to select the best candidate.

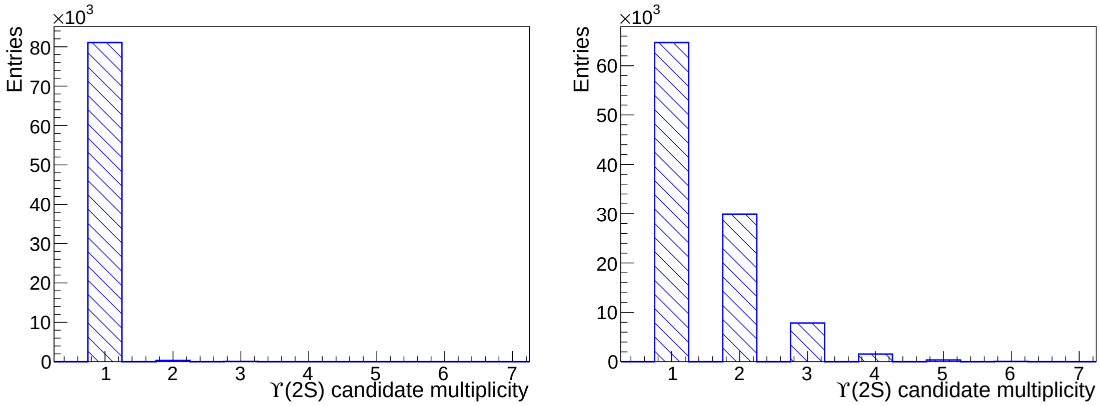

FIGURE 3.25: $\Upsilon(2S)$ candidate multiplicity for $\eta_b(1S)$ (left) and $X_{b\bar{b}}(9975)$ (right).

3.3.4 Maximum Likelihood Fit

To decide the probability density function (PDF) of the each signal component, the respective signal MC distributions are studied. In signal MC, the $X_{b\bar{b}}(9975)$ signal component is parametrized by the sum of a Gaussian and an asymmetric Gaussian function (to take into account of low energy tails) and a first order Chebyshev polynomial for the background component. The fit is illustrated in Figure 3.26 (left), the yield obtained for the signal component is used to obtain the efficiency of each mode. In the case of three $\chi_{bJ}(1P)$, which are our control sample, the same PDF as the $X_{b\bar{b}}(9975)$ is used. As an example, for the $\chi_{b1}(1P)$ case the distribution is shown in Figure 3.26 (right). The Gaussian component of signal (shown in the red dashed line) in the case of $X_{b\bar{b}}(9975)$ is narrower than the χ_{bJ}'s but has a larger tail component of the asymmetric Gaussian (shown in the green dashed line).

The fit to the ΔM distribution in data is done in the $(0.03, 0.30)$ GeV/c^2 range that includes the eventual $X_{b\bar{b}}(9975)$ peak region as well as the three $\chi_{bJ}(1P)$ peaks, whose yields are expected to be few hundreds in our sample. The signals, as mentioned earlier, are fitted with the sum of two Gaussians, where the three widths and the fraction between the two Gaussians are fixed from the MC sample of the corresponding signal in all the reconstructed modes. These parameters are

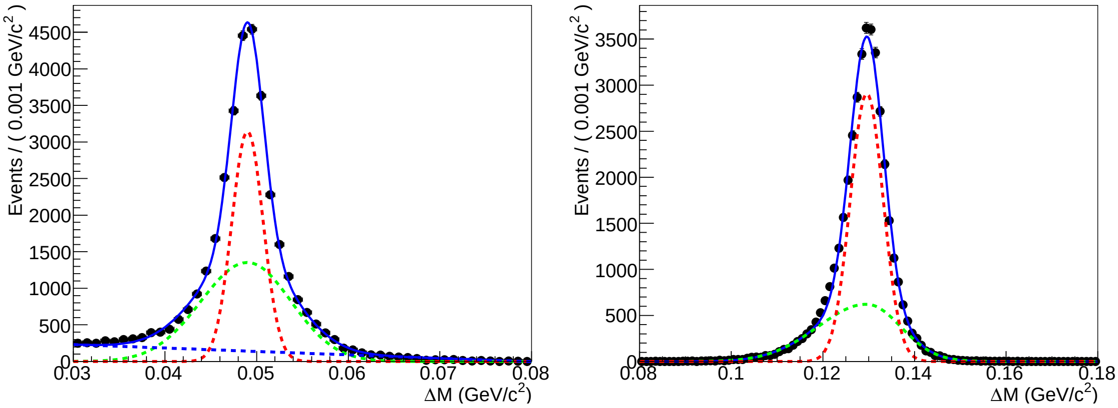

FIGURE 3.26: Fit to the ΔM distribution from the $X_{b\bar{b}}(9975)$ (left) and $\chi_{b1}(1P)$ (right) in the signal MC samples. Blue solid curves are the result from the fit, red dashed curves denote is the core Gaussian component and the green dashed curves represent the asymmetric Gaussian component of signal.

very close in the different modes, and when plotting each parameter of all the 26 modes, the distribution has a small RMS. Each parameter is fixed to the mean value of this distribution and the RMS is used for the variation to estimate the assorted systematic uncertainty. In the $X_{b\bar{b}}(9975)$ case, we use the same procedure to fix the mean as well. To take into account of the possible difference in resolution between MC and data, a fudge factor is allowed to vary for the sigma of the main Gaussian; this factor is common to all the four signal PDFs.

Background is fitted with the sum of an exponential function and a first order Chebyshev polynomial, the corresponding three parameters (fraction, exponential factor and slope of polynomial) are allowed to vary in the fit. The background PDF is validated by fitting the ΔM distribution of off-resonance data recorded 60 MeV below the $\Upsilon(4S)$ resonance, as shown in Figure 3.27. This is in contrast to Ref. [35], where a single exponential function was used to describe the background PDF. The polynomial component is critically needed to model the background due to final-state radiation for $\Delta M < 0.15\,\mathrm{GeV}/c^2$ and from π^0 for $\Delta M \geq 0.15\,\mathrm{GeV}/c^2$ and thus only an exponential won't be sufficient to fit the background.

Before fitting the $\Upsilon(2S)$ data, a sample composed of an $\Upsilon(2S)$ generic MC sample and a scaled $\Upsilon(4S)$ off-resonance sample is fitted. The resulting fit is illustrated in Figure 3.28. The fudge factor obtained, 0.94 ± 0.41, is consistent with 1. This shows that our procedure to estimate the difference in resolution between the sample fitted and the signal MC is working properly. The means of the $\chi_{b2}(1P)$, $\chi_{b1}(1P)$ and $\chi_{b0}(1P)$ are 109.84 ± 0.30, 130.09 ± 0.31, and 162.07 ± 0.22 MeV/c^2

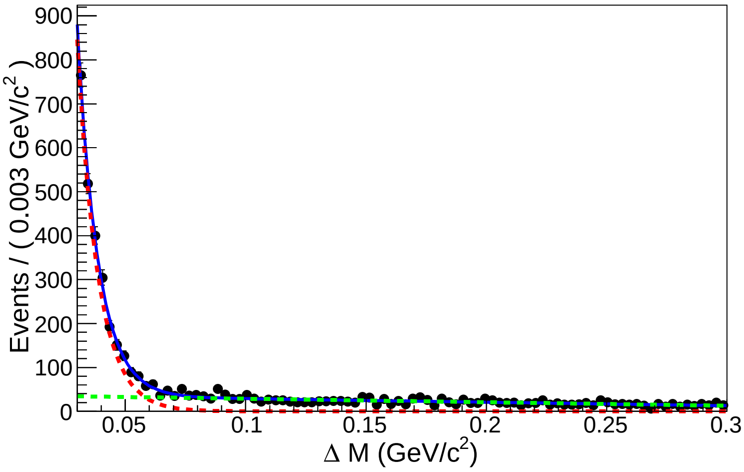

FIGURE 3.27: Fit to the ΔM distribution of the $\Upsilon(4S)$ off-resonance data for $\Delta M \in (0.03, 0.30)$ GeV/c^2, black dots with error bars are data points, blue solid curve is the result from the fit, red dashed curve denotes the exponential component and the green dashed curve represent the first-order Chebyshev polynomial component of the total fit.

that correspond to a mass of 9913.42 ± 0.31, 9893.17 ± 0.31, and 9861.19 ± 0.22 MeV/c^2, respectively. These values are consistent with generated mass values listed in Table B.1.

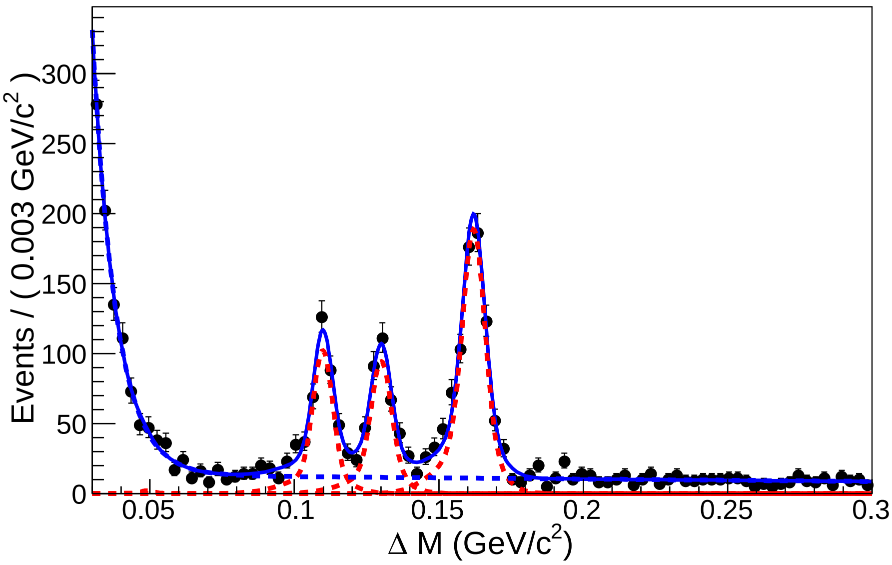

FIGURE 3.28: Fit for ΔM distribution of generic MC and scaled off-resonance data for $\Delta M \in (0.03, 0.30)$ GeV/c^2, blue solid curve is the result from the fit, blue dashed curve denotes background component, and red dashed curves represent signal components.

Figure 3.29 (top) illustrates the fit to the ΔM distribution in the $\Upsilon(2S)$ data sample and the bottom plot is a zoomed up version in the $X_{b\bar{b}}(9975)$ region. The yield of $X_{b\bar{b}}(9975)$ is found -29.6 ± 18.7, consistent with no signal. The background shape is consistent with the one found for the $\Upsilon(4S)$ off-resonance sample (Figure 3.27). The fudge factor, which represents the data-MC difference for the resolution, is found to be 1.23 ± 0.05, in reasonable agreement with the usual Belle estimations. The chi^2/NDF of the fit is found to be 0.91. The large statistic available in our sample for the $\chi_{bJ}(1P)$ (from 300 to 950 candidates) allows to determine precisely (with an accuracy competitive with the world average) the $\chi_{bJ}(1P)$ masses and are listed in Table 3.2. Complete fit result is listed in Table B.2 of Appendix B.4.

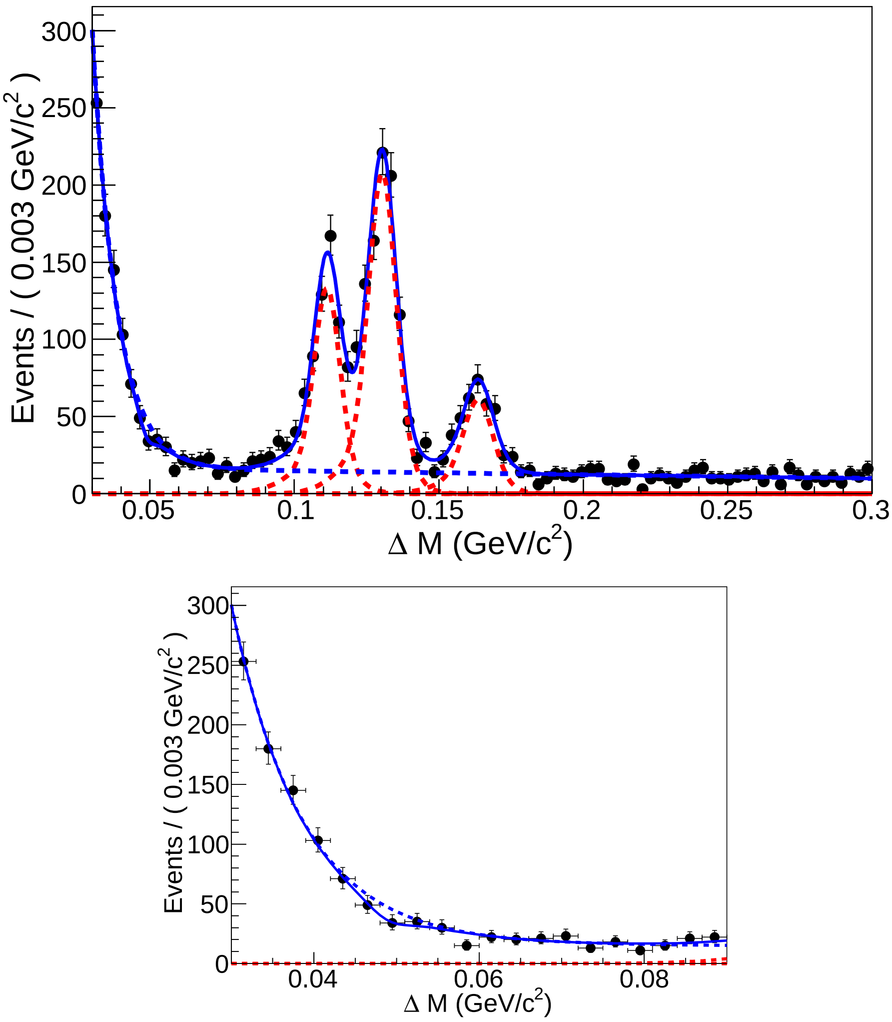

FIGURE 3.29: Fit to the ΔM distribution of $\Upsilon(2S)$ on-resonance data sample for $\Delta M \in (0.03, 0.30)\,\mathrm{GeV}/c^2$, is shown by blue solid curves, points with error bars are the data, red dashed curves are the signal component, and blue dashed curve is the background component of the fit. The bottom plot shows a zoomed view of the ΔM distribution in the $[0.03, 0.09]\,\mathrm{GeV}/c^2$ region.

The signal PDF for the $\eta_b(1S)$ is a Breit-Wigner function, whose width is fixed to the value obtained in Ref. [32], convolved with a Gaussian function with a

TABLE 3.2: Summary of the $\chi_{bJ}(1P)$ masses in the fit to the ΔM distribution in the $\Upsilon(2S)$ data sample.

	ΔM (GeV/c^2)	Mass (MeV/c^2)	Mass(PDG) [13] (MeV/c^2)
$\chi_{b0}(1P)$	0.16363 ± 0.00049	9859.63 ± 0.49	$9859.44 \pm 0.42 \pm 0.31$
$\chi_{b1}(1P)$	0.13043 ± 0.00023	9892.83 ± 0.23	$9892.78 \pm 0.26 \pm 0.31$
$\chi_{b2}(1P)$	0.11127 ± 0.00034	9912.00 ± 0.34	$9912.21 \pm 0.26 \pm 0.31$

width of $8\,\mathrm{MeV}/c^2$ describing the detector resolution. The latter is estimated by studying the signal MC sample of all the 26 modes. An example fitting to the signal MC sample for the $3(\pi^+\pi^-)$ mode is demonstrated in Figure 3.30 (left). A first-order Chebyshev polynomial is used for background in the $\eta_b(1S)$ region, which is validated with the large sample of $\Upsilon(4S)$ off-resonance data. The result of the fit to off-resonance data is presented in the right plot of Figure 3.30.

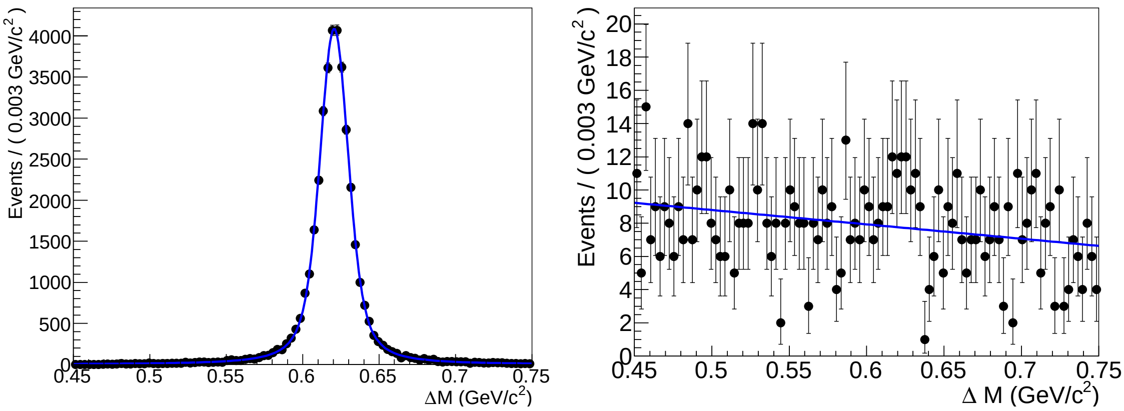

FIGURE 3.30: Fit to the ΔM distribution of the $\eta_b(1S)$ signal MC and $\Upsilon(4S)$ off-resonance data samples for $\Delta M \in (0.45, 0.75)\,\mathrm{GeV}/c^2$.

No signal (-6 ± 10 events) is found for the $\eta_b(1S)$. Fit to the ΔM distribution in $\Upsilon(2S)$ data is shown in Figure 3.31 while complete fit result can be found in Table B.3 of Appendix B.4.

3.4 Efficiency Estimation

For a particle of mass near $10\,\mathrm{GeV}/c^2$, exclusive decays are distributed across many final states. Thus the $\chi_{bJ}(1P)$ decay modes are used as a guidance to estimate the average efficiency $\varepsilon[(b\bar{b})]$ for both $X_{b\bar{b}}(9975)$ and $\eta_b(1S)$. The $\varepsilon[(b\bar{b})]$ is calculated

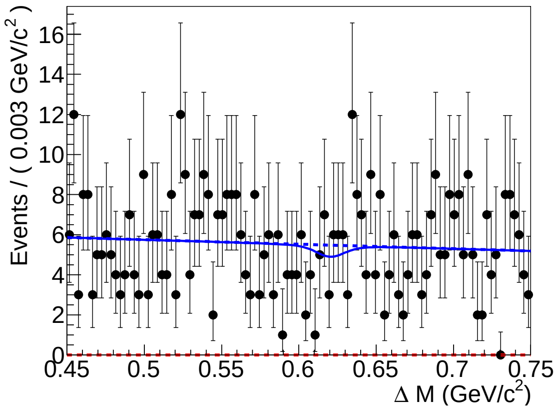

FIGURE 3.31: Fit to the ΔM distribution of the $\eta_b(1S)$ region in the $\Upsilon(2S)$ on-resonance data sample for $\Delta M \in (0.45, 0.75)$ GeV/c^2.

with the individual efficiencies $[\varepsilon^i_{(b\bar{b})}]$ obtained from signal MC samples weighted according to the yields $[N^i_{\chi_{bJ}(1P)}]$ for each mode in the $\chi_{bJ}(1P)$ case, as

$$\varepsilon[(b\bar{b})] = \sum_{i=1}^{26} \frac{\varepsilon^i_{(b\bar{b})} \times N^i_{\chi_{bJ}(1P)}}{N^{\text{tot}}_{\chi_{bJ}(1P)}}, \tag{3.4}$$

where $N^{\text{tot}}_{\chi_{bJ}(1P)}$ denotes the total sum of signal yields obtained for the 26 hadronic decays of the $\chi_{bJ}(1P)$. Similar results are obtained in the three cases of $\chi_{bJ}(1P)(J = 0, 1, 2)$: 3.99%, 4.05%, and 3.78%, respectively, for $X_{b\bar{b}}(9975)$. The $\chi_{b0}(1P)$ case is selected for further calculation as it is a scalar like $\eta_b(1S)$ and $X_{b\bar{b}}(9975)$ [claimed to be $\eta_b(2S)$]. The main decays contributing to $\chi_{b0}(1P)$ are found to be $3(\pi^+\pi^-)$ [14.42%], $4(\pi^+\pi^-)$ [12.33%], $2(\pi^+\pi^-)(K^+K^-)$ [11.91%], $4(\pi^+\pi^-)(K^+K^-)$ [10.39%], and $3(\pi^+\pi^-)(K^+K^-)$ [8.30%] (in decreasing order of contribution). A calibration factor due to particle identification efficiency difference between data and simulations is also taken into account, where the main difference is found for pions ($\sim$ 95% per pion) with negligible contributions for kaons and protons. The final efficiency is 2.85% for $X_{b\bar{b}}(9975)$ and 3.52% for $\eta_b(1S)$.

3.5 Systematic Error Estimation

Uncertainties on the signal yields due to signal PDF shapes are estimated with $\pm 1\sigma$ variations of the shape parameters that are fixed in the nominal fit. The dominant sources of such additive systematic errors are the $X_{b\bar{b}}(9975)$ [35] and $\eta_b(1S)$ [32] masses. For the upper limit calculation, we conservatively use the fit likelihood, which gives the largest upward variation of the signal yield: 18 and 4 events for the $X_{b\bar{b}}(9975)$ and $\eta_b(1S)$, respectively. The multiplicative systematic uncertainties that do not affect the signal yields are listed in Table 3.3. The largest contribution here comes from the uncertainty in the efficiency estimate. Two sources dominate here: (a) the statistical error in the yield of the different decay modes of the $\chi_{b0}(1P)$, and (b) effects of possible intermediate states on the signal efficiency (referred to as "decay modeling", mentioned in Section 3.1). Differences in the efficiencies based on the same final-state modes generated with the intermediate resonances ($\rho^0, \phi, K^{\star}(892)^0, K^{\star}(892)^{\pm}$) can be as large as 9.2%. The other minor contributions are from hadron identification, charged track reconstruction, K_S^0 and photon detection, and the number of $\Upsilon(2S)$.

TABLE 3.3: Multiplicative systematic uncertainties (in %) considered in the estimation of the $X_{b\bar{b}}(9975)$ (top) and $\eta_b(1S)$ (bottom) upper limits.

Source	$X_{b\bar{b}}(9975)$		
	error (+)	error (−)	error (max.)
Efficiency calculation	+2.5	−2.9	±2.5
Decay modeling	+0.0	−9.2	±9.2
Hadron identification	+3.7	−3.7	±3.7
Track reconstruction	+2.6	−2.6	±2.6
K_S^0 detection	+0.2	−0.2	±0.2
Photon detection	+3.0	−3.0	±3.0
Number of $\Upsilon(2S)$	+2.3	−2.3	±2.3
Total	+6.4	−11.2	±11.2

Source	$\eta_b(1S)$		
	error (+)	error (−)	error (max.)
Efficiency calculation	+2.9	−2.9	±2.9
Decay modeling	+0.0	−6.9	±6.9
Hadron identification	+3.7	−3.7	±3.7
Track reconstruction	+2.6	−2.6	±2.6
K_S^0 detection	+0.2	−0.2	±0.2
Photon detection	+3.0	−3.0	±3.0
Number of $\Upsilon(2S)$	+2.3	−2.3	±2.3
Total	+6.8	−9.5	±9.5

3.6 Results

The branching fraction is determined from the number of observed signal events (n_{sig}) as $\mathcal{B} = n_{\text{sig}}/\{\varepsilon[(b\bar{b})] \times N_{\Upsilon(2S)}\}$, where $\varepsilon[(b\bar{b})]$ is evaluated according to Eq. 3.4

and $N_{\Upsilon(2S)}$ is the total number of $\Upsilon(2S)$ decays. In the absence of the signal, we obtain an upper limit at 90% confidence level (CL) on the branching fraction ($\mathcal{B}_{\rm UL}$) by integrating the likelihood ($\mathcal{L}$) of the fit with fixed values of the branching fraction:

$$\int_0^{\mathcal{B}_{\rm UL}} \mathcal{L}(\mathcal{B})d\mathcal{B} = 0.9 \times \int_0^1 \mathcal{L}(\mathcal{B})d\mathcal{B}. \tag{3.5}$$

Multiplicative systematic uncertainties are included by convolving the likelihood function with a Gaussian function of width equals to the total uncertainty from Table 3.3. We estimate $\mathcal{B}[\Upsilon(2S) \to \eta_b(1S)\gamma] \times \sum_i \mathcal{B}[\eta_b(1S) \to h_i] < 3.7 \times 10^{-6}$ and $\mathcal{B}[\Upsilon(2S) \to X_{b\bar{b}}\gamma] \times \sum_i \mathcal{B}[X_{b\bar{b}} \to h_i] < 4.9 \times 10^{-6}$.

In summary, we have searched for the $X_{b\bar{b}}(9975)$ state reported in Ref. [35], which is reconstructed in 26 exclusive hadronic final states, using a sample of $(157.8 \pm 3.6) \times 10^6$ $\Upsilon(2S)$ decays. We find no evidence for a signal and thus determine a 90% CL upper limit on the product branching fraction $\mathcal{B}[\Upsilon(2S) \to X_{b\bar{b}}\gamma] \times \sum_i \mathcal{B}[X_{b\bar{b}} \to h_i] < 4.9 \times 10^{-6}$, which is an order of magnitude smaller than the value reported in Ref. [35]. We have also verified using a large number of pseudo-experiments that if the $X_{b\bar{b}}(9975)$ signal were present in our data sample we would have observed it with a significance exceeding 10 standard deviations. We have searched for the $\eta_b(1S)$ state as well, where set an upper limit $\mathcal{B}[\Upsilon(2S) \to \eta_b(1S)\gamma] \times \sum_i \mathcal{B}[\eta_b(1S) \to h_i] < 3.7 \times 10^{-6}$ at 90% CL.

CHAPTER 4

Hadronic decays of the $\chi_{bJ}(1P)$ triplet

The recent claim of observing a new state near 9975 MeV/c^2, $X_{b\bar{b}}(9975)$, in the CLEO data is now refuted by us [78], which is already discussed in the previous chapter. In that analysis, we also observe a large signal yield for $\chi_{bJ}(1P)$ states from the sum of 26 exclusive hadronic final states. The observed signal yields for $\chi_{bJ}(1P)(J = 0, 1, 2)$ are 299 ± 22, 946 ± 36 and 582 ± 31, respectively. This motivated us to study the product branching fractions of $\mathcal{B}[\Upsilon(2S) \to \gamma\chi_{bJ}(1P)] \times \mathcal{B}[\chi_{bJ}(1P) \to h_i]$, where h_i is a specific hadronic mode. Our study using the world's largest e^+e^- collision data recorded with the Belle detector in the $\Upsilon(2S)$ decays would not only improve over the earlier measurements of 14 modes [25], but also potentially uncover many new modes. This chapter describes this study.

We have reconstructed the following hadronic decay modes for $\chi_{bJ}(1P)$:

- The 26 charged hadronic modes same as in the previous analysis, $2(\pi^+\pi^-)$, $3(\pi^+\pi^-)$, $4(\pi^+\pi^-)$, $5(\pi^+\pi^-)$, $\pi^+\pi^-K^+K^-$, $2(\pi^+\pi^-)K^+K^-$, $3(\pi^+\pi^-)K^+K^-$, $4(\pi^+\pi^-)K^+K^-$, $2(K^+K^-)$, $\pi^+\pi^-2(K^+K^-)$, $2(\pi^+\pi^-K^+K^-)$, $3(\pi^+\pi^-)2(K^+K^-)$, $\pi^+\pi^-p\bar{p}$, $2(\pi^+\pi^-)p\bar{p}$, $3(\pi^+\pi^-)p\bar{p}$, $4(\pi^+\pi^-)p\bar{p}$, $\pi^+\pi^-K^+K^-p\bar{p}$, $2(\pi^+\pi^-)K^+K^-p\bar{p}$, $3(\pi^+\pi^-)K^+K^-p\bar{p}$, $\pi^\pm K^\mp K^0_S$, $\pi^+\pi^-\pi^\pm K^\mp K^0_S$, $2(\pi^+\pi^-)\pi^\pm K^\mp K^0_S$, $3(\pi^+\pi^-)\pi^\pm K^\mp K^0_S$, $\pi^+\pi^-2K^0_S$, $2(\pi^+\pi^-K^0_S)$, and $3(\pi^+\pi^-)2K^0_S$.
- One π^0 is added to the above charged final states, excluding $2(\pi^+\pi^-)\pi^0$, $3(\pi^+\pi^-)\pi^0$, $4(\pi^+\pi^-)\pi^0$ and $5(\pi^+\pi^-)\pi^0$ as they are forbidden by the G-parity conservation [25]. In total, the following 22 modes with one π^0 are reconstructed,

$\pi^+\pi^-K^+K^-\pi^0$, $2(\pi^+\pi^-)K^+K^-\pi^0$, $3(\pi^+\pi^-)K^+K^-\pi^0$, $4(\pi^+\pi^-)K^+K^-\pi^0$, $2(K^+K^-)\pi^0$, $\pi^+\pi^-2(K^+K^-)\pi^0$, $2(\pi^+\pi^-K^+K^-)\pi^0$, $3(\pi^+\pi^-)2(K^+K^-)\pi^0$, $\pi^+\pi^-p\overline{p}\pi^0$, $2(\pi^+\pi^-)p\overline{p}\pi^0$, $3(\pi^+\pi^-)p\overline{p}\pi^0$, $4(\pi^+\pi^-)p\overline{p}\pi^0$, $\pi^+\pi^-K^+K^-p\overline{p}\pi^0$, $2(\pi^+\pi^-)K^+K^-p\overline{p}\pi^0$, $3(\pi^+\pi^-)K^+K^-p\overline{p}\pi^0$, $\pi^\pm K^\mp K^0_S\pi^0$, $\pi^+\pi^-\pi^\pm K^\mp K^0_S\pi^0$, $2(\pi^+\pi^-)\pi^\pm K^\mp K^0_S\pi^0$, $3(\pi^+\pi^-)\pi^\pm K^\mp K^0_S\pi^0$, $\pi^+\pi^-2K^0_S\pi^0$, $2(\pi^+\pi^-K^0_S)\pi^0$, and $3(\pi^+\pi^-)2K^0_S\pi^0$.

- Further 26 modes are reconstructed with an addition of two π^0's to the charged final states mentioned above.
  $2(\pi^+\pi^-)2\pi^0$, $3(\pi^+\pi^-)2\pi^0$, $4(\pi^+\pi^-)2\pi^0$, $5(\pi^+\pi^-)2\pi^0$, $(\pi^+\pi^-)K^+K^-2\pi^0$, $2(\pi^+\pi^-)K^+K^-2\pi^0$, $3(\pi^+\pi^-)K^+K^-2\pi^0$, $4(\pi^+\pi^-)K^+K^-2\pi^0$, $2(K^+K^-)2\pi^0$, $\pi^+\pi^-2(K^+K^-)2\pi^0$, $2(\pi^+\pi^-)K^+K^-2\pi^0$, $3(\pi^+\pi^-)2(K^+K^-)2\pi^0$, $\pi^+\pi^-p\overline{p}2\pi^0$, $2(\pi^+\pi^-)p\overline{p}2\pi^0$, $3(\pi^+\pi^-)p\overline{p}2\pi^0$, $4(\pi^+\pi^-)p\overline{p}2\pi^0$, $\pi^+\pi^-K^+K^-p\overline{p}2\pi^0$, $2(\pi^+\pi^-)K^+K^-p\overline{p}2\pi^0$, $3(\pi^+\pi^-)K^+K^-p\overline{p}2\pi^0$, $\pi^\pm K^\mp K^0_S2\pi^0$, $\pi^+\pi^-\pi^\pm K^\mp K^0_S2\pi^0$, $2(\pi^+\pi^-)\pi^\pm K^\mp K^0_S2\pi^0$, $3(\pi^+\pi^-)\pi^\pm K^\mp K^0_S2\pi^0$, $\pi^+\pi^-2K^0_S2\pi^0$, $2(\pi^+\pi^-)2K^0_S2\pi^0$, and $3(\pi^+\pi^-)2K^0_S2\pi^0$.

In total, 74 hadronic decay modes of the $\chi_{bJ}(1P)$ are reconstructed comprising charged and neutral pions, kaons, protons, and K^0_S mesons.

4.1 Data and MC Samples

The study is performed with the same data sample used in previous analysis (described in Section 3.1), which contains $(157.8\pm3.6)\times10^6$ $\Upsilon(2S)$ events [61] and the off-resonance sample below $\Upsilon(2S)$ and $\Upsilon(4S)$ resonances for the continuum background study. MC events, same luminosity as the data, of generic $\Upsilon(2S)$ decays are utilised to study the potential peaking background.

Half a million signal MC events are produced for 48 hadronic modes with π^0's other than the previously generated 26 modes. In the newly generated modes also, the radiative decay of $\Upsilon(2S)$ is generated by the helicity amplitude (`HELAMP`) model [67, 68], details are given in Appendix B.1. The hadronic decays of $\chi_{bJ}(1P)$ are modeled with the phase space (`PHSP`) model, where final state radiation effects are incorporated with an interface to `PHOTOS` [69–71]. Here, to estimate the systematic uncertainties due to a phase space assumption for the hadronic decays, possible intermediate states considered are, $\rho^0\to\pi^+\pi^-$, $\rho^\pm\to\pi^\pm\pi^0$, $\phi\to K^+K^-$, $\omega\to\pi^+\pi^-\pi^0$, $K^\star(892)^0\to K^\pm\pi^\mp/K^0_S\pi^0$, and $K^\star(892)^\pm\to K^0_S\pi^\pm/K^\pm\pi^0$.

4.2 $\Upsilon(2S)$ Reconstruction

The reconstruction procedure begins with selecting and reconstructing final state hadrons to form a $\chi_{bJ}(1P)$ system, which is further combined with a selected photon originating from the radiative decay to form an $\Upsilon(2S)$ candidate. Figure 4.1 shows a typical sketch of an event, which has six charged tracks in the final state, shown by blue dash-dotted curves and three photons two of which arising from a π^0 decay are shown by blue dotted arrows and the photon from the radiative decay is shown by the red dashed arrow.

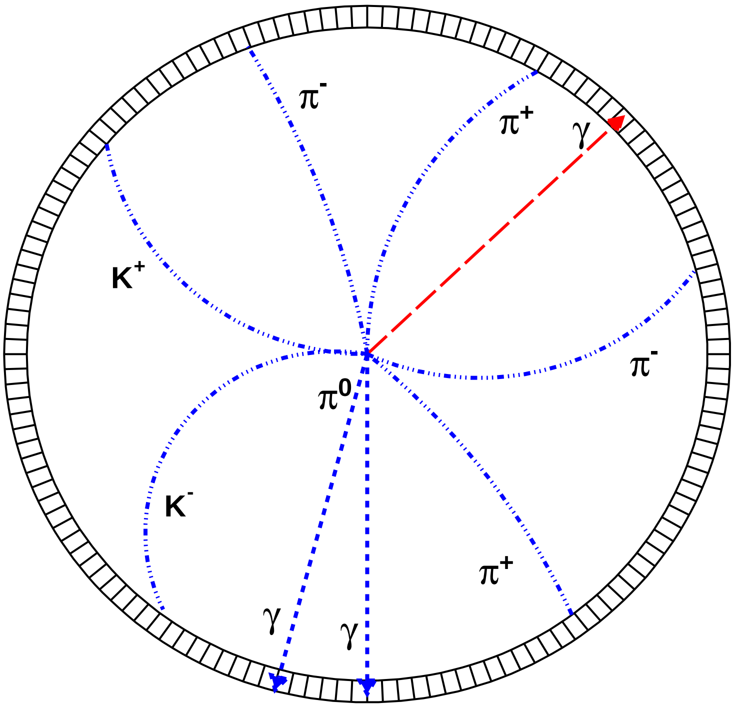

FIGURE 4.1: Sketch of a signal event with six charged tracks, a photon pair coming from a π^0 decay, and a photon from the radiative decay.

4.2.1 $\chi_{bJ}(1P)$ Reconstruction

The $\chi_{bJ}(1P)$ is reconstructed from its daughter charged and neutral hadrons (K_S^0 and π^0). Requirements on charged hadrons in the final state (except for those coming from $K_S^0 \to \pi^+\pi^-$), K_S^0 and π^0 reconstruction are discussed below.

- Impact parameter: Condition on the impact parameters are $|dr| < 1\,\text{cm}$ and $|dz| < 4\,\text{cm}$.

- Number of charged tracks: The number of good charged tracks are selected as 4, 6, 8, or 10 depending on the mode.

- Charged pion and kaon selection: Charged pions and kaons are identified based on the likelihood ratio $\mathcal{L}_{K/\pi}$, and its distribution is shown in Figure 4.2.

  - $\mathcal{L}_{K/\pi} < 0.6$ for the selection of pions. Also $\pi^{\pm}$ should not be a daughter of any K^0_S candidate.
  - $\mathcal{L}_{K/\pi} > 0.6$ for the selection of kaons.

  For the above mentioned condition the kaon identification efficiency is $81-90\%$ with a pion misidentification probability of $9-14\%$. Pions are detected with an efficiency of $91-95\%$ with a kaon-to-pion misidentification rate of $8-13\%$.

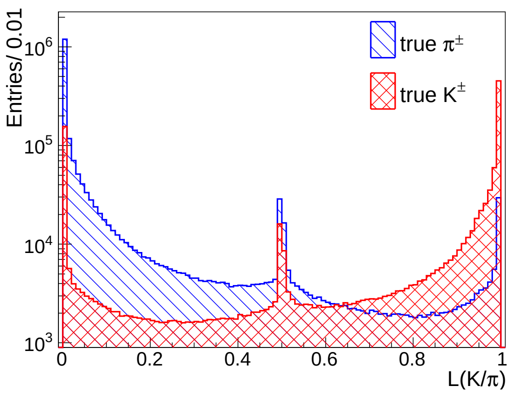

FIGURE 4.2: Distribution of $\mathcal{L}_{K/\pi}$ in the signal MC sample of $\chi_{b1}(1P) \to 2(\pi^+\pi^-)(K^+K^-)$. The red cross-hatched histogram represents truth-matched kaons whereas the blue line hatched histogram denotes correctly reconstructed pions.

- Selection of $p/\overline{p}$: protons and antiprotons are identified using the likelihood ratios $\mathcal{L}_{p/K}$ and $\mathcal{L}_{p/\pi}$. The distributions of these ratios are shown in Figure 4.3.

  - $\mathcal{L}_{p/\pi} > 0.7$
  - $\mathcal{L}_{p/K} > 0.7$

  For the above mentiontioned conditions the proton identification efficiency is 95%, while the probability of a kaon being misidentified as a proton is below 3%.

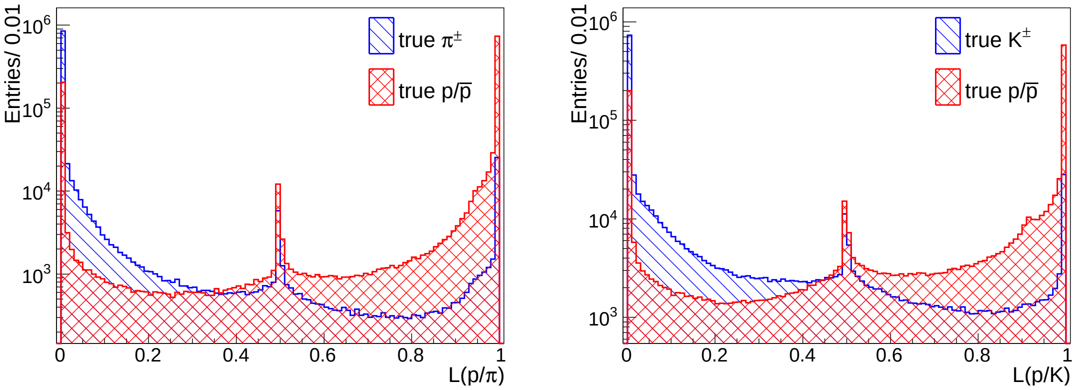

FIGURE 4.3: $\mathcal{L}_{p/\pi}$ (left) and $\mathcal{L}_{p/K}$ (right) distributions obtained from the signal MC sample of $\chi_{b1}(1P) \to 2(\pi^+\pi^-)K^+K^-p\bar{p}$.

- K_S^0 reconstruction: The K_S^0 candidates are reconstructed in the same way as described in the Section 3.2.1. Further, the K_S^0 invariant mass from the pair of charged tracks should lie between $[486, 509]$ MeV/c^2, which corresponds to $\pm 3\sigma$ around the nominal K_S^0 mass [13].

- π^0 reconstruction: A π^0 is reconstructed from a pair of photons, each having energy greater than 100 MeV. The reconstructed π^0 should have an invariant mass between $[113, 157]$ MeV/c^2, which corresponds to $\pm 3.5\sigma$ around the nominal π^0 mass [13].

The $\chi_{bJ}(1P)$ candidate is reconstructed using as appropriate number and types of selected particles according to the 74 mentioned hadronic modes.

4.2.2 γ Selection

The radiative photon candidates coming from the process, $\Upsilon(2S) \to \gamma\chi_{bJ}(1P)$, are chosen based on the following quantities, already defined in Section 3.2.2:

- Energy of the photon (E_γ): The signal photon has energy $100 - 240$ MeV for $\chi_{b0}(1P)$, $70 - 190$ MeV for $\chi_{b1}(1P)$, and $50 - 170$ MeV for $\chi_{b2}(1P)$. In Figures 4.4, 4.5, and 4.6 the signal energy distributions are shown for $\chi_{bJ}(1P)$, $J = 0,\ 1$, and 2, respectively, in the laboratory (left) and CM frame (right). A condition $\text{E}_\gamma > 30$ MeV is applied for the signal photon selection.

- E9/E25: To ensure the showers in the calorimeter consistent with electromagnetic shower shape, a condition E9/E25 > 0.85 is applied.

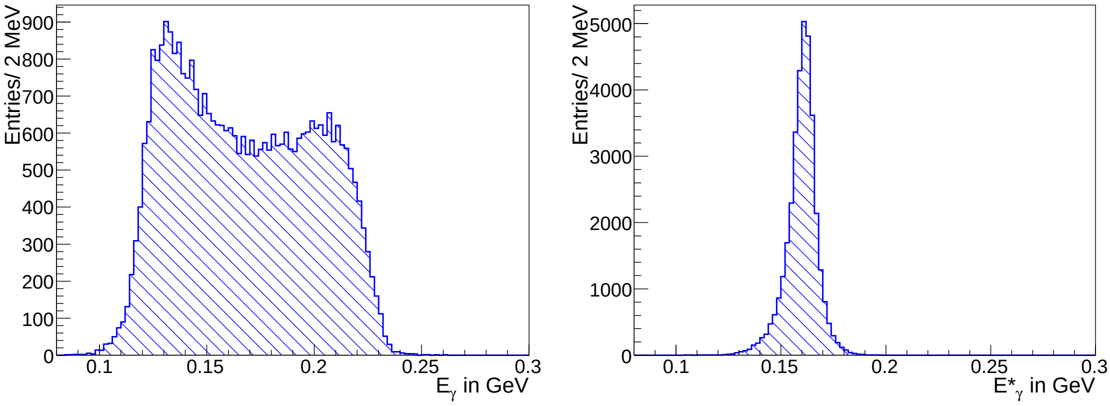

FIGURE 4.4: Distribution of energy of the correctly reconstructed signal photon for $\chi_{b0}(1P)$ in the laboratory (left) and CM frame (right).

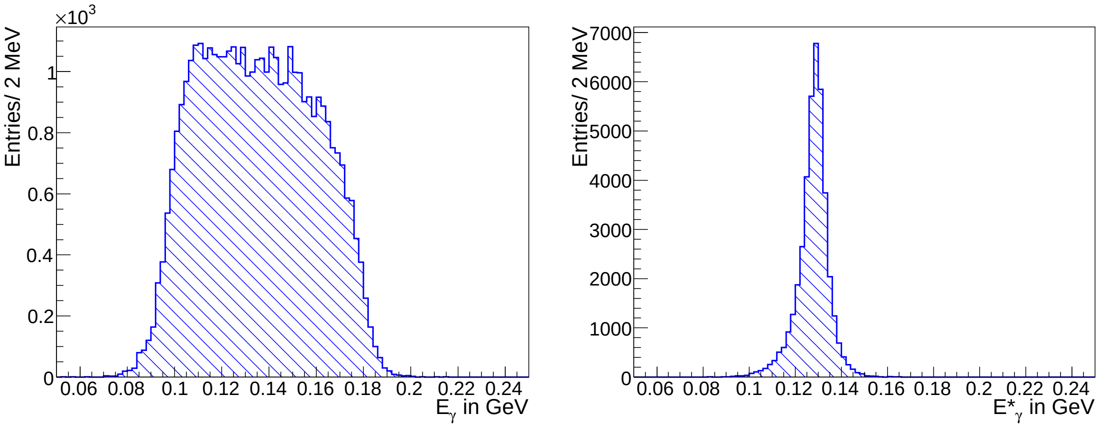

FIGURE 4.5: Distribution of energy of the correctly reconstructed signal photon for $\chi_{b1}(1P)$ in the laboratory (left) and CM frame (right).

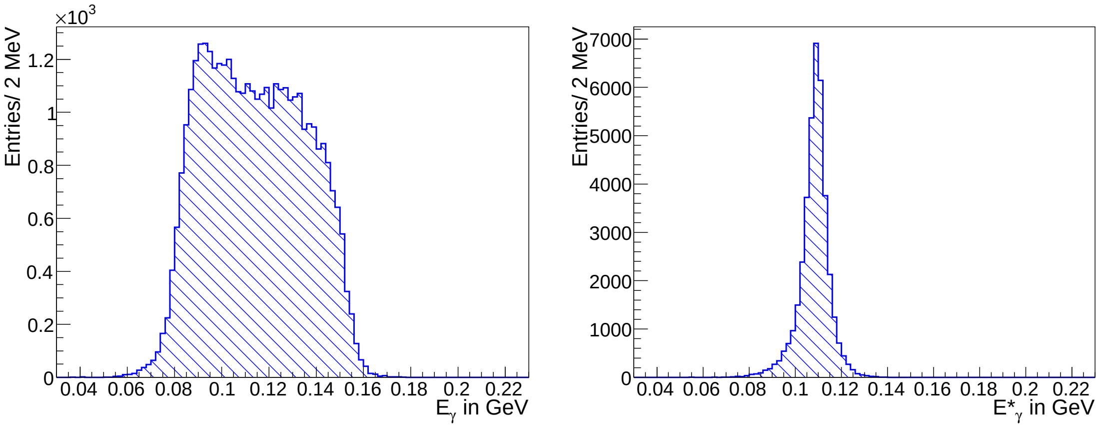

FIGURE 4.6: Distribution of energy of the correctly reconstructed signal photon for $\chi_{b2}(1P)$ in the laboratory (left) and CM frame (right).

- Charged track matching: The electromagnetic shower should not match with any charged track in the CDC for the signal photon selection.

- Polar angle of the photon (θ_γ): To reduce the beam related background, only photons in the barrel region satisfying the condition $\theta_\gamma \in [0.5,\ 2.3]$ rad are selected.

- The candidate γ should not be coming from a π^0 reconstructed for $\chi_{bJ}(1P)$.

4.2.3 Continuum Suppression

Continuum events comprise the light (u, d, s and c) quark-antiquark pairs produced in e^+e^- collisions. They have a 'back-to-back' jetlike topology in contrast to spherical signal events. To suppress this background, the cosine of the angle between the photon candidate and the thrust axis (calculated from the final state hadrons), $\cos\theta_T$, is used. Signal events have a uniform distribution (shown as the red histogram in Figure 4.7) in this variable while continuum events peak near $|\cos\theta_T| = 1$ (shown as the blue histogram in Figure 4.7). A requirement $|\cos\theta_T| < 0.8$ is applied to reduce the continuum background.

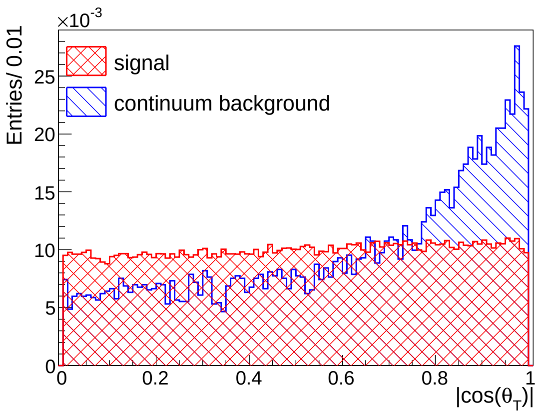

FIGURE 4.7: Normalised $|\cos\theta_T|$ distributions, flat red-cross lined distribution of signal events is from the MC sample of $\chi_{b1}(1P) \to 3(\pi^+\pi^-)$, and the blue lined distribution peaking near 1 is for continuum background events taken from the $\Upsilon(2S)$ off-resonance data.

4.3 Kinematic Fit and χ^2 Cut

A kinematic fit imposing energy-momentum conservation (4C) can help in improving the mass resolution since all the final state particles are reconstructed. The χ^2 from the 4C fit can also be used as a selection criterion for signal (and to select the best candidate if multiple candidates are found). In our previous analysis, we have verified that applying a selection criterion on the χ^2 is equivalent to applying selection criteria on variables $P^*_{\Upsilon(2S)}$ and ΔE. The 4C-fit is discussed in detail in Appendix B.3.

After the pre-selection criteria and continuum suppression described above, an optimised criterion on reduced χ^2 (χ^2/NDF) is applied for further background suppression. Optimisation is done for the signal $\chi_{b0}(1P)$ because it is also the signal of interest for the width measurement. As the branching fraction information is mostly available for the $\chi_{b1}(1P)$ decays, the optimisation is performed for two branching fraction cases: (a) sum of the product branching fractions ($\mathcal{B}[\Upsilon(2S) \to \gamma\chi_{b1}(1P)] \times \mathcal{B}[\chi_{b1}(1P) \to X_i]$) for 13 modes (available in Ref. [25], excluding upper limit), multiplied by the ratio of the sum of signal yields for $\chi_{b0}(1P)$ and $\chi_{b1}(1P)$ in those modes, and (b) the product branching fraction as in case (a), but it is varied around ($\pm1\sigma$) the obtained uncertainty.

The $\chi_{b0}(1P)$ signal region in ΔM ($M[\Upsilon(2S)] - M[\chi_{bJ}(1P)]$) distribution is defined as $[138, 180]\,\mathrm{MeV}/c^2$, which corresponds to a $\pm3\sigma$ window. The variation of the expected signal yield with reduced χ^2 is shown in Figure 4.8 (left). The background contribution is estimated from one stream of generic MC events in the same mass window ($[138, 180]\,\mathrm{MeV}/c^2$). Signal events are removed from the generic MC sample while the off-resonance data are added to it after a proper scaling. The variation of background events with the criterion on reduced χ^2 is shown in Figure 4.8 (right).

A figure-of-merit (FOM) is calculated as $S/\sqrt{(S+B)}$, where S (B) is the expected signal (background) events. The variation of FOM with the condition on reduced χ^2 is shown in Figure 4.9, where $\chi^2/\mathrm{NDF} < 3$ is found to be the optimal point. The uncertainty on FOM mostly arises from the ratio of the yield of $\chi_{b0}(1P)$ to that of $\chi_{b1}(1P)$ in our signal estimation. The FOM is recalculated by varying the product branching fraction $\pm1\sigma$ around its error [discussed above as the case (b)], and is shown in Figure 4.9. The optimal point remains unchanged at $\chi^2/\mathrm{NDF} < 3$.

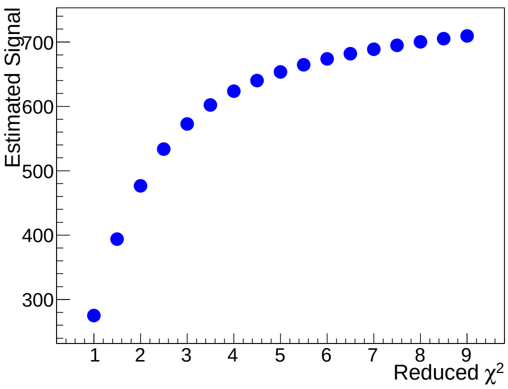

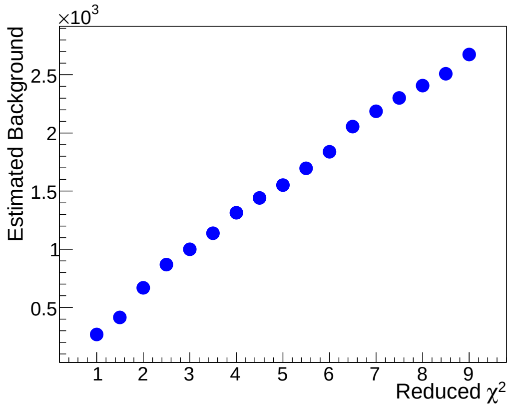

FIGURE 4.8: Variation of expected signal (left) and background (right) events with the applied χ^2/NDF condition.

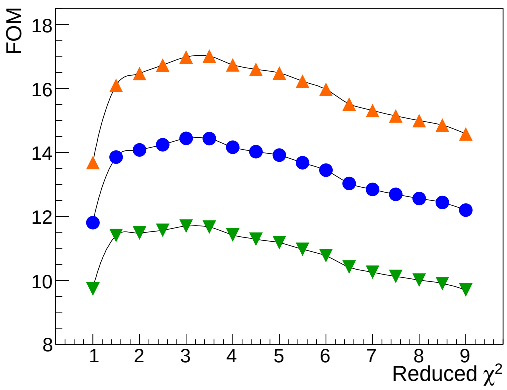

FIGURE 4.9: Variation of the FOM with the condition on reduced χ^2, the optimal point is found at $\chi^2/\text{NDF} < 3$. The FOM is recalculated by varying the product branching fraction by $\pm 1\sigma$ around its error. The curve with upward orange triangles is for the positive variation, the curve with downward green triangles for the negative variation, whereas the curve with blue dots is for no variation. The optimal cut value does not change from $\chi^2/\text{NDF} < 3$.

4.4 Fit and Significant Modes

Significant modes need to be identified for the branching fraction related studies. Fit in data to the ΔM distribution and the method of significant mode selection are discussed in the following subsections.

4.4.1 Maximum Likelihood Fit

To decide the PDF for the signal components, the respective signal MC samples are studied. All three signals shapes are modeled with the sum of a symmetric

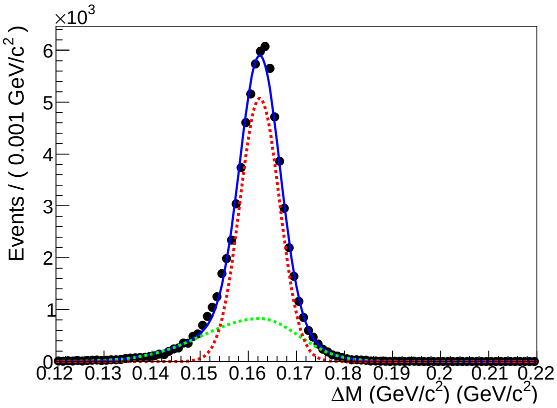

FIGURE 4.10: Fit to the ΔM distribution of the signal MC sample of $\chi_{b0}(1P) \to 2(\pi^+\pi^-)$. Black points with error bars are signal MC events, the solid blue curve is the result of the total fit, the symmetric Gaussian component is shown by the dotted red curve, and the asymmetric Gaussian component of the fit is represented by the dotted green curve.

and an asymmetric Gaussian function. Both the Gaussians have a common mean (an example is shown in Figure 4.10).

The fit range of the ΔM distribution in data is $(40, 240)$ MeV/c^2, which includes the three $\chi_{bJ}(1P)(J = 0, 1, 2)$ signal components. These components, as mentioned earlier, are fitted with the sum of two Gaussians, for which the three widths and the fraction between the two are fixed from fitting MC events of the corresponding signal in all the 74 modes. The parameters for all modes are close, having a small RMS. Thus we fix each parameter to its mean value while the RMS is varied to estimate the assorted systematic uncertainty. In order to account for a modest difference in the detector resolution between data and simulations, we use a fudge factor common to the three signal components. Background is modeled with the sum of an exponential function and a first-order Chebyshev polynomial. The corresponding three parameters (exponent, slope and relative fraction) are allowed to vary in the fit. The fitting procedure is similar to that already discussed and validated in Section 3.3.4.

The fit to the ΔM distributions for the sum of 74 modes in data is shown in Figure 4.11, the χ^2/NDF of the fit is 1.082. Complete fit result is given in Table B.4 of Appendix B.4. The $\chi_{bJ}(1P)$ signal yields are found to be 5 times more than in our previous analysis [78]. The masses of the $\chi_{bJ}(1P)(J = 0, 1, 2)$ states are obtained to be in an excellent agreement with, and more precise than, the world average values [13]. They are listed in Table 4.1 along with their world average values. The calibration factor, which takes into account the data-MC difference

TABLE 4.1: Mass and signal yield of $\chi_{bJ}(1P)$ obtained in this analysis from the sum of 74 reconstrcuted modes.

State	Signal yield	Mass in MeV/c^2 (stat. error only)	Mass in MeV/c^2 (World average [13])
$\chi_{b0}(1P)$	1197 ± 58	9858.98 ± 0.33	$9859.44 \pm 0.42 \pm 0.31$
$\chi_{b1}(1P)$	4747 ± 94	9893.05 ± 0.12	$9892.78 \pm 0.26 \pm 0.31$
$\chi_{b2}(1P)$	3064 ± 87	9911.81 ± 0.16	$9912.21 \pm 0.26 \pm 0.31$

for the resolution is, 1.134 ± 0.019, in a resonable agreement with the usual Belle estimations.

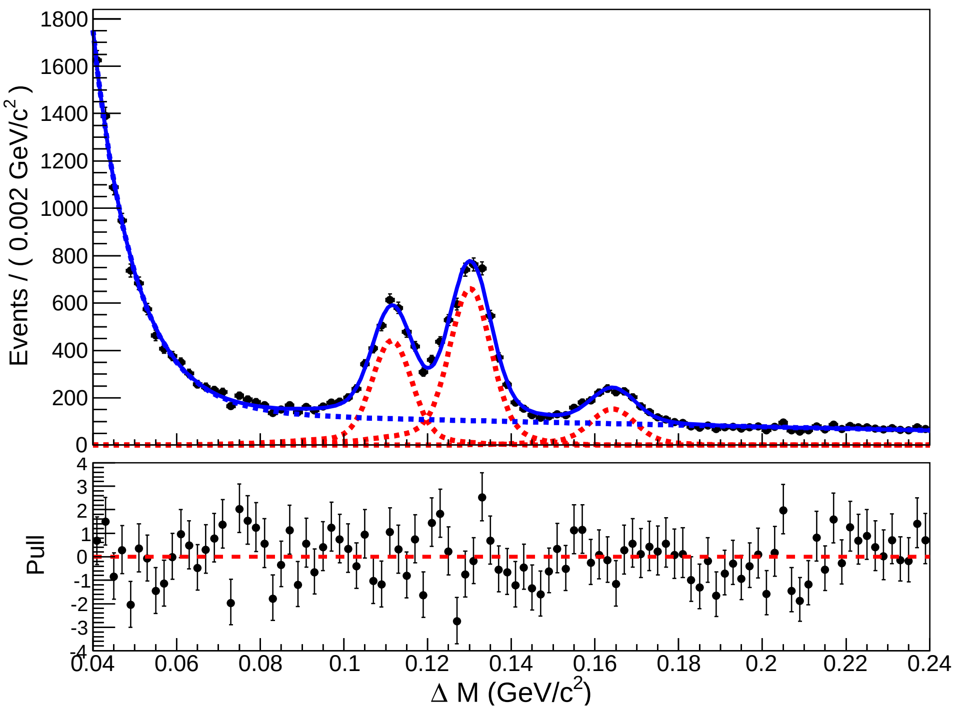

FIGURE 4.11: Fit to the ΔM distribution for $\Delta M \in (0.04, 0.24)$ GeV/c^2 in $\Upsilon(2S)$ on-resonance data from the sum of 74 reconstructed modes. The blue solid and blue dashed curves are the total fit and background components. The three $\chi_{bJ}(1P)$ components are shown by red dashed curves.

4.4.2 Mode Selection

With signal shapes, including the ΔM values, fixed by the fit to the sum of 74 modes (described in Section 3.3.4), the ΔM distribution in each mode is fitted. The signal significance from the fit to each mode is determined as $\sqrt{-2\ln(\mathcal{L}_0/\mathcal{L}_{max})}$, where $\mathcal{L}_0$ and $\mathcal{L}_{max}$ are the likelihood value with the signal yield varied as a free parameter and fixed to 0. Signal significances in all the modes reconstructed are given in Appendix B.5. In total, 41 modes are identified that have at least 5σ significance in any of the $\chi_{bJ}(1P)(J = 0, 1, 2)$ signals. Number of signal events obtained from the fit, corrected efficiency, and the significance for the selected modes are listed in Table 4.2. The ΔM distribution in those 41 selected modes are shown in Figure 4.12.

Table 4.2: Number of $\chi_{bJ}(1P)$ signal events obtained from the fit, the significance and the corrected efficiency for each significant modes. The table continues to the next page.

Modes	χ_{b0}			χ_{b1}			χ_{b2}		
	N	σ	ϵ	N	σ	ϵ	N	σ	ϵ
$2\pi^+2\pi^-$	25.6	3.0	12.7	72.5	6.8	14.6	32.6	3.1	13.6
$3\pi^+3\pi^-$	90.2	11.0	8.6	286.3	23.6	9.8	143.0	12.6	9.4
$4\pi^+4\pi^-$	63.0	8.5	5.1	266.7	22.5	6.0	163.7	14.6	5.7
$5\pi^+5\pi^-$	25.6	4.9	3.1	84.8	10.8	3.5	90.8	10.9	3.3
$\pi^+\pi^-K^+K^-$	25.9	8.1	10.8	33.9	8.6	12.3	27.1	6.3	11.4
$2\pi^+2\pi^-K^+K^-$	59.9	8.7	7.2	157.6	16.3	8.3	96.6	11.5	7.9
$3\pi^+3\pi^-K^+K^-$	42.7	5.8	4.4	132.5	13.7	5.0	89.8	9.8	4.8
$4\pi^+4\pi^-K^+K^-$	45.5	7.9	2.5	71.1	10.5	2.9	66.9	9.6	2.7
$\pi^+\pi^-2K^+2K^-$	16.6	5.4	6.0	38.8	8.6	7.0	33.7	7.4	6.6
$2\pi^+2\pi^-2K^+2K^-$	14.5	4.4	3.5	38.6	7.8	4.1	34.7	7.2	3.9
$3\pi^+3\pi^-2K^+2K^-$	10.2	3.8	1.9	15.4	4.5	2.3	23.8	6.2	2.2
$2\pi^+2\pi^-p\overline{p}$	1.7	0.9	3.8	45	10.2	5.5	13.5	3.5	5.2
$3\pi^+3\pi^-p\overline{p}$	10.2	3.1	2.9	36.5	7.8	3.3	15.3	3.6	3.2
$\pi^+\pi^-K^+K^-p\overline{p}$	10.2	4.2	5.1	17.6	5.7	5.9	13.3	3.7	5.6
$2\pi^+2\pi^-K^+K^-p\overline{p}$	17.3	4.5	3.5	28.3	6.3	4.1	12	3.4	3.8
$\pi^+\pi^-\pi^\pm K^\mp K^0_S$	0.0	0.0	5.5	74.9	12.9	6.4	27.0	5.0	6.1
$2\pi^+2\pi^-\pi^\pm K^\mp K^0_S$	10.6	2.2	3.3	116.2	13.9	3.8	64.3	8.5	3.6
$3\pi^+3\pi^-\pi^\pm K^\mp K^0_S$	10.3	2.1	1.9	55.9	8.9	2.2	24.8	4.3	2.1
$2\pi^+2\pi^-2K^0_S$	8.1	4.2	2.6	13.4	5.4	3.1	13.6	5.2	2.9
$3\pi^+3\pi^-2K^0_S$	5.1	2.2	1.5	14.4	5.0	1.7	11.4	3.8	1.6

Number of $\chi_{bJ}(1P)$ signal events obtained from the fit, the significance, and the corrected efficiency for each selected modes. The table continues from the previous page.

Modes	χ_{b0}			χ_{b1}			χ_{b2}		
	N	σ	ϵ	N	σ	ϵ	N	σ	ϵ
$\pi^+\pi^-K^+K^-\pi^0$	3.3	0.7	6.2	88.0	10.7	7.2	39.0	5.2	6.9
$2\pi^+2\pi^-K^+K^-\pi^0$	45.7	4.5	3.4	261.4	18.3	3.9	170.4	11.8	3.8
$3\pi^+3\pi^-K^+K^-\pi^0$	52.5	5.2	1.8	198.6	14.5	2.1	124.3	9.0	2.0
$4\pi^+4\pi^-K^+K^-\pi^0$	9.3	1.4	0.9	69.2	7.8	1.1	40.0	4.4	1.0
$\pi^+\pi^-2K^+2K^-\pi^0$	12.2	3.2	2.7	46.2	7.9	3.2	22	3.9	3.1
$2\pi^+2\pi^-2K^+2K^-\pi^0$	15.7	3.2	1.4	30.0	5.0	1.7	18.7	3.5	1.6
$\pi^+\pi^-p\overline{p}\pi^0$	0.0	0.0	4.0	17.4	5.4	4.6	9.9	3.3	4.5
$\pi^+\pi^-K^+K^-p\overline{p}\pi^0$	6.8	2.8	2.6	20.9	5.5	2.9	14.3	3.3	2.8
$\pi^+\pi^-\pi^\pm K^\mp K^0_S\pi^0$	8.2	1.5	2.7	110.8	11.9	3.2	55.8	6.1	3.1
$2\pi^+2\pi^-\pi^\pm K^\mp K^0_S\pi^0$	30.9	3.8	1.5	137.0	12.1	1.6	67.1	6.1	1.6
$3\pi^+3\pi^-\pi^\pm K^\mp K^0_S\pi^0$	29.6	4.1	0.8	64.7	7.6	0.9	39.2	4.7	0.9
$2\pi^+2\pi^-2\pi^0$	42.0	3.9	3.4	282.5	16.9	4.0	213.5	12.5	4.0
$3\pi^+3\pi^-2\pi^0$	101.1	6.7	1.8	556.3	24.0	2.1	308.5	13.6	2.0
$4\pi^+4\pi^-2\pi^0$	66.9	5.3	0.9	365.7	19.6	1.0	251.7	13.3	1.0
$5\pi^+5\pi^-2\pi^0$	19.5	2.6	0.4	87.8	8.4	0.5	82.7	7.1	0.5
$\pi^+\pi^-K^+K^-2\pi^0$	24.4	3.3	2.8	57.8	7.0	3.3	47.6	5.4	3.2
$2\pi^+2\pi^-K^+K^-2\pi^0$	39.4	3.9	1.4	129.5	10.0	1.7	89.5	6.8	1.6
$3\pi^+3\pi^-K^+K^-2\pi^0$	35.6	3.6	0.7	114.3	9.4	0.8	77.5	6.3	0.8
$2\pi^+2\pi^-p\overline{p}2\pi^0$	13.3	2.7	0.9	27.6	5.0	1.0	25.3	4.4	1.0
$\pi^+\pi^-\pi^\pm K^\mp K^0_S2\pi^0$	37.3	5.1	1.2	78.2	8.6	1.4	35.7	4.2	1.3
$2\pi^+2\pi^-\pi^\pm K^\mp K^0_S2\pi^0$	27	3.5	0.6	90.8	9.1	0.6	53.1	5.1	0.7

4.4.3 Systematic Error Estimation

The major source of systematic uncertainty is found to be the effect of possible intermediate states (mentioned in Section 4.1) on the signal reconstruction efficiency. The deviation in the efficiency obtained from phase space consideration is found be 2 – 23%. Uncertainties on the signal yield due to PDF shapes are estimated using $\pm1\sigma$ variations of the shape parameters that are fixed in the fit, and are found to be 3 – 12%. The uncertainty due to a limited size of the signal MC sample is 1%. Uncertainties associated with photon detection (3%), charged track reconstruction (0.35% per track), particle identification is (1.5 – 4.5%), K^0_S reconstruction (2.2% per K^0_S), π^0 reconstruction (2.2% per π^0) and number of $\Upsilon(2S)$ in data sample (2.3%) are also taken into account. Systematic errors are added in quadrature mode by mode, and they are in a range of 6 – 27%.

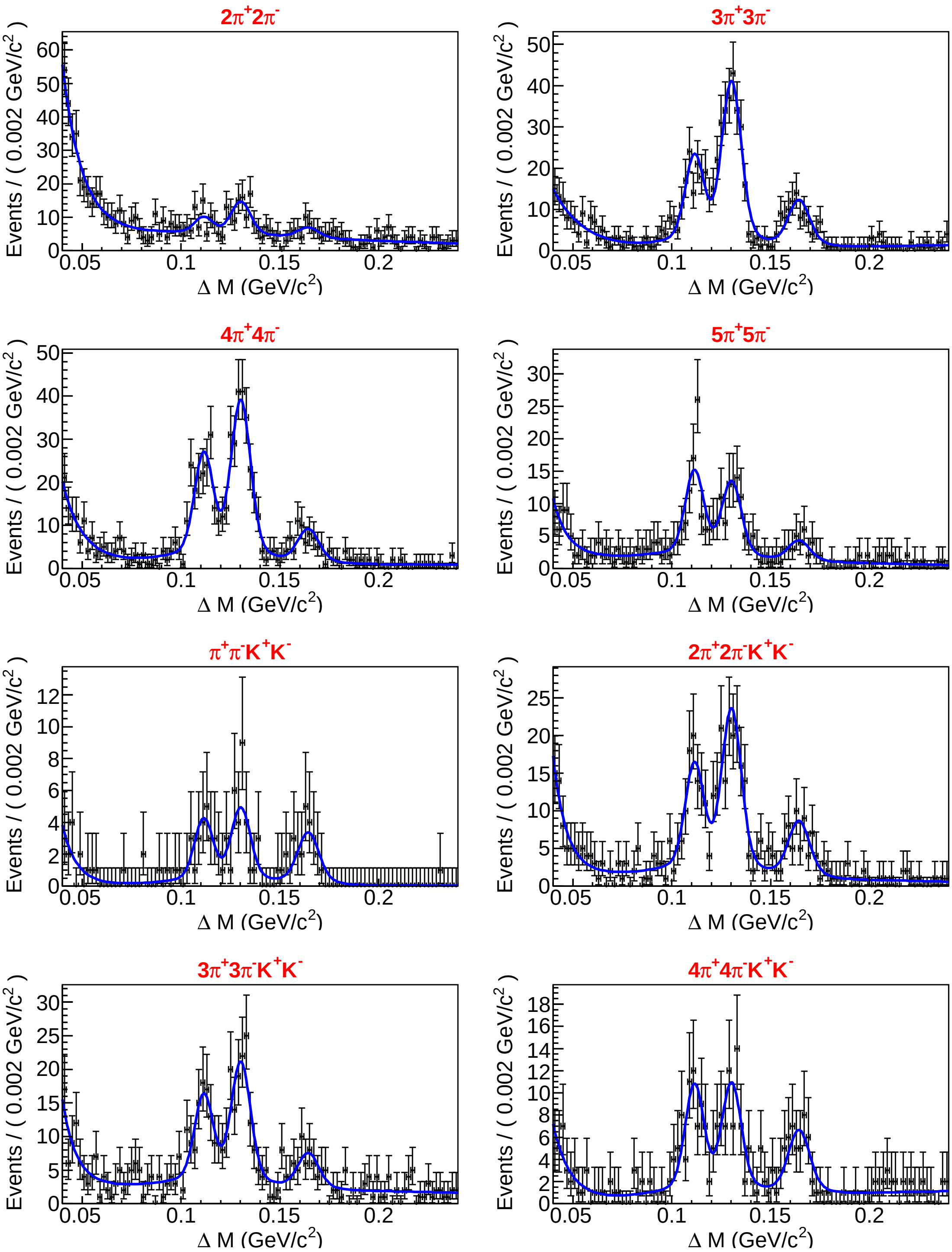

FIGURE 4.12: ΔM distributions in the significant 41 modes. Points with error bars are the data and blue line is the total fit (continued).

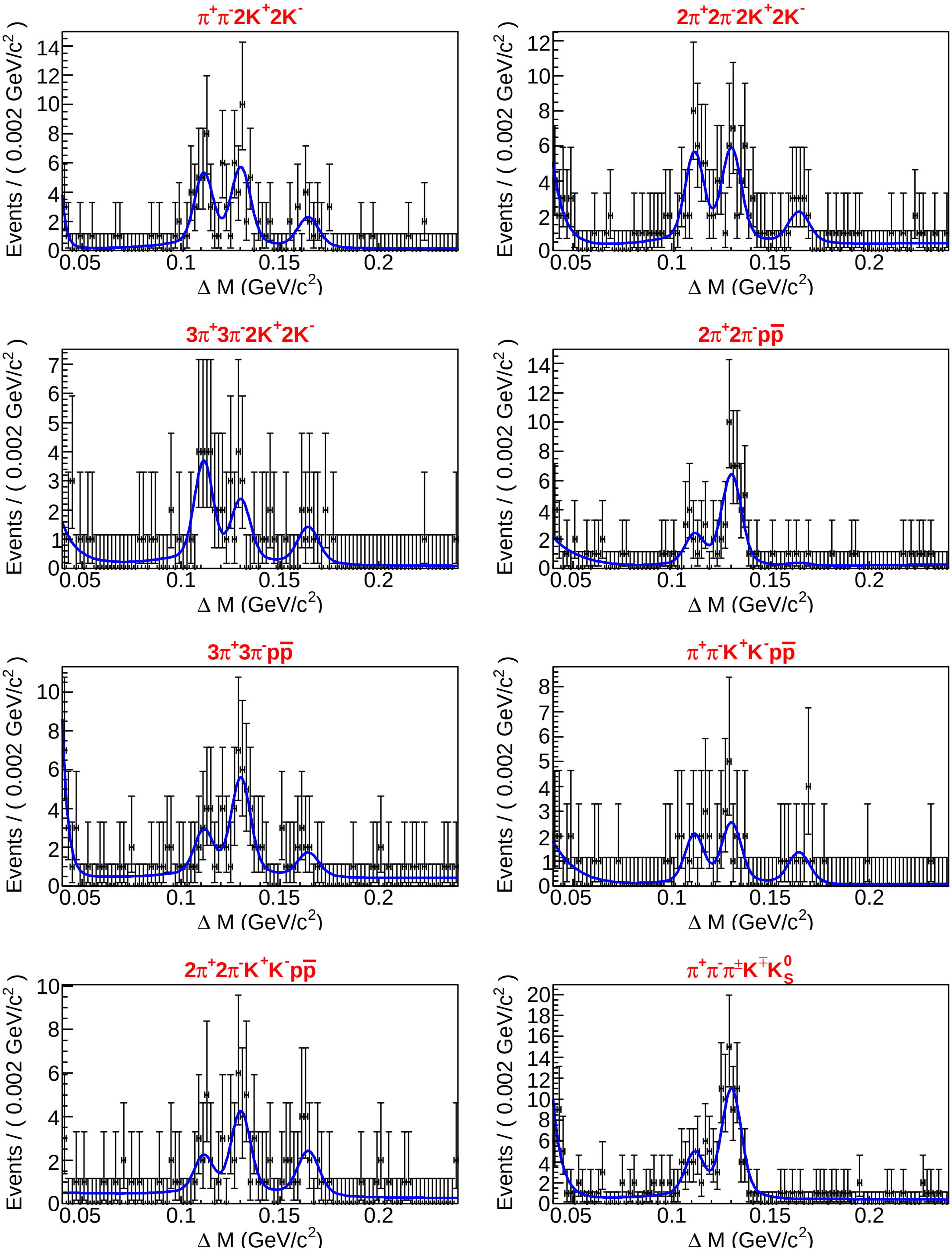

ΔM distributions in the significant 41 modes. Points with error bars are the data and blue line is the total fit (continued).

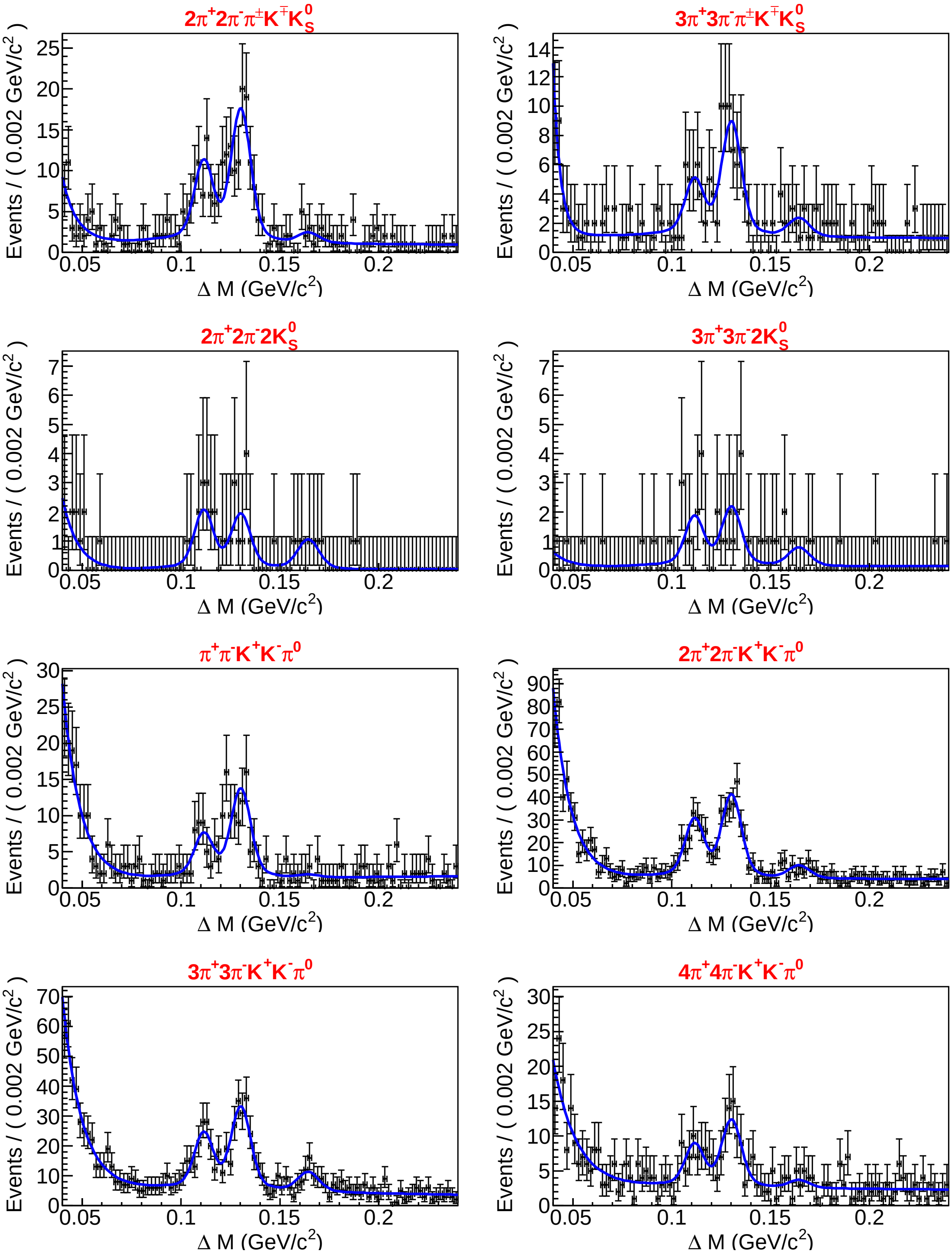

ΔM distributions in the significant 41 modes. Points with error bars are the data and blue line is the total fit (continued).

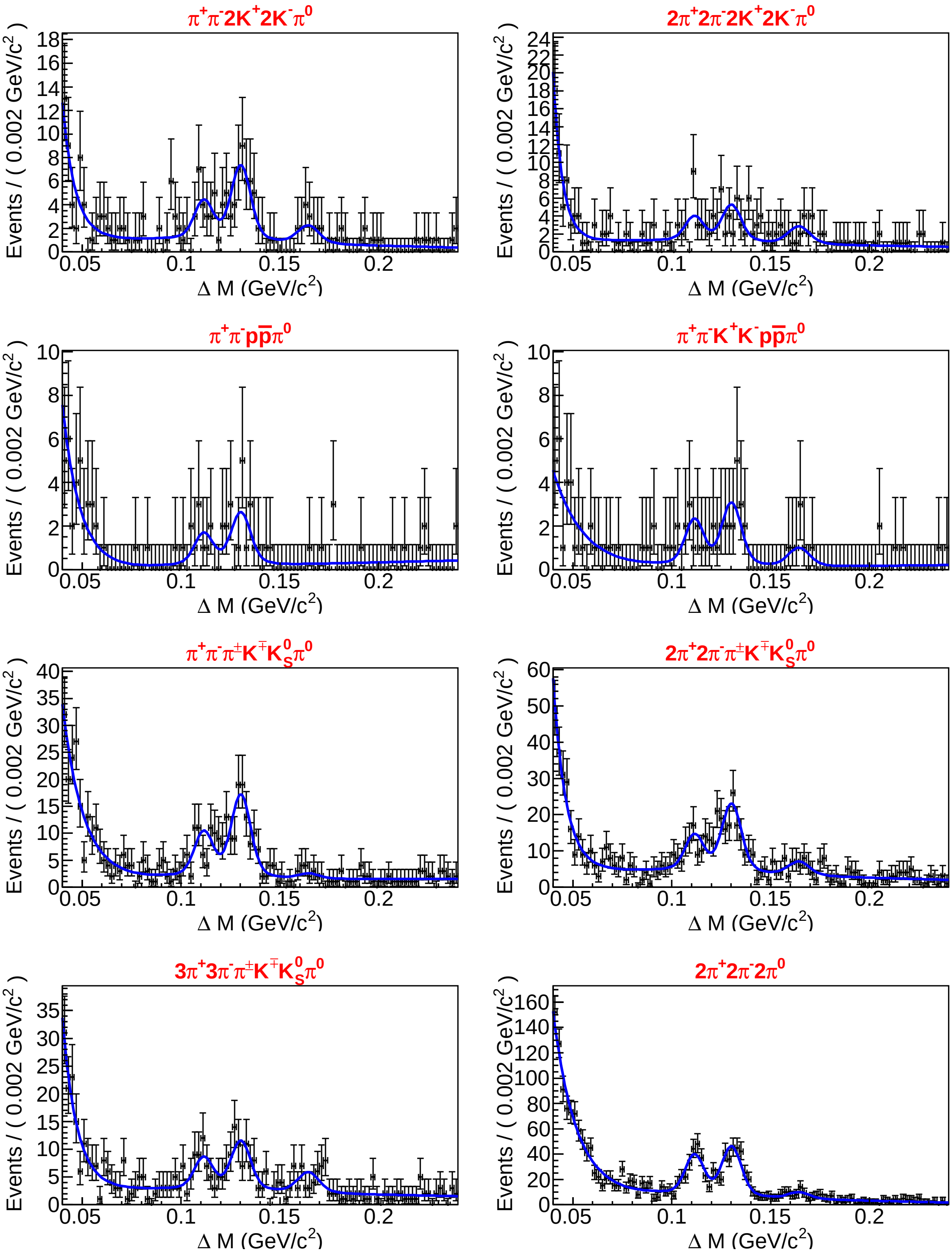

ΔM distributions in the significant 41 modes. Points with error bars are the data and blue line is the total fit (continued).

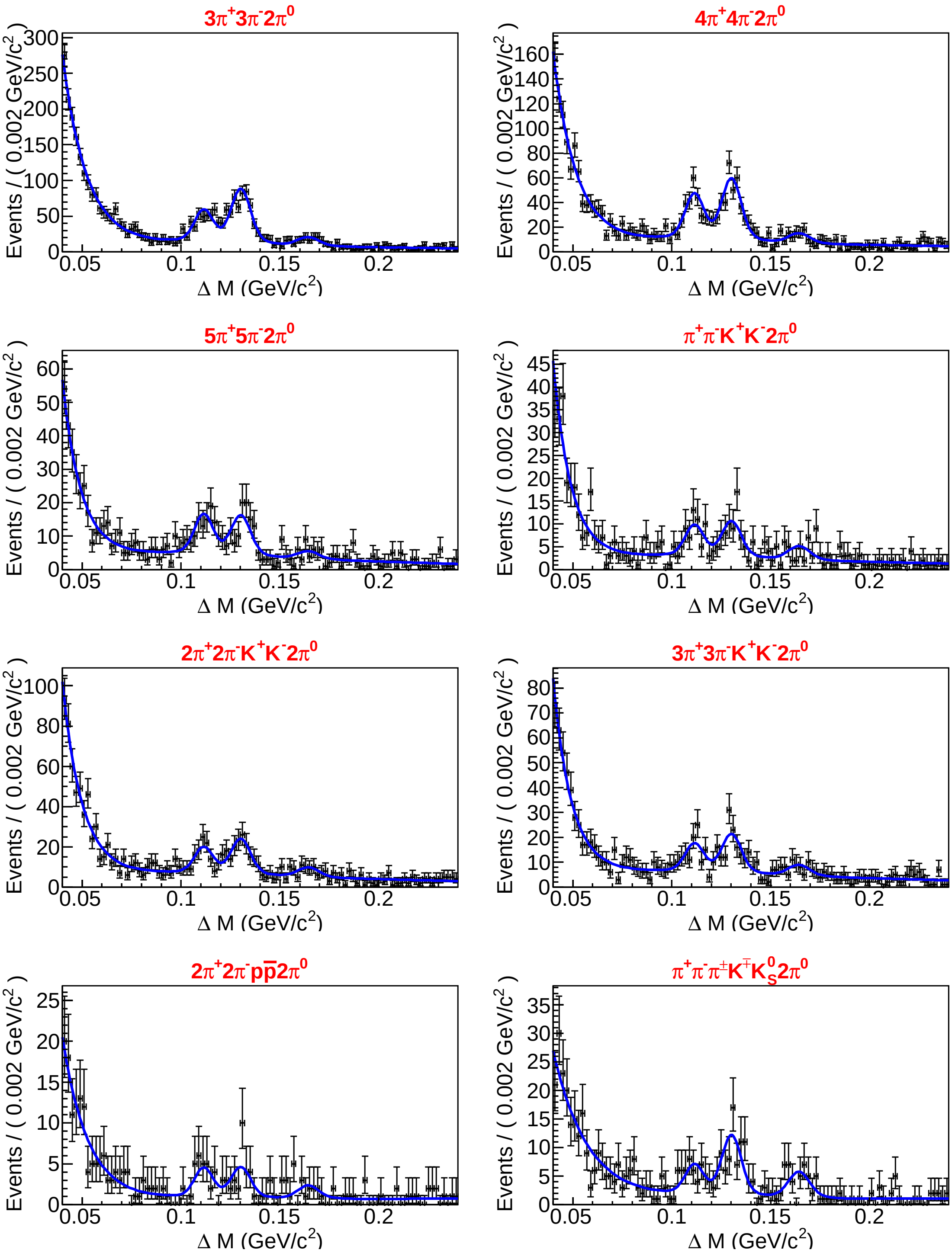

ΔM distributions in the significant 41 modes. Points with error bars are the data and blue line is the total fit (continued).

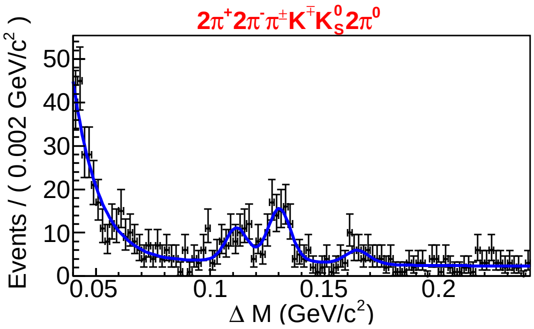

ΔM distributions in the significant 41 modes. Points with error bars are the data and blue line is the total fit.

4.4.4 Branching Fraction Results

The product branching fraction, $\mathcal{B}[\Upsilon(2S) \to \gamma\chi_{bJ}(1P)] \times \mathcal{B}[\chi_{b1}(1P) \to X_i]$, for each $\chi_{bJ}(1P)$ decay where the significance is greater than 3σ, are listed in Table 4.3. The values indicated by a symbol † in the table (in total, 85 of them) are the first observation of the signal in that mode.

TABLE 4.3: Product branching fraction, $\mathcal{B}[\Upsilon(2S) \to \gamma\chi_{bJ}(1P)] \times \mathcal{B}[\chi_{b1}(1P) \to h_i]$, for each $\chi_{bJ}(1P)(J = 0, 1, 2)$ in units of 10^{-5}. Upper limits at the 90% CL are calculated for the modes having a significance less than 3σ. The quoted uncertainties are statistical and systematic, respectively. The table continues to the next page.

Mode	$\chi_{b0}(1P)$	$\chi_{b1}(1P)$	$\chi_{b2}(1P)$
$2\pi^+2\pi^-$	$0.13 \pm 0.05 \pm 0.02$†	$0.3 \pm 0.1 \pm 0.04$†	$0.2 \pm 0.1 \pm 0.02$†
$3\pi^+3\pi^-$	$0.7 \pm 0.1 \pm 0.06$†	$1.8 \pm 0.1 \pm 0.2$	$1 \pm 0.1 \pm 0.1$
$4\pi^+4\pi^-$	$0.8 \pm 0.1 \pm 0.1$†	$2.8 \pm 0.2 \pm 0.4$	$1.8 \pm 0.2 \pm 0.2$
$5\pi^+5\pi^-$	$0.5 \pm 0.1 \pm 0.1$†	$1.5 \pm 0.2 \pm 0.3$†	$1.7 \pm 0.2 \pm 0.3$†
$\pi^+\pi^-K^+K^-$	$0.15 \pm 0.03 \pm 0.03$†	$0.17 \pm 0.03 \pm 0.03$†	$0.15 \pm 0.04 \pm 0.03$†
$2\pi^+2\pi^-K^+K^-$	$0.5 \pm 0.1 \pm 0.1$	$1.2 \pm 0.1 \pm 0.1$	$0.8 \pm 0.1 \pm 0.1$
$3\pi^+3\pi^-K^+K^-$	$0.6 \pm 0.1 \pm 0.1$	$1.7 \pm 0.2 \pm 0.2$	$1.2 \pm 0.2 \pm 0.1$†
$4\pi^+4\pi^-K^+K^-$	$1.2 \pm 0.2 \pm 0.2$†	$1.6 \pm 0.2 \pm 0.2$†	$1.6 \pm 0.2 \pm 0.2$†
$\pi^+\pi^-2K^+2K^-$	$0.18 \pm 0.05 \pm 0.02$†	$0.4 \pm 0.1 \pm 0.03$†	$0.3 \pm 0.1 \pm 0.03$†
$2\pi^+2\pi^-2K^+2K^-$	$0.3 \pm 0.1 \pm 0.03$†	$0.6 \pm 0.1 \pm 0.1$†	$0.6 \pm 0.1 \pm 0.1$†
$3\pi^+3\pi^-2K^+2K^-$	$0.3 \pm 0.1 \pm 0.1$†	$0.4 \pm 0.1 \pm 0.1$†	$0.7 \pm 0.2 \pm 0.1$†
$2\pi^+2\pi^-p\bar{p}$	< 0.2	$0.5 \pm 0.1 \pm 0.1$†	$0.2 \pm 0.1 \pm 0.03$†
$3\pi^+3\pi^-p\bar{p}$	$0.2 \pm 0.1 \pm 0.03$†	$0.7 \pm 0.1 \pm 0.1$†	$0.3 \pm 0.1 \pm 0.04$†
$\pi^+\pi^-K^+K^-p\bar{p}$	$0.13 \pm 0.04 \pm 0.02$†	$0.2 \pm 0.1 \pm 0.03$†	$0.2 \pm 0.1 \pm 0.03$†
$2\pi^+2\pi^-K^+K^-p\bar{p}$	$0.3 \pm 0.1 \pm 0.1$†	$0.4 \pm 0.1 \pm 0.1$†	$0.2 \pm 0.1 \pm 0.03$†

Product branching fraction, $\mathcal{B}[\Upsilon(2S) \to \gamma\chi_{bJ}(1P)] \times \mathcal{B}[\chi_{b1}(1P) \to h_i]$, for each $\chi_{bJ}(1P)(J = 0, 1, 2)$ in units of 10^{-5}. Upper limits at the 90% CL are calculated for the modes having a significance less than 3σ. The quoted uncertainties are statistical and systematic, respectively. The table continues from the previous page.

Mode	$\chi_{b0}(1P)$	$\chi_{b1}(1P)$	$\chi_{b2}(1P)$
$\pi^+\pi^-\pi^\pm K^\mp K^0_S$	< 0.1	$0.7 \pm 0.1 \pm 0.1$	$0.3 \pm 0.1 \pm 0.1\dagger$
$2\pi^+2\pi^-\pi^\pm K^\mp K^0_S$	< 0.4	$1.9 \pm 0.2 \pm 0.2\dagger$	$1.1 \pm 0.2 \pm 0.1\dagger$
$3\pi^+3\pi^-\pi^\pm K^\mp K^0_S$	< 0.7	$1.6 \pm 0.3 \pm 0.1\dagger$	$0.8 \pm 0.2 \pm 0.1\dagger$
$2\pi^+2\pi^-2K^0_S$	$0.2 \pm 0.1 \pm 0.04\dagger$	$0.3 \pm 0.1 \pm 0.03\dagger$	$0.3 \pm 0.1 \pm 0.03\dagger$
$3\pi^+3\pi^-2K^0_S$	< 0.6	$0.5 \pm 0.2 \pm 0.1\dagger$	$0.4 \pm 0.2 \pm 0.1\dagger$
$\pi^+\pi^-K^+K^-\pi^0$	< 0.2	$0.8 \pm 0.1 \pm 0.1$	$0.4 \pm 0.1 \pm 0.04$
$2\pi^+2\pi^-K^+K^-\pi^0$	$0.8 \pm 0.2 \pm 0.2\dagger$	$4.2 \pm 0.3 \pm 0.7$	$2.8 \pm 0.3 \pm 0.5$
$3\pi^+3\pi^-K^+K^-\pi^0$	$1.8 \pm 0.4 \pm 0.4\dagger$	$6.0 \pm 0.6 \pm 1.1$	$3.8 \pm 0.5 \pm 0.7$
$4\pi^+4\pi^-K^+K^-\pi^0$	< 1.7	$4.0 \pm 0.7 \pm 1.0\dagger$	$2.4 \pm 0.6 \pm 0.6\dagger$
$\pi^+\pi^-2K^+2K^-\pi^0$	$0.3 \pm 0.1 \pm 0.1\dagger$	$0.9 \pm 0.2 \pm 0.2\dagger$	$0.5 \pm 0.1 \pm 0.1\dagger$
$2\pi^+2\pi^-2K^+2K^-\pi^0$	$0.7 \pm 0.3 \pm 0.1\dagger$	$1.1 \pm 0.3 \pm 0.2\dagger$	$0.7 \pm 0.3 \pm 0.1\dagger$
$\pi^+\pi^-p\overline{p}\pi^0$	< 0.1	$0.2 \pm 0.1 \pm 0.04\dagger$	$0.1 \pm 0.1 \pm 0.02\dagger$
$\pi^+\pi^-K^+K^-p\overline{p}\pi^0$	< 0.5	$0.5 \pm 0.1 \pm 0.2\dagger$	$0.3 \pm 0.1 \pm 0.1\dagger$
$\pi^+\pi^-\pi^\pm K^\mp K^0_S\pi^0$	< 0.5	$2.2 \pm 0.3 \pm 0.2\dagger$	$1.2 \pm 0.2 \pm 0.2\dagger$
$2\pi^+2\pi^-\pi^\pm K^\mp K^0_S\pi^0$	$1.3 \pm 0.4 \pm 0.2\dagger$	$5.3 \pm 0.6 \pm 0.8$	$2.6 \pm 0.5 \pm 0.5\dagger$
$3\pi^+3\pi^-\pi^\pm K^\mp K^0_S\pi^0$	$2.4 \pm 0.7 \pm 0.5\dagger$	$4.6 \pm 0.8 \pm 1.0\dagger$	$2.9 \pm 0.7 \pm 0.6\dagger$
$2\pi^+2\pi^-2\pi^0$	$0.8 \pm 0.2 \pm 0.2\dagger$	$4.5 \pm 0.4 \pm 1.0$	$3.4 \pm 0.3 \pm 0.8$
$3\pi^+3\pi^-2\pi^0$	$3.6 \pm 0.6 \pm 0.5\dagger$	$16.8 \pm 0.9 \pm 2.3$	$9.7 \pm 0.9 \pm 1.5$
$4\pi^+4\pi^-2\pi^0$	$4.8 \pm 1.0 \pm 1.0\dagger$	$22.3 \pm 1.5 \pm 4.7$	$15.5 \pm 1.5 \pm 3.3$
$5\pi^+5\pi^-2\pi^0$	< 5.1	$10.8 \pm 1.6 \pm 2.4\dagger$	$11 \pm 1.9 \pm 2.5\dagger$
$\pi^+\pi^-K^+K^-2\pi^0$	$0.5 \pm 0.2 \pm 0.1\dagger$	$1.1 \pm 0.2 \pm 0.3\dagger$	$0.9 \pm 0.2 \pm 0.2\dagger$
$2\pi^+2\pi^-K^+K^-2\pi^0$	$1.7 \pm 0.5 \pm 0.4\dagger$	$4.9 \pm 0.6 \pm 1.1$	$3.5 \pm 0.6 \pm 0.8$
$3\pi^+3\pi^-K^+K^-2\pi^0$	$3.2 \pm 1.0 \pm 0.8\dagger$	$8.9 \pm 1.2 \pm 2.2\dagger$	$6.4 \pm 1.2 \pm 1.6\dagger$
$2\pi^+2\pi^-p\overline{p}2\pi^0$	< 1.8	$1.8 \pm 0.5 \pm 0.3\dagger$	$1.6 \pm 0.5 \pm 0.3\dagger$
$\pi^+\pi^-\pi^\pm K^\mp K^0_S2\pi^0$	$2 \pm 0.5 \pm 0.3\dagger$	$3.6 \pm 0.5 \pm 0.4\dagger$	$1.7 \pm 0.5 \pm 0.2$
$2\pi^+2\pi^-\pi^\pm K^\mp K^0_S2\pi^0$	$3 \pm 1.0 \pm 0.6\dagger$	$9.0 \pm 1.3 \pm 1.7\dagger$	$5.1 \pm 1.2 \pm 1.0\dagger$

Our branching fraction results are consistent with, and more precise than, the ones observed in CLEO's analysis. Futhermore, a $\chi_{bJ}(1P)$ signal for $J = 0, 1$ and 2 has been observed for the first time in 27, 28 and 30 modes, respectively.

CHAPTER 5

Epilogue

The first evidence for bottomonium was found in the di-muon spectrum at Fermilab in 1977 (3 years after the famous November revolution of particle physics started with the discovery of charmonium). Recently many new discoveries in bottomonia have made it a hot topic. Notable among them is the observation of the P-wave spin-singlet bottomonium states $h_b(1P)$ and $h_b(2P)$ by the Belle experiment at KEK [28]. This subsequently led to the discovery of $Z_b^{\pm}$, an exotic state[1], and also opened a new window to access $\eta_b(1S)$ (the ground state of botttomonium) as well as $\eta_b(2S)$ states via radiative transitions [32]. Belle confirmed the $\eta_b(1S)$ at a mass $9402.4 \pm 1.5 \pm 1.8$ MeV/c^2, which is most precise measurement till date, and measured its width $10.8^{+4.0+4.5}_{-3.7-2.0}$ MeV for the first time. In the same analysis, the $\eta_b(2S)$ meson is also discovered at $9974.6 \pm 2.3(\text{stat.}) \pm 2.1(\text{syst.})$ MeV/c^2. These S-wave spin singlet states allow one to obtain the hyperfine splitting from their spin triplet $\Upsilon(nS)$ counterparts, $\Delta M_{HF}(nS) = M[\Upsilon(nS)] - M[\eta_b(nS)]$, which provide an important piece of information about spin-spin interactions between the quark and antiquark. Hyperfine splittings for the $1S$ and $2S$ states are found to be $57.9 \pm 2.3\,\text{MeV}/c^2$ and $24.3^{+4.0}_{-4.5}\,\text{MeV}/c^2$, respectively. However, there is a recent claim [35] of observation of a bottomonium state $X_{b\bar{b}}(9975)$ in the radiative decay $\Upsilon(2S) \to X_{b\bar{b}}(9975)\gamma$ with a data sample of 9.3×10^6 $\Upsilon(2S)$ decays recorded by the CLEO detector. The analysis, based on the reconstruction of 26 exclusive hadronic final states, reports a mass of $9974.6 \pm 2.3 \pm 2.1\,\text{MeV}/c^2$ and assigns this state to the $\eta_b(2S)$, which corresponds to $\Delta M_{\text{HF}}(2S) = 48.6 \pm 3.1\,\text{MeV}/c^2$. This disagrees with most of the predictions for $\Delta M_{\text{HF}}(2S)$ from unquenched lattice calculations, potential models and a model-independent relation that are compiled in Ref. [36],

[1] These states are non-standard hadrons, containing at least four quarks.

and therefore suggests a flaw in the theoretical understanding of QCD hyperfine mass splittings. In contrast, the Belle result [32] is consistent with theoretical expectations.

5.1 Search for $X_{b\bar{b}}(9975)$

We have searched for the $X_{b\bar{b}}(9975)$ state in the data set recorded at the $\Upsilon(2S)$ resonance by the Belle detector, which is also world's largest e^+e^- collision data at that energy [78]. The search is performed in the radiative decay $\Upsilon(2S) \to \gamma(b\bar{b})$, where the $(b\bar{b})$ states are reconstructed from the same 26 modes mentioned in Ref [35]. In Figure 5.1, we present a fit to the $\Delta M \equiv M[(b\bar{b})\gamma] - M(b\bar{b})$ distributions for the sum of the 26 modes. The results of the fit show no evidence of an $X_{b\bar{b}}(9975)$ signal, with a yield of -30 ± 19 events. Our analysis procedure is described in Chapter 2.

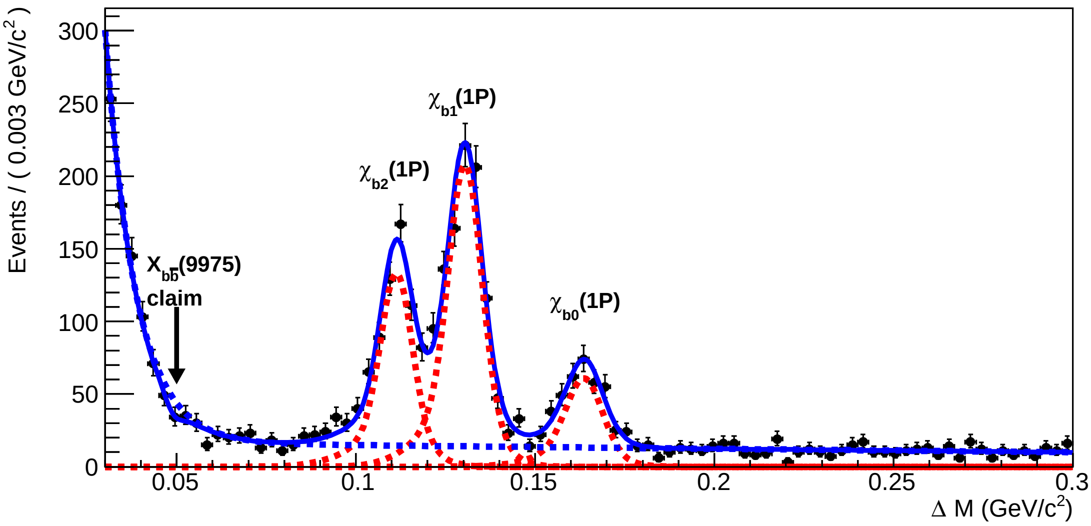

FIGURE 5.1: ΔM distributions and fit for a $\Upsilon(2S)$ data events.

A 90% CL upper limit is determined on the product branching fraction $\mathcal{B}[\Upsilon(2S) \to X_{b\bar{b}}(9975)\gamma] \times \sum_i \mathcal{B}[X_{b\bar{b}}(9975) \to h_i] < 4.9 \times 10^{-6}$, which is an order of magnitude smaller than that reported in Ref. [35]. We have also searched for the $\eta_b(1S)$ state and set an upper limit $\mathcal{B}[\Upsilon(2S) \to \eta_b(1S)\gamma] \times \sum_i \mathcal{B}[\eta_b(1S) \to h_i] < 3.7 \times 10^{-6}$ at 90% CL. The disconfirmation of the $X_{b\bar{b}}(9975)$ state was extremely important as its claim to be the $\eta_b(2S)$ was in disagreement with theory predictions and the Belle result.

5.2 Hadronic Decays of $\chi_{bJ}(1P)$ Triplets

In our previous analysis, we observed large signal yields of 300, 950, and 580 events for $J = 0$, 1, and 2, respectively for the $\chi_{bJ}(1P)$ from the sum of 26 hadronic decay modes. This motivated us further to study the product branching fractions of $\mathcal{B}[\Upsilon(2S) \to \gamma\chi_{bJ}(1P)] \times \mathcal{B}[\chi_{bJ}(1P) \to h_i]$, as the decay of $\chi_{bJ}(1P)$ into states of light-quark hadrons tells us how initial quarks and gluons turn into observable hadrons [27]. For this analysis, we have reconstructed in total of 74 hadronic modes comprising charged pions and kaons, protons, K_S^0 and neutral pions. Signal yields for the $\chi_{bJ}(1P)$ (1200, 4750, and 3050 events for J=0, 1, and 2, respectively) found in this analysis is almost 5 times than our earlier analysis. The analysis procedure is discussed in Chapter 4. In total, 41 modes are identified that have at least 5σ significance in any of the $\chi_{bJ}(1P)(J = 0, 1, 2)$ signals. Our measurement not only improved the previous measurements by the CLEO Collaboration [25] but also led to first observations in many (in total 85) new modes.

5.3 Future Scope and Other Works

Various theoretical calculations for the $\chi_{b0}(1P)$ and $\chi_{b2}(1P)$ widths are summarised in Table 1.3. These calculations predicts that the width of the $\chi_{b0}(1P)$ width can be as large as 2 MeV. With the large statistics of the $\chi_{bJ}(1P)$ signals in our sample we can attempt to measure the width of $\chi_{b0}(1P)$, cross-checks performed regarding this is discussed in Appendix B.6.

Though this thesis is largely focused on the physics analysis of Belle data, as a collaborator of the Belle II experiment I have also participated in the assembly of the layer-4 of its silicon vertex detector, where my task was to perform and optimize gluing operations between the pitch adapters and silicon sensors. A brief description of this work is given in Appendix A.

APPENDIX A

Silicon Vertex Detector for Belle II

Based on a successful operation of the KEKB collider and Belle detector, an upgradation of the accelerator complex (SuperKEKB) leading to an ultimate luminosity of $8 \times 10^{35}\mathrm{cm}^{-2}\mathrm{s}^{-1}$ is currently ongoing, in order to measure mainly rare decays in B and D meson system with higher statistics. To cope up with this 40-fold increase in luminosity, a detector upgrade (Belle II) is also taking place. The Belle II detector is a general purpose magnetic spectrometer comprising the following sub-detector components [79]:

- Two layers of pixelated silicon sensors (PXD) and four layers of double-sided silicon microstrip sensors (SVD) aimed to measure the decay vertex position of short lived particles in particular B mesons.
- A central drift chamber (CDC) for measuring charged particle trajectories, their momenta and specific ionization (dE/dx).
- A barrel-shaped array of time-of-propagation (TOP) counters that reconstructs, in spatial and time coordinates, the ring-image of Cerenkov light emitted from charged particles passing through quartz radiator bars, and another ring-imaging Cerenkov counters with aerogel radiator (ARICH) in the forward endcap, as particle identification devices, especially to distinguish between charged pion and kaons.
- An electromagnetic calorimeter (ECL) composed of CsI(Tl) crystals.
- All the above subdetectors are located inside a superconducting solenoid coil that provides a 1.5 T magnetic field.

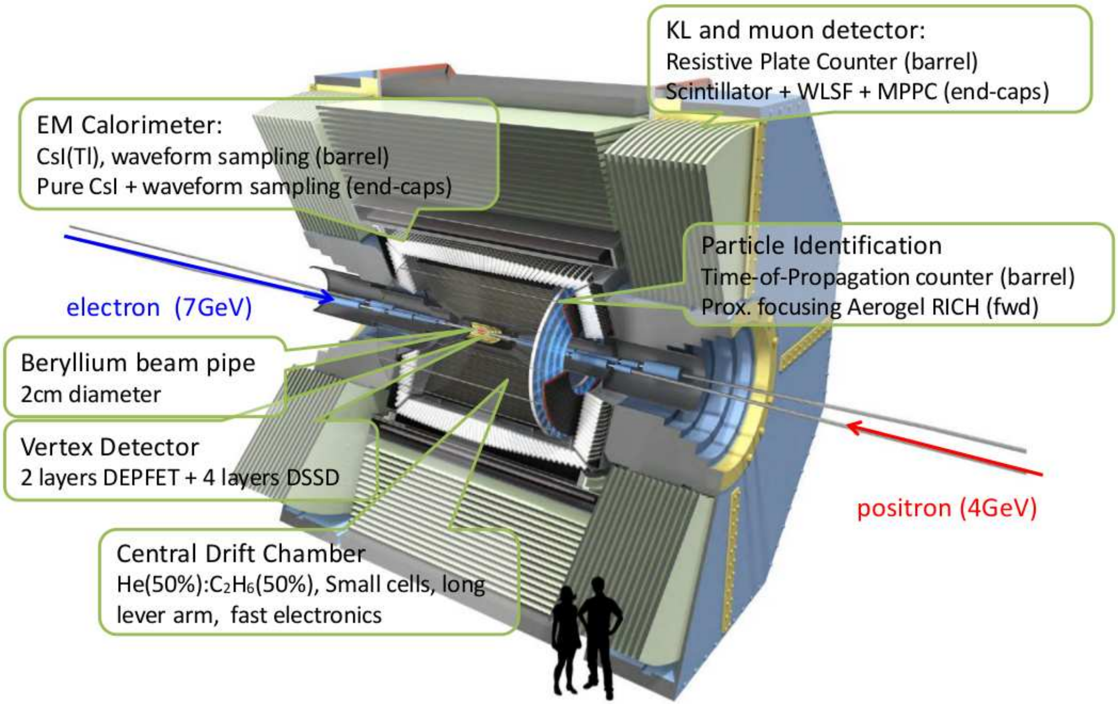

Figure A.1: Schematic of the Belle II detector [79].

- An iron flux-return located outside of the magnet coil which is instrumented with RPCs (plastic scintillators) in the barrel (end-caps) region to detect K_L^0 mesons and muons (KLM).

A three-dimensional schematic view of the upcoming Belle II detector with various sub-detectors is shown in Figure A.1.

As a Belle-II collaborator, I have been fortunate to participate in the assembly of the layer-4 (L4) of its SVD. My major task was to perform and optimize gluing operations between the pitch adapter and silicon sensors. Apart from that, I was also involved in aligning sensors during module assembly with a precision three-dimensional coordinate measuring machine. The Belle II SVD is discussed in Section A.1 while my work is summarised in Section A.2.

A.1 The Belle II SVD

The vertex detector of the Belle described in Section 2.2.3 cannot cope with the 40-fold increase in luminosity and thus an upgrade is absolutely necessary. The new vertex detector for Belle II consists of two layers of the silicon pixel detectors

(PXD) surrounding the beam pipe (described in Ref. [80]) followed by four layers of double-sided silicon microstrip detectors (SVD) [81]. Each layer is composed of several ladders that are an assembly of a number of silicon sensors; Table A.1 lists the specification of the four SVD layers and a schematic of the SVD is shown in Figure A.2. The readout electronics should be faster than before to cope with the luminosity increase and to maintain manageable levels of occupancy and pile-up. Hence, a chip-on-sensor ('origami') scheme [82] is developed to minimize the distance between strips and readout amplifier (thereby reducing the electronic noise) as well as the overall material budget.

TABLE A.1: Layer configuration of the Belle II SVD [81].

Layer	Radius (mm)	Ladders	Sensors per ladder
L3	38	7	2
L4	80	10	3
L5	104	12	4
L6	135	16	5

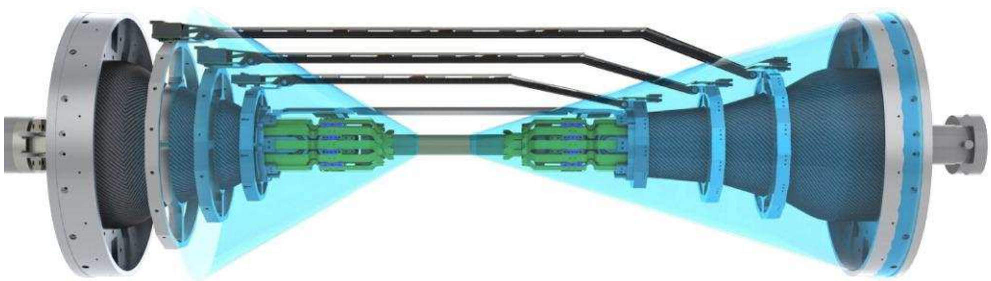

FIGURE A.2: Schematic of the SVD with transparent cones indicating the borders of its angular coverage. In each layer, a single ladder is shown for representation [81].

A.2 L4 Gluing Related Work

For gluing various components of the SVD, Araldite 2011/2012 glue is used, which is a two component epoxy paste adhesive. The two components are mixed by attaching a glue mixer to the cartridge and squeezed till the mixture comes out of the mixer orifice. Required amount of mixed glue is carefully put inside a syringe with stopper. Then the syringe with glue is placed in a centrifuge defoaming machine in proper position inside a syringe holder. The glue is centrifuged for 400s, which removes any air bubbles formed during the glue mixing or while transferring the glue inside the syringe. The stopper from the syringe is replaced with a needle of appropriate diameter (0.25 mm - 1.06 mm) specified for the gluing different components. An air-pump line is attached to the syringe, which brings glue out for the desired application through the needle by applying pressure (2-4 bar). For a specific glue pattern, a glue robot (Cast PRO II SONY) is used. For this the syringe is clamped at the designated position on the glue robot and later calibrated by looking at attached microscopes. A photograph of this procedure can be seen in Figure A.3.

FIGURE A.3: Initial position of the needle of the syringe being calibrated before start of the operation of gluing pattern programs.

The component on which glue to be applied should be properly cleaned and carefully fixed to the platform (vacuum chuck) of the glue robot beforehand. The values of needle diameter, gas pressure, and several other parameters are optimized for different purposes (and it can be found in an internal webpage [83]).

APPENDIX B

Supplementary Informations

B.1 MC generation

For simulating the radiative decay $\Upsilon(2S) \to \gamma(b\bar{b})$, the `HELAMP` [67, 68] model of the `EvtGen` [63] package is used by specifying helicity amplitudes of final state particles in the input decay table, as follows:

1. For the decay $\Upsilon(2S) \to \gamma\chi_{b0}(1P)$:
   ```
   Decay Upsilon(2S)
   1.0000 gamma chi_b0       HELAMP 1.0 0.0 1.0 0.0;
   Enddecay
   ```
2. For the decay $\Upsilon(2S) \to \gamma\chi_{b1}(1P)$:
   ```
   Decay Upsilon(2S)
   1.0000 gamma chi_b1       HELAMP 1.0 0.0  1.0 0.0  -1.0 0.0  -1.0
   0.;
   Enddecay
   ```
3. For the decay $\Upsilon(2S) \to \gamma\chi_{b2}(1P)$:
   ```
   Decay Upsilon(2S)
   1.0000 gamma chi_b2       HELAMP 2.4494897 0.  1.7320508 0.  1.  0.
   1.  0.  1.7320508 0.  2.4494897 0.;
   Enddecay
   ```
4. For the decay $\Upsilon(2S) \to \gamma\eta_b(1S)$:
   ```
   Decay Upsilon(2S)
   ```

```
1.0000 gamma eta_b       HELAMP 1.0 0.0 1.0 0.0;
Enddecay
```

5. For the decay $\Upsilon(2S) \to \gamma X_{b\bar{b}}(9975)$:

```
Decay Upsilon(2S)
1.0000 gamma eta_b(2S)       HELAMP 1.0 0.0 1.0 0.0;
Enddecay
```

Properties of the signals generated are described in Table B.1

Table B.1: Properties of signals generated in MC samples.

Signal	ID	Mass (GeV/c^2)	Width(MeV)	Spin
$\Upsilon(2S)$	100553	10.02326	0.044	1
$X_{b\bar{b}}(9975)[\eta_b(2S)]$[a]	100551	9.974	0	0
$\chi_{b2}(1P)$	555	9.9126	0	2
$\chi_{b1}(1P)$	20553	9.8927	0	1
$\chi_{b0}(1P)$	10551	9.8599	0	0
$\eta_b(1S)$	551	9.403	10[b]	0

[a] $X_{b\bar{b}}(9975)$ signal properties generated as $\eta_b(2S)$, except its mass as measured by Belle [32].

[b] signal with zero width is also generated for measuring detector resolution.

The Generic decay of $\Upsilon(2S)$ is simulated as follows:

```
Decay Upsilon(2S)
0.0192   e+     e-     PHOTOS  VLL;
0.0192   mu+    mu-    PHOTOS  VLL;
0.0200   tau+   tau-   PHOTOS  VLL;
0.1880   Upsilon    pi+   pi-     PHOTOS PHSP;
0.0900   Upsilon    pi0   pi0     PHSP;
# V-> gamma S Partial wave (L,S)=(0,1)
0.0380   gamma    chi_b0   HELAMP 1.0 0.0 1.0 0.0;
# V-> gamma V Partial wave (L,S)=(0,1)
0.0690   gamma    chi_b1   HELAMP 1.0 0.0 1.0 0.0 -1.0 0.0 -1.0 0.;
# V-> gamma T Partial wave (L,S)=(0,1)
0.0715   gamma    chi_b2   HELAMP 2.4494897 0.  1.7320508 0.  1.  0.  1.
0.  1.7320508 0.  2.4494897 0.;
0.0050   d      anti-d  PHOTOS PYTHIA 32;
0.0200   u      anti-u  PHOTOS PYTHIA 32;
```

```
0.0050   s     anti-s  PHOTOS PYTHIA 32;
0.0200   c     anti-c  PHOTOS PYTHIA 32;
0.4191   g     g   g   PHOTOS PYTHIA 4;
0.0160   gamma g   g   PHOTOS PYTHIA 4;
Enddecay;
```

The $\chi_{bJ}(1P)$ decay is simulated in generic MC as follows (as given in Belle `evt.pdl`):

```
Decay chi_b0
# S-> gamma V Partial wave (L,S)=(0,0)
0.0500 gamma Upsilon HELAMP 1.  0.  1.  0.;
0.9500 rndmflav anti-rndmflav PHOTOS PYTHIA 12;
Enddecay;
#
Decay chi_b1
# V-> gamma V Partial wave (L,S)=(0,1)
0.3500 gamma Upsilon HELAMP 1.  0.  1.  0.  -1.  0.  -1.  0.;
0.6500 g g PHOTOS PYTHIA 32;
Enddecay;
#
Decay chi_b2
# T-> gamma V Partial wave (L,S)=(0,2) Use PHSP.
0.2200 gamma Upsilon PHSP;
#0.2200 gamma Upsilon HELAMP 1.  0.  1.7320508 0.  2.4494897 0.
# 2.4494897 0.  1.7320508 0.  1.  0.;
0.7800 g g PHOTOS PYTHIA 32;
Enddecay;
```

B.2 `HELAMP` Model Verification

`HELAMP` model allows generation of two-body decays according to the helicity amplitude formalism. The parameters of this model used for generating the signal MC sample are summarised in Appendix B.1. To verify this model, we fit the ΔM distribution of the $\Upsilon(2S)$ on-resonance data in bins of the photon helicity angle and obtain the signal yield for each bin. The signal yield is normalised by dividing its value in each bin by the total yield for each signal $\chi_{bJ}(1P)(J = 0, 1, 2)$ case. Using signal MC events, the efficiency is obtained for each bin of the photon helicity angle and normalised by dividing it by the total efficiency. In Figure B.1, a comparison between the data and signal MC expectation is shown. As an example, the signal MC sample used here is $\Upsilon(2S) \to \gamma\chi_{bJ}(1P)(J = 0, 1, 2)$ with $\chi_{bJ}(1P)(J = 0, 1, 2) \to 3\pi^+3\pi^-$. The data and generated MC samples are found to be in good agreement.

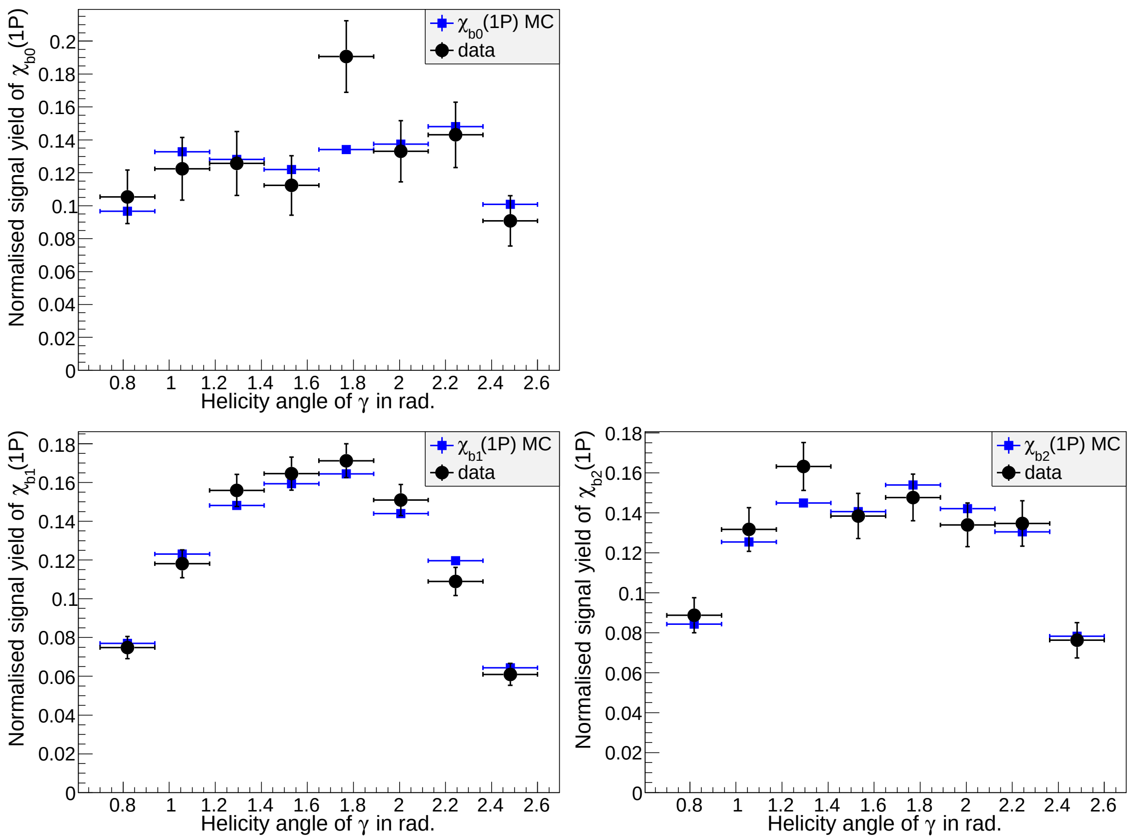

FIGURE B.1: Normalised signal yield in bins of the photon helicity angle. Black dots with error bars are the data and the blue squares with error bars are the signal MC expectations.

B.3 Kinematic Fit

In an event, measured energy and momentum (four-momentum) of final state particles are supposed to satisfy kinematic constraints to the initial four-momentum of the decaying particle [$\Upsilon(2S)$ in our case]. However, due to uncertainties associated with the four-momenta measurements, these kinematic constraints are not exactly matched. The measured values can be slightly varied within their uncertainties while applying the kinematic constraint. In an exclusive measurement, where all final state particles are measured, the kinematic fit can thus be used to improve the mass resolution. The fit is also known as '4C-fit' as it has four constraints corresponding to energy-momentum conservation.

Suppose the final state consists of n number of particles with four momentum $\mathbf{P_n}$ of the n^{th} particle is $[p_{nx}, p_{ny}, p_{nz}, \sqrt{p_n^2 + m_n^2}]$ and the initial four momentum $\mathbf{T}$ is $[t_x, t_y, t_z, t_E]$. The four constraints, f_x, f_y, f_z, f_E, on the energy and momentum can be expressed as,

$$\begin{aligned}
f_x &: \sum_n p_{nx} - t_x = 0, \\
f_y &: \sum_n p_{ny} - t_y = 0, \\
f_z &: \sum_n p_{nz} - t_z = 0, \\
f_E &: \sum_n (p_n^2 + m_n^2) - t_E = 0.
\end{aligned}$$

Then, least square fitting is performed with the application of the Lagrange multiplier method. The χ^2 is defined as,

$$\chi^2 = \sum_n (\mathbf{P_n} - \mathbf{P_n^0})^{\mathbf{T}} \mathbf{V_n^{-1}} (\mathbf{P_n} - \mathbf{P_n^0}),$$

where $\mathbf{P_n^0}$ and $\mathbf{P_n}$ are the measured and predicted value for four momentum of the n^{th} particle,respectively, that minimises the χ^2. A more detailed description of the fitting method is discussed in Ref. [84].

Apart from improving the mass resolution, the χ^2/NDF (NDF = 4) of the 4C fit can be useful in selecting the best candidate among the multiple candidates, if found in an event. It can also be utilized as a criterion for the signal selection.

In our search for the $X_{b\bar{b}}(9975)$ signal (Chapter 3), as expected we observed that χ^2 of the 4C-fit has a strong correlation with other kinematic variables like ΔE and $P^{\star}_{\Upsilon(2S)}$.

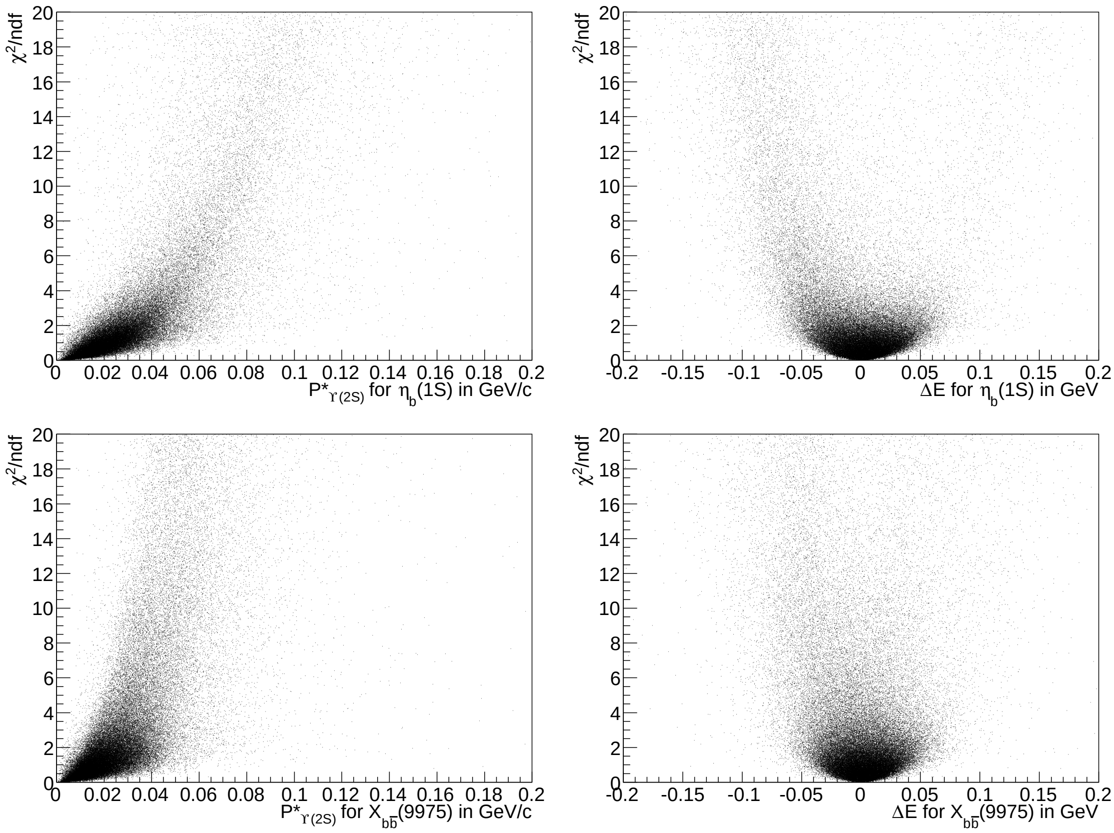

FIGURE B.2: The scatter plots in top are χ^2/NDF *vs.* $P^{\star}_{\Upsilon(2S)}$ (left) and *vs.* ΔE (right) from the signal MC sample of $\eta_b(1S) \to 3(\pi^+\pi^-)$, and the scatter plots in bottom are χ^2/NDF *vs.* $P^{\star}_{\Upsilon(2S)}$ (left) and *vs.* ΔE (right) from the signal MC sample of $X_{b\bar{b}}(9975) \to 3(\pi^+\pi^-)$.

We optimize the condition on χ^2/NDF in the same way as earlier done for other variables and compare the FOM obtained with that of previously optimized set of kinematic cuts. The FOM obtained from two approaches are found to be fairly close. In our latter analysis to study the hadronic decays of $\chi_{bJ}(1P)$ triplet, a criterion on χ^2/NDF is thus applied.

B.4 Results of Maximum Likelihood Fit

TABLE B.2: Results of the fit to the ΔM distribution from the sum of 26 reconstructed modes in the [0.03, 0.30] GeV/c^2 region for the $\Upsilon(2S)$ data sample (shown in Figure 3.29). The values with uncertainties are floated in the fit.

Component	Function	Parameter	Value
Background	Exponential	coefficient	-116.8 ± 9.2
	Chebyshev	slope	-0.25 ± 0.07
		fraction	0.406 ± 0.022
	Yield	(# Background)	1999 ± 56
$X_{b\bar{b}}(9975)$	Double Gaussian	mean	0.04901
	(Asym-Gauss	sigma1	0.00557
	+	sigma2	0.004898
	Gauss)	sigma	0.00183
		fraction	0.5275
	Yield	(# $X_{b\bar{b}}(9975)$)	-29.6 ± 18.7
$\chi_{b0}(1P)$	Double Gaussian	mean	0.16363 ± 0.00049
	(Asym-Gauss	sigma1	0.01083
	+	sigma2	0.007419
	Gauss)	sigma	0.003965
		fraction	0.3621
	Yield	(#$\chi_{b0}(1P)$)	299 ± 22
$\chi_{b1}(1P)$	Double Gaussian	mean	0.13043 ± 0.00023
	(Asym-Gauss	sigma1	0.01103
	+	sigma2	0.007624
	Gauss)	sigma	0.003678
		fraction	0.328
	Yield	(#$\chi_{b1}(1P)$)	946 ± 36
$\chi_{b2}(1P)$	Double Gaussian	mean	0.11127 ± 0.00034
	(Asym-Gauss	sigma1	0.01139
	+	sigma2	0.00794
	Gauss)	sigma	0.003521
		fraction	0.3117
	Yield	(#$\chi_{b2}(1P)$)	582 ± 31
		Fudge factor	1.232 ± 0.046

Table B.3: Results of the fit to the ΔM distribution from the sum of 26 reconstructed modes in the [0.45, 0.75] GeV/c^2 region for the $\Upsilon(2S)$ data sample (shown in Figure 3.31). The values with uncertainties are the variables which are floated in the fit.

Component	Function	Parameter	Value
Background	Chebyshev	slope	-0.0608 ± 0.073
	Yield	# Background	552 ± 25
$\eta_b(1S)$	Voigtian	mean	0.62043
		width	0.01
		sigma	0.007158
	Yield	$\#\eta_b(1S)$	-5.5 ± 9.6

Table B.4: Result of the fit to the ΔM distribution from the sum of 74 reconstructed modes in the [0.04, 0.24] GeV/c^2 region for the $\Upsilon(2S)$ data sample (shown in Figure 4.11). The values with uncertainties are the variables floated in the fit.

Component	Function	Parameter	Value
Background	Exponential	exponent	-99.4 ± 2.6
	Chebyshev	slope	-0.37 ± 0.03
		fraction	0.449 ± 0.011
		(# Background)	18101 ± 185
$\chi_{b0}(1P)$	Double Gaussian	mean	0.16428 ± 0.00033
	(Asym-Gauss	sigma1	0.01604
	+	sigma2	0.01107
	Gauss)	sigma	0.004562
		fraction	0.2826
	Yield	$(\#\chi_{b0}(1P))$	1197 ± 58
$\chi_{b1}(1P)$	Double Gaussian	mean	0.13021 ± 0.00012
	(Asym-Gauss	sigma1	0.017
	+	sigma2	0.011
	Gauss)	sigma	0.004195
		fraction	0.2588
	Yield	$(\#\chi_{b1}(1P))$	4747 ± 94
$\chi_{b2}(1P)$	Double Gaussian	mean	0.11145 ± 0.00016
	(Asym-Gauss	sigma1	0.01966
	+	sigma2	0.01245
	Gauss)	sigma	0.004069
		fraction	0.2371
	Yield	$(\#\chi_{b2}(1P))$	3064 ± 87
		Common-Fudge	1.134 ± 0.019

B.5 Significance of Modes for $\chi_{bJ}(1P)$ Study

Table B.5: Signal yield and significance of $\chi_{bJ}(1P)$, reconstructed from the 26 modes of charged hadrons. $\surd$ mark is for the modes that have at least 5σ significance in any of the $\chi_{bJ}(1P)(J = 0, 1, 2)$ signals and modes with $\times$ mark are those which do not follow the mentioned criteria.

Modes	χ_{b0}		χ_{b1}		χ_{b2}		
	N	σ	N	σ	N	σ	
$2\pi^+2\pi^-$	25.6 ± 9.7	3.0	72.5 ± 13.0	6.8	32.6 ± 11.8	3.1	$\surd$
$3\pi^+3\pi^-$	90.2 ± 11.4	11.0	286.3 ± 19.2	23.6	143.0 ± 15.7	12.6	$\surd$
$4\pi^+4\pi^-$	63.0 ± 10.2	8.5	266.7 ± 18.8	22.5	163.7 ± 16.6	14.6	$\surd$
$5\pi^+5\pi^-$	25.6 ± 6.8	4.9	84.8 ± 11.3	10.8	90.8 ± 12.2	10.9	$\surd$
$\pi^+\pi^-K^+K^-$	25.9 ± 5.4	8.1	33.9 ± 6.6	8.6	27.1 ± 6.5	6.3	$\surd$
$2\pi^+2\pi^-K^+K^-$	59.9 ± 9.6	8.7	157.6 ± 14.8	16.3	96.6 ± 12.9	11.5	$\surd$
$3\pi^+3\pi^-K^+K^-$	42.7 ± 9.2	5.8	132.5 ± 14.1	13.7	89.8 ± 13.1	9.8	$\surd$
$4\pi^+4\pi^-K^+K^-$	45.5 ± 8.1	7.9	71.1 ± 10.2	10.5	66.9 ± 10.5	9.6	$\surd$
$2K^+2K^-$	3.1 ± 1.0	3.3	3.1 ± 1.1	2.9	4.9 ± 1.3	3.0	$\times$
$\pi^+\pi^-2K^+2K^-$	16.6 ± 4.6	5.4	38.8 ± 7.1	8.6	33.7 ± 6.8	7.4	$\surd$
$2\pi^+2\pi^-2K^+2K^-$	14.5 ± 4.7	4.4	38.6 ± 7.5	7.8	34.7 ± 7.4	7.2	$\surd$
$3\pi^+3\pi^-2K^+2K^-$	10.2 ± 3.8	3.8	15.4 ± 5.0	4.5	23.8 ± 6.0	6.2	$\surd$
$\pi^+\pi^-p\overline{p}$	0.0 ± 5.8	1.5	2.4 ± 1.9	2.7	3.8 ± 2.1	3.6	$\times$
$2\pi^+2\pi^-p\overline{p}$	1.7 ± 2.1	0.9	45.0 ± 7.4	10.2	13.5 ± 4.8	3.5	$\surd$
$3\pi^+3\pi^-p\overline{p}$	10.2 ± 4.3	3.1	36.5 ± 7.2	7.8	15.3 ± 5.5	3.6	$\surd$
$4\pi^+4\pi^-p\overline{p}$	9.6 ± 3.7	3.8	6.4 ± 3.5	2.4	14.3 ± 4.9	4.4	$\times$
$\pi^+\pi^-K^+K^-p\overline{p}$	10.2 ± 3.5	4.2	17.6 ± 4.8	5.7	13.3 ± 4.7	3.7	$\surd$
$2\pi^+2\pi^-K^+K^-p\overline{p}$	16.4 ± 4.5	4.9	27.4 ± 6.2	6.3	11.4 ± 4.5	3.3	$\surd$
$3\pi^+3\pi^-K^+K^-p\overline{p}$	9.1 ± 3.6	3.7	4.5 ± 3.0	1.9	16.6 ± 5.0	4.7	$\times$
$\pi^\pm K^\mp K^0_S$	0.0 ± 0.5	0.0	4.0 ± 2.1	3.3	0.9 ± 1.2	1.1	$\times$
$\pi^+\pi^-\pi^\pm K^\mp K^0_S$	0.0 ± 3.2	0.0	74.9 ± 9.7	12.9	27.0 ± 7.2	5.0	$\surd$
$2\pi^+2\pi^-\pi^\pm K^\mp K^0_S$	10.6 ± 5.6	2.2	116.2 ± 12.8	13.9	64.3 ± 11.1	8.5	$\surd$
$3\pi^+3\pi^-\pi^\pm K^\mp K^0_S$	10.3 ± 5.6	2.1	55.9 ± 9.1	8.9	24.8 ± 7.2	4.3	$\surd$
$\pi^+\pi^-2K^0_S$	0.0 ± 0.5	0.0	1.0 ± 1.1	1.5	1.0 ± 1.0	1.3	$\times$
$2\pi^+2\pi^-2K^0_S$	8.1 ± 3.2	4.2	13.4 ± 4.1	5.4	13.6 ± 4.0	5.2	$\surd$
$3\pi^+3\pi^-2K^0_S$	5.1 ± 3.1	2.2	14.4 ± 4.5	5.0	11.4 ± 4.2	3.8	$\surd$

TABLE B.6: Signal yield and significance of $\chi_{bJ}(1P)$, reconstructed from the 22 modes of charged hadrons and a π^0. $\surd$ mark is for the modes that have at least 5σ significance in any of the $\chi_{bJ}(1P)(J=0,1,2)$ signals and modes with $\times$ mark are those which do not follow the mentioned criteria.

Modes	χ_{b0}		χ_{b1}		χ_{b2}		
	N	σ	N	σ	N	σ	
$\pi^+\pi^-K^+K^-\pi^0$	3.3 ± 5.1	0.7	88.0 ± 11.7	10.7	39.0 ± 9.5	5.2	$\surd$
$2\pi^+2\pi^-K^+K^-\pi^0$	45.7 ± 11.6	4.5	261.4 ± 20.0	18.3	170.4 ± 18.5	11.8	$\surd$
$3\pi^+3\pi^-K^+K^-\pi^0$	52.5 ± 11.9	5.2	198.6 ± 18.4	14.5	124.3 ± 17.1	9.0	$\surd$
$4\pi^+4\pi^-K^+K^-\pi^0$	9.3 ± 7.3	1.4	69.2 ± 11.7	7.8	40.0 ± 10.7	4.4	$\surd$
$2K^+2K^-\pi^0$	0.0 ± 0.5	0.0	5.7 ± 2.7	3.2	0.6 ± 1.3	0.5	$\times$
$\pi^+\pi^-2K^+2K^-\pi^0$	12.2 ± 4.8	3.2	46.2 ± 8.4	7.9	22.0 ± 7.2	3.9	$\surd$
$2\pi^+2\pi^-2K^+2K^-\pi^0$	15.7 ± 6.0	3.2	30.0 ± 7.7	5.0	18.7 ± 6.6	3.5	$\surd$
$3\pi^+3\pi^-2K^+2K^-\pi^0$	7.7 ± 4.4	2.1	15.4 ± 5.6	3.6	19.0 ± 6.0	4.2	$\times$
$\pi^+\pi^-p\overline{p}\pi^0$	0.0 ± 3.5	0.0	17.4 ± 4.9	5.4	9.9 ± 4.2	3.3	$\surd$
$2\pi^+2\pi^-p\overline{p}\pi^0$	2.8 ± 4.6	0.6	28.0 ± 7.4	4.9	22.9 ± 7.6	3.6	$\times$
$3\pi^+3\pi^-p\overline{p}\pi^0$	3.7 ± 4.3	0.9	20.8 ± 6.7	3.8	12.6 ± 6.3	2.3	$\times$
$4\pi^+4\pi^-p\overline{p}\pi^0$	0.5 ± 5.6	0.1	13.3 ± 5.2	3.5	7.4 ± 4.5	2.0	$\times$
$\pi^+\pi^-K^+K^-p\overline{p}\pi^0$	6.8 ± 3.7	2.8	20.9 ± 6.2	5.5	14.3 ± 5.7	3.3	$\surd$
$2\pi^+2\pi^-K^+K^-p\overline{p}\pi^0$	1.8 ± 2.6	0.8	15.8 ± 5.2	4.2	20.0 ± 5.6	4.8	$\times$
$3\pi^+3\pi^-K^+K^-p\overline{p}\pi^0$	2.7 ± 3.1	1.0	3.3 ± 3.2	1.2	10.0 ± 4.6	2.7	$\times$
$\pi^\pm K^\mp K^0_S\pi^0$	6.5 ± 3.0	3.0	8.6 ± 3.7	3.2	5.4 ± 3.3	2.1	$\times$
$\pi^+\pi^-\pi^\pm K^\mp K^0_S\pi^0$	8.2 ± 5.8	1.5	110.8 ± 13.2	11.9	55.8 ± 11.4	6.1	$\surd$
$2\pi^+2\pi^-\pi^\pm K^\mp K^0_S\pi^0$	30.9 ± 9.6	3.8	137.0 ± 15.4	12.1	67.1 ± 13.3	6.1	$\surd$
$3\pi^+3\pi^-\pi^\pm K^\mp K^0_S\pi^0$	29.6 ± 8.7	4.1	64.7 ± 11.0	7.6	39.2 ± 10.1	4.7	$\surd$
$\pi^+\pi^-2K^0_S\pi^0$	1.2 ± 1.7	1.7	4.5 ± 3.0	2.0	1.5 ± 3.1	0.7	$\times$
$2\pi^+2\pi^-2K^0_S\pi^0$	7.8 ± 4.2	2.3	17.8 ± 5.6	4.3	8.8 ± 5.0	2.1	$\times$
$3\pi^+3\pi^-2K^0_S\pi^0$	4.1 ± 3.6	1.3	9.5 ± 4.8	2.4	13.4 ± 5.5	3.0	$\times$

TABLE B.7: Signal yield and significance of $\chi_{bJ}(1P)$, reconstructed from the 26 modes of charged hadrons and two π^0's. $\surd$ mark for the modes that have at least 5σ significance in any of the $\chi_{bJ}(1P)(J = 0, 1, 2)$ signals and modes with $\times$ mark are those which do not follow the mentioned criteria.

Modes	χ_{b0}		χ_{b1}		χ_{b2}		
	N	σ	N	σ	N	σ	
$2\pi^+2\pi^-2\pi^0$	42.0 ± 12.2	3.9	282.5 ± 22.2	16.9	213.5 ± 21.3	12.5	$\surd$
$3\pi^+3\pi^-2\pi^0$	101.1 ± 17.3	6.7	556.3 ± 30.9	24.0	308.5 ± 27.2	13.6	$\surd$
$4\pi^+4\pi^-2\pi^0$	66.9 ± 14.6	5.3	365.7 ± 25.1	19.6	251.7 ± 23.5	13.3	$\surd$
$5\pi^+5\pi^-2\pi^0$	19.5 ± 8.5	2.6	87.8 ± 13.3	8.4	82.7 ± 14.2	7.1	$\surd$
$\pi^+\pi^-K^+K^-2\pi^0$	24.4 ± 8.6	3.3	57.8 ± 10.5	7.0	47.6 ± 10.6	5.4	$\surd$
$2\pi^+2\pi^-K^+K^-2\pi^0$	39.4 ± 11.5	3.9	129.5 ± 16.3	10.0	89.5 ± 15.7	6.8	$\surd$
$3\pi^+3\pi^-K^+K^-2\pi^0$	35.6 ± 11.1	3.6	114.3 ± 15.3	9.4	77.5 ± 14.6	6.3	$\surd$
$4\pi^+4\pi^-K^+K^-2\pi^0$	9.6 ± 6.6	1.6	35.8 ± 8.9	4.9	20.7 ± 8.6	2.7	$\times$
$2K^+2K^-2\pi^0$	0.1 ± 2.6	0.1	3.2 ± 2.3	2.4	1.2 ± 1.8	0.8	$\times$
$\pi^+\pi^-2K^+2K^-2\pi^0$	0.8 ± 3.0	0.3	19.2 ± 5.6	4.6	8.1 ± 4.4	2.1	$\times$
$2\pi^+2\pi^-2K^+2K^-2\pi^0$	10.1 ± 4.9	2.5	9.1 ± 4.6	2.4	20.6 ± 6.6	3.9	$\times$
$3\pi^+3\pi^-2K^+2K^-2\pi^0$	3.5 ± 3.1	1.3	6.0 ± 4.1	1.7	9.0 ± 4.4	4.1	$\times$
$\pi^+\pi^-p\overline{p}2\pi^0$	0.0 ± 1.4	0.0	10.2 ± 4.4	3.1	15.6 ± 4.9	4.2	$\times$
$2\pi^+2\pi^-p\overline{p}2\pi^0$	13.3 ± 5.9	2.7	27.6 ± 7.1	5.0	25.3 ± 7.1	4.4	$\surd$
$3\pi^+3\pi^-p\overline{p}2\pi^0$	0.0 ± 1.0	0.0	9.1 ± 5.4	1.9	9.1 ± 5.6	1.9	$\times$
$4\pi^+4\pi^-p\overline{p}2\pi^0$	4.4 ± 3.5	1.5	5.6 ± 3.5	1.9	6.5 ± 3.8	2.0	$\times$
$\pi^+\pi^-K^+K^-p\overline{p}2\pi^0$	2.6 ± 2.1	1.6	7.1 ± 3.2	3.2	5.4 ± 3.2	2.3	$\times$
$2\pi^+2\pi^-K^+K^-p\overline{p}2\pi^0$	5.4 ± 3.3	2.0	5.2 ± 3.0	2.0	4.9 ± 3.0	2.0	$\times$
$3\pi^+3\pi^-K^+K^-p\overline{p}2\pi^0$	3.6 ± 2.3	2.0	0.0 ± 0.5	0.0	2.9 ± 2.0	2.0	$\times$
$\pi^\pm K^\mp K^0_S 2\pi^0$	0.0 ± 24.8	0.0	14.8 ± 4.7	4.5	3.0 ± 3.1	1.1	$\times$
$\pi^+\pi^-\pi^\pm K^\mp K^0_S 2\pi^0$	37.3 ± 9.1	5.1	78.2 ± 11.8	8.6	35.7 ± 9.7	4.2	$\surd$
$2\pi^+2\pi^-\pi^\pm K^\mp K^0_S 2\pi^0$	27.0 ± 8.9	3.5	90.8 ± 13.1	9.1	53.1 ± 12.3	5.1	$\surd$
$3\pi^+3\pi^-\pi^\pm K^\mp K^0_S 2\pi^0$	12.4 ± 7.2	1.9	35.1 ± 9.7	4.2	18.1 ± 9.0	2.2	$\times$
$\pi^+\pi^-2K^0_S 2\pi^0$	6.1 ± 2.8	3.1	4.6 ± 2.5	2.5	4.3 ± 2.7	2.2	$\times$
$2\pi^+2\pi^-2K^0_S 2\pi^0$	1.1 ± 2.3	0.5	9.1 ± 3.8	3.2	6.4 ± 4.0	2.0	$\times$
$3\pi^+3\pi^-2K^0_S 2\pi^0$	6.6 ± 4.0	2.0	13.3 ± 5.0	3.3	14.7 ± 5.3	3.6	$\times$

B.6 $\chi_{b0}(1P)$ Width Measurement

As mentioned in Chapter 1, the width of $\chi_{b0}(1P)$ can be as large as 2 MeV, but till now no experimental measurement has been done for it. Large signal yield obtained in our branching fraction studies of the $\chi_{bJ}(1P)$ triplet (Chapter 4) motivated us to measure the width of $\chi_{b0}(1P)$. Cross-checks done so far towards this purpose are described in following sub-sections.

B.6.1 Linearity Test

- Several signal MC samples are generated for different assumed $\chi_{b0}(1P)$ widths.
- A linearity test is performed between the generated signal width *vs.* that obtained from the fit. For this, first a sample is prepared in which background is taken from the generic MC sample from the sum of 41 significant modes found in Chapter 4. The $\chi_{bJ}(1P)$ signals generated with zero width are added to this sample with a yield equal to that obtained in sum of the 41 modes. A maximum likelihood fit is performed in this sample, the background is fitted with a sum of an exponential function and a first-order Chebyshev polynomial, whereas signals are fitted with a sum of a Gaussian and an asymmetric Gaussian function, same as described in Chapter 4. The fit to the zero width case is shown in Figure B.3.
- Next, the $\chi_{b0}(1P)$ signal generated for the different width cases are introduced in the sample with the same yield and then the maximum likelihood fit is performed on the ΔM distribution. The fit function is similar to the previous case, except for the $\chi_{b0}(1P)$ signal, where the sum of Gaussian functions is convolved with a Breit-Wigner function. The asymmetric Gaussian is convolved numerically using FFTW (Fastest Fourier Transform in the West) [85] package of ROOT while the symmteric Gaussian is convolved analytically (Voigtian function of RooFit) with the same Breit-Wigner function. Here, all the parameters are kept fixed to the nominal values obtained by fitting to the zero width case, except the width of the Breit-Wigner function for the $\chi_{b0}(1P)$ case, and all the signal and background yields are varied. The fitting is performed on one sample for each width case and a comparison of

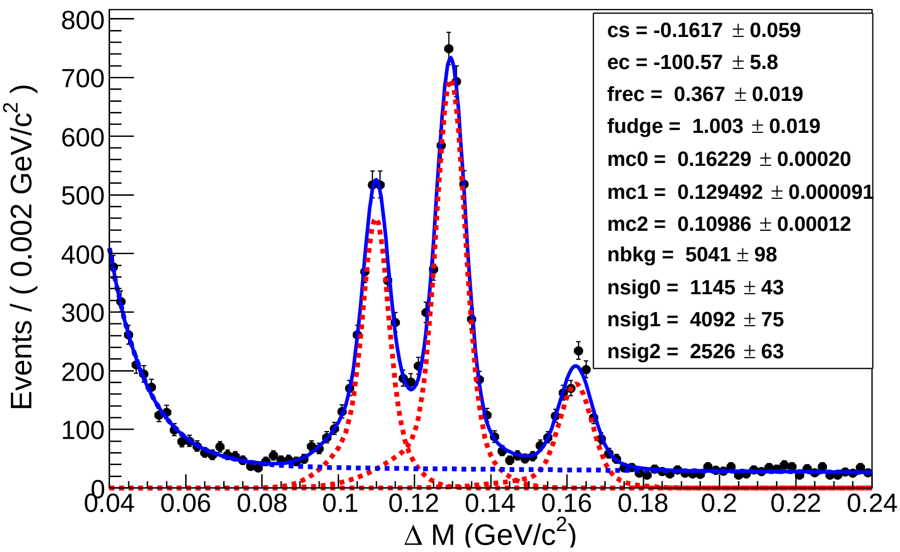

FIGURE B.3: Fit to the ΔM distribution from the sum of 41 significant modes in a mixed sample of generic and signal MC events. Here, all the signals are generated with zero width.

the generated *vs.* fitted width from the fit is shown in Figure B.4. The plot has a linear behaviour even for width cases below 2 MeV.

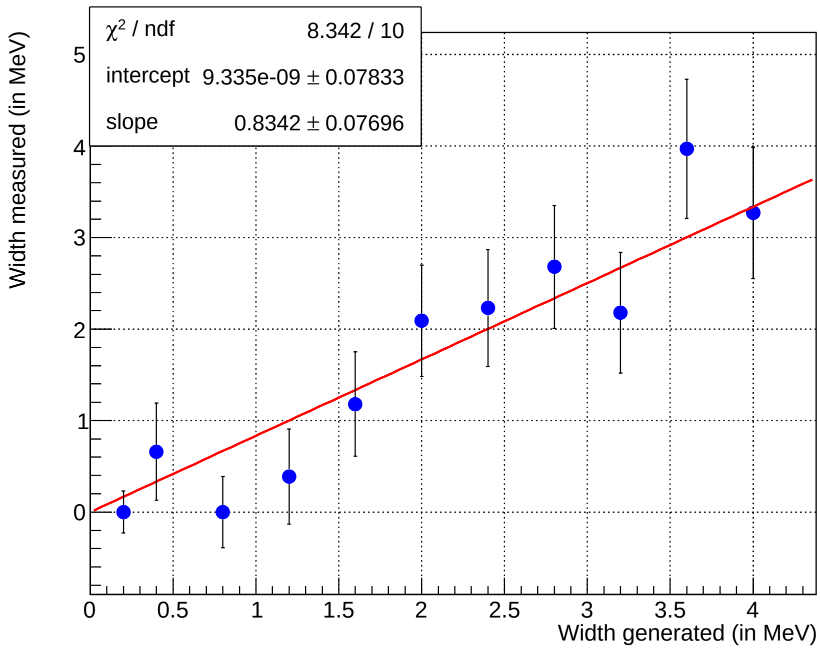

FIGURE B.4: Comparison of the generated *vs.* fitted width from the fit.

B.6.2 Photon Energy Calibration

- The Calibration is done using π^0 reconstructed from two γ's. The method is similar to that mentioned in Ref. [32] and also described in the (internal) Belle Note [86].

- Energy asymmetry between the γ's of the π^0 is required to be small, thus a criterion $|E_1 - E_2|/(E_1 + E_2) < 0.05$ is applied, where E_1 and E_2 are the energies of the γ's. Also, photons only in the barrel region is used, because our $\chi_{bJ}(1P)$ signal photon is reconstructed only from that part of the ECL.

- Diphoton invariant mass ($\sim$ M[π^0]) is divided in 10 bins of E_γ, (with a bin size of 25 MeV) in the range (100, 350) MeV. Note that the $\chi_{b0}(1P)$ signal photon has an energy range 100 – 240 MeV.

- A $24.7\,\mathrm{fb}^{-1}$ of on-resonance $\Upsilon(2S)$ data and an equivalent amount of generic MC sample are used. Each bin is fitted invidually with equal number of events (0.3M events).

- First, the diphoton invariant mass distribution for the MC sample in each bin is fitted with a Crystal Ball (CB) function plus a first order Chebyshev polynomial. Then it is fitted for data in each bin with the same function used for the MC sample, where the signal (CB function) parameters are fixed from MC events with the introduction of two new variables: mean shift (ΔM) and a fudge factor (f) by substituting, $M \to M + \Delta M$ and $\sigma \to \sigma f$.

- For the $\pi^0 \to \gamma\gamma$ decay mode:

$$M^2 = 2E_1E_2(1 - \cos\theta)$$
$$2M\delta M = 2(E_2\delta E_1 + E_1\delta E_2)(1 - \cos\theta)$$
$$\frac{2\delta M}{M} = \frac{\delta E_1}{E_1} + \frac{\delta E_2}{E_2}$$
$$\frac{\delta E}{E} = \frac{\delta M}{M}$$
$$\frac{\delta E}{E} = \frac{\delta M}{M[\pi^0]}$$

where δM is the deviation from mean obtained in data and $M[\pi^0]$ is nominal π^0 mass [13]. The plot for $\delta E/E$ (resolution) in data with energy is shown in Figure B.5. Resolution for the $\chi_{b0}(1P)$ signal photon energy is found to be approximately 1.6 MeV.

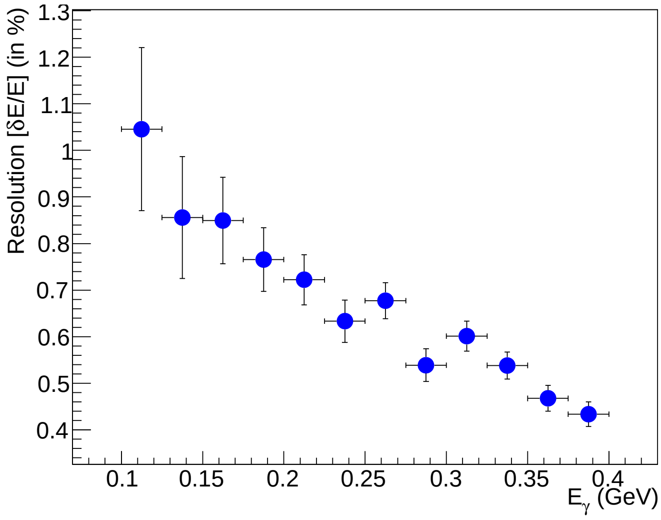

Figure B.5: Variation of the energy resolution of photon with its energy.

- Variation of the fudge-factor (to account for the data-MC difference) with energy is also measured and shown in Figure B.6. Acceptable data-MC diference observed, and the disagreement is more for the lower energy.

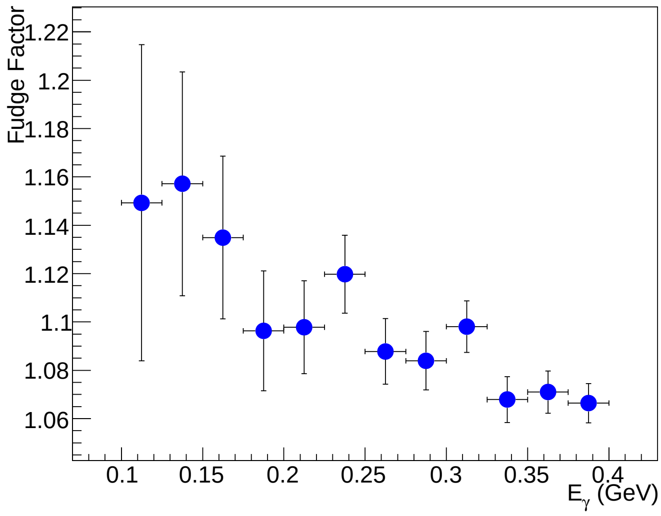

Figure B.6: Variation of the fudge factor with the photon energy.

If the $\chi_{b0}(1P)$ width is larger than 1.5 MeV then above cross-checks make us confident that it can be measured in our analysis.

Bibliography

[1] W. Kwong, J. Rosner, and C. Quigg, Ann. Rev. Nucl. Part. Sci. **37**, 325 (1987).

[2] D. H. Perkins, *Introduction to High Energy Physics*, vol. 4 (Cambridge University Press, 2000).

[3] E. Eichten, K. Gottfried, T. Kinoshita, K. D. Lane, and T. M. Yan, Phys. Rev. D **17**, 3090 (1978).

[4] E. Eichten, K. Gottfried, T. Kinoshita, K. D. Lane, and T. M. Yan, Phys. Rev. D **21**, 313 (1980).

[5] M. Voloshin, Prog. in Part. and Nucl. Phys. **61**, 455 (2008), ISSN 0146-6410.

[6] K. Berkelman, Rep. Prog. Phys. **49**, 1 (1986).

[7] S. W. Herb et al., Phys. Rev. Lett. **39**, 252 (1977).

[8] The plot is taken from the URL: http://www.lns.cornell.edu/public/lab-info/upsilon.html †.

[9] K. Han et al., Phys. Rev. Lett. **49**, 1612 (1982).

[10] G. Eigen et al., Phys. Rev. Lett. **49**, 1616 (1982).

[11] C. Klopfenstein et al., Phys. Rev. Lett. **51**, 160 (1983).

[12] F. Pauss et al., Phys. Lett. B **130**, 439 (1983).

[13] K. Olive et al. (Particle Data Group), Chin. Phys. **C38**, 092001 (2014).

[14] G. Aad et al. (ATLAS Collaboration), Phys. Rev. Lett. **108**, 152001 (2012).

[15] V. M. Abazov et al. (DØ Collaboration), Phys. Rev. D **86**, 031103 (2012).

[16] R. Aaij et al. (LHCb Collaboration), JHEP **2014**, 88 (2014).

[17] R. Barbieri, R. Gatto, and R. Kgerler, Phys. Lett. B **60**, 183 (1976).

[18] C.-W. Hwang and R.-S. Guo, Phys. Rev. D **82**, 034021 (2010).

[19] G.-L. Wang, Phys. Lett. B **653**, 206 (2007).

[20] G.-L. Wang, Phys. Lett. B **674**, 172 (2009).

[21] J. T. Laverty, S. F. Radford, and W. W. Repko, arXiv:0901.3917 [hep-ph] (2009).

[22] D. Ebert, R. N. Faustov, and V. O. Galkin, Phys. Rev. D **67**, 014027 (2003).

[23] S. N. Gupta, J. M. Johnson, and W. W. Repko, Phys. Rev. D **54**, 2075 (1996).

[24] S. Godfrey and N. Isgur, Phys. Rev. D **32**, 189 (1985).

[25] D. M. Asner et al. (CLEO Collaboration), Phys. Rev. D **78**, 091103 (2008).

[26] T. Barnes, S. Godfrey, and E. S. Swanson, Phys. Rev. D **72**, 054026 (2005).

[27] C. Patrignani, T. Pedler, and J. Rosner, Ann. Rev. Nucl. Part. Sci. **63**, 21 (2013).

[28] I. Adachi et al. (Belle Collaboration), Phys. Rev. Lett. **108**, 032001 (2012).

[29] B. Aubert et al. (BaBar Collaboration), Phys. Rev. Lett. **101**, 071801 (2008).

[30] B. Aubert et al. (BaBar Collaboration), Phys. Rev. Lett. **103**, 161801 (2009).

[31] G. Bonvicini et al. (CLEO Collaboration), Phys. Rev. D **81**, 031104 (2010).

[32] R. Mizuk et al. (Belle Collaboration), Phys. Rev. Lett. **109**, 232002 (2012).

[33] S. Meinel, Phys. Rev. D **82**, 114502 (2010).

[34] B. A. Kniehl, A. A. Penin, A. Pineda, V. A. Smirnov, and M. Steinhauser, Phys. Rev. Lett. **92**, 242001 (2004).

[35] S. Dobbs, Z. Metreveli, A. Tomaradze, T. Xiao, and K. K. Seth, Phys. Rev. Lett. **109**, 082001 (2012).

[36] T. J. Burns, Phys. Rev. D **87**, 034022 (2013).

[37] R. J. Dowdall, C. T. H. Davies, T. Hammant, and R. R. Horgan (HPQCD Collaboration), Phys. Rev. D **89**, 031502 (2014).

[38] A. Abashian et al. (Belle Collaboration), Nucl. Instrum. Methods Phys. Res, Sect. A **479**, 117 (2002).

[39] J. Brodzicka, T. Browder, P. Chang, S. Eidelman, B. Golob, K. Hayasaka, H. Hayashii, T. Iijima, K. Inami, K. Kinoshita, et al. (for the Belle Collaboration), Prog. of Theor. and Exp. Phys. **2012**, 04D001 (2012).

[40] S. Kurokawa and E. Kikutani, Nucl. Instrum. Methods Phys. Res, Sect. A **499**, 1 (2003), and other papers included in this volume.

[41] T. Abe et al., Prog. Theor. Exp. Phys. **03A001**, 1 (2013), and following articles up to **03A011**.

[42] B. Aubert et al., Nucl. Instrum. Methods Phys. Res, Sect. A **479**, 1 (2002).

[43] M. Kobayashi and T. Maskawa, Prog. Theor. Phys. **49**, 652 (1973).

[44] "The Nobel Prize in Physics 2008 - Advanced Information".

[45] http://belle.kek.jp/belle/transparency/accelerator1.html.

[46] H. Aihara et al., Nucl. Instrum. Methods Phys. Res, Sect. A **568**, 269 (2006).

[47] Z. Natkaniec et al., Nucl. Instrum. Methods Phys. Res, Sect. A **560**, 1 (2006).

[48] H. Hirano et al., Nucl. Instrum. Methods Phys. Res, Sect. A **455**, 294 (2000).

[49] M. Akatsu et al., Nucl. Instrum. Methods Phys. Res, Sect. A **452**, 322 (2000).

[50] T. Iijima et al., Nucl. Instrum. Methods Phys. Res, Sect. A **453**, 321 (2000).

[51] H. Kichimi et al., Nucl. Instrum. Methods Phys. Res, Sect. A **453**, 315 (2000).

[52] J. Nam et al., Nucl. Instrum. Methods Phys. Res, Sect. A **491**, 54 (2002).

[53] K. Miyabayashi, Nucl. Instrum. Methods Phys. Res, Sect. A **494**, 298 (2002).

[54] H. Ikeda et al., Nucl. Instrum. Methods Phys. Res, Sect. A **441**, 401 (2000).

[55] Y. Ushiroda et al., Nucl. Instrum. Methods Phys. Res, Sect. A **438**, 460 (1999).

[56] S. Y. Suzuki et al., Nucl. Instrum. Methods Phys. Res, Sect. A **453**, 440 (2000).

[57] S. Y. Suzuki et al., Nucl. Instrum. Methods Phys. Res, Sect. A **494**, 535 (2002).

[58] E. Nakano, Nucl. Instrum. Methods Phys. Res, Sect. A **494**, 402 (2002).

[59] H. Hamasaki et al. (PID group), Belle Note # 321.

[60] K. Hanagaki et al. (PID group), Belle Note # 312.

[61] X. L. Wang et al., Phys. Rev. D **84**, 071107 (2011).

[62] S. Nagayama, Belle Note # 130, 131 and 132.

[63] D. J. Lange, Nucl. Instrum. Methods Phys. Res, Sect. A **462**, 152 (2001).

[64] T. Sjöstrand, Comput. Phys. Commun. **27**, 243 (1982), **28** (1983) 229, **39** (1986) 347.

[65] T. Sjöstrand, S. Mrenna, and P. Skands, Comput. Phys. Commun. **178**, 852 (2008).

[66] R. Brun, F. Bruyant, M. Maire, A. McPherson, and P. Zanarini, CERN DD/EE/84-1 (1987), GEANT3 user's guide.

[67] R. Jeffrey, *An experimenter's guide to the helicity formalism*, CALT-68-1148 (1984).

[68] M. Jacob and G. Wick, Annals Phys. **281**, 774 (2000).

[69] E. Barberio and Z. Wąs, Comput. Phys. Commun. **79**, 291 (1994).

[70] P. Golonka and Z. Wąs, Eur. Phys. J. C **45**, 97 (2006).

[71] P. Golonka and Z. Wąs, Eur. Phys. J. C **50**, 53 (2007).

[72] S. Nishida, Belle Note # 779.

[73] G. Majumder, Belle Note # 670.

[74] K. Tien, Belle Note # 1279.

[75] F. Fang, Belle Note # 323.

[76] K.-F. Chen et al. (Belle Collaboration), Phys. Rev. D **72**, 012004 (2005).

[77] K. Miyabayashi (Belle calorimeter group), Belle Note # 679.

[78] S. Sandilya et al. (Belle Collaboration), Phys. Rev. Lett. **111**, 112001 (2013).

[79] http://belle2.kek.jp/detector.html.

[80] J. Schieck, Nucl. Instrum. Methods Phys. Res, Sect. A **732**, 160 (2013).

[81] M. Friedl et al., Nucl. Instrum. Methods Phys. Res, Sect. A **732**, 83 (2013).

[82] C. Irmler et al., Nucl. Instrum. Methods Phys. Res, Sect. A **732**, 109 (2013).

[83] https://belle2.cc.kek.jp/ twiki/bin/view/Detector/SVD/GluingPage.

[84] R.-J. Li, Belle Note # 1238.

[85] http://www.fftw.org.

[86] A. Bondar and R. Mizuk, Belle Note # 1218.